AN ABSTRACT OF THE DISSERTATION OF

Ahmet Alper Dumanli for the degree of Doctor of Philosophy in Robotics presented on March 18, 2021.

Title: Active and Passive Control of Machine Tool Vibrations for High Speed and Accuracy.

Abstract approved:

_____

Burak Sencer

High-performance mechatronic systems are widely used in precision manufacturing equipment such as CNC machine tools, 3D-Printers, photolithography systems, industrial robots, and Coordinate Measuring Machines (CMMs). These equipment are utilized in producing parts and components for aviation, semiconductor, optics, and many other emerging industries, with geometric features and surface properties within micrometer-, or even in some cases nanometer-level accuracy. To keep up with the rapidly increasing productivity and accuracy demands, it is crucial that mechatronic systems of these manufacturing equipment deliver high-speed motion with high precision. In this dissertation, motion control strategies are presented to increase dynamic positioning accuracy and productivity of such mechatronic systems. First, a novel trajectory generation method is presented to avoid exciting low frequency structural vibration modes of machine tools and 3D-Printers, without compromising from productivity. The trajectory generation problem is posed as a convex optimization problem, and a practical windowing method is presented to implement the proposed strategy in real-time for long and realistic manufacturing scenarios. The proposed algorithm is validated on an industrial 3-Axis machine tool, and 4-6 times attenuation of the column vibration mode is achieved with 1[g] acceleration commands, without increasing the cycle time compared to state-of-the-art trajectory generation methods.

This is followed by proposition of a data-driven trajectory shaping algorithm designed to eliminate dynamic positioning errors induced by flexible motion transmission components (such as ball-screw drives) and nonlinear friction forces typically caused by mechanical bearings and guiding units. The proposed algorithm is used for optimizing trajectory pre-filters through machine-in-the-loop iterations, in a data-driven fashion, and therefore it can be applied on a wide variety of systems without requiring elaborate dynamic modeling. Effectiveness of the proposed technique is validated on a linear-motor-driven planar motion stage and an industrial 3-Axis machine tool, and it is shown that dynamic errors are reduced by 3-5 times compared to industry-standard approaches. Finally, an active tool position control strategy is proposed to mitigate self-excited (chatter) vibrations for improving stability margins of turning processes. Two motion control algorithms are developed to control the dynamic *process* defined by the interaction of the tool and the workpiece. An industrial lathe (turning center) is utilized for validating the effectiveness of proposed algorithms. A piezo-actuator driven tool-assembly is utilized to control tool position during the machining process, utilizing tool acceleration feedback, and the experiments show that 4-5 times increase in productivity (widths of cut) is achieved by the proposed strategy.

Active and Passive Control of Machine Tool Vibrations for High Speed and Accuracy

by
Ahmet Alper Dumanli

A DISSERTATION

submitted to

Oregon State University

in partial fulfillment of
the requirements for the
degree of

Doctor of Philosophy

Presented March 18, 2021
Commencement June 2021

Doctor of Philosophy dissertation of Ahmet Alper Dumanli presented on March 18, 2021.

APPROVED:

Major Professor, representing Robotics

Associate Dean for Graduate Programs, College of Engineering

Dean of the Graduate School

I understand that my dissertation will become part of the permanent collection of Oregon State University libraries. My signature below authorizes release of my dissertation to any reader upon request.

Ahmet Alper Dumanli, Author

ACKNOWLEDGEMENTS

I would like to express my sincere appreciation and gratitude to my advisor, Prof. Burak Sencer. His expertise in mechatronics and manufacturing technology, and enthusiasm in creating high quality work has been a great source of inspiration, and it has been very rewarding working with him.

I also would like to thank my friends and colleagues who works or have worked at Manufacturing Process Control Laboratory (MPCL); Shingo Tajima, Bora Eren, Christopher Indrarto, Joseph Tinnell, Tucker Shannon, Josiah Adam Breen, Yili Zhang, Jordan Meader and Angel Huang for their support and assistance in preparing this dissertation.

Finally, I would like to thank all my friends all over the world for their endless friendship and support.

TABLE OF CONTENTS

TABLE OF CONTENTS (Continued)

TABLE OF CONTENTS (Continued)

LIST OF FIGURES

LIST OF FIGURES (Continued)

Figure Page

DEDICATION

I would like to dedicate this dissertation to my parents Tahir and Ülkü Dumanlı, and my sister Seçil Dumanlı, and I am forever grateful for their life-long love and support.

1. General Introduction

Accuracy and productivity of precision motion generation systems such as CNC machine tools [1] (see Figure 1.a), 3D printers [2] (see Figure 1.b), industrial robots [3], photo-lithography equipment [4] and coordinate measuring machines (CMMs) are determined by dynamic positioning accuracy of their motion delivery mechanisms (commonly referred to as fed drives). The main goal of precision feed drives is to deliver high-speed motion with excellent dynamic positioning accuracy. To achieve this goal, high bandwidth control of precision motion delivery systems with the capability of rejection external disturbance forces has been an active research interest of mechatronics community, e.g. [5], [6], [7], [8] and [9].

Figure 1. Examples of a CNC machine tool (a) and a 3D-Printer (b).

Achievable accuracy of precision motion delivery systems and precision manufacturing equipment is limited by several factors. First, manufacturing equipment typically exhibit structural vibration modes originating from lightly damped mechanical components such as columns that carry the cutting tool of a CNC machine [10], or the extrusion nozzle of a 3D-Printer [11]. These equipment are typically operated at high speeds, following motion trajectories with rapidly varying acceleration/deceleration commands. Inertial forces generated by these commands

inevitably excite lightly damped structural vibration modes, which have detrimental effects on the quality of manufactured components. For example, vibrations of the cutting tool of a CNC milling machine with respect to the motion stage cause distortion of the manufactured workpiece's geometry and surface [10] as demonstrated by Figure.

Second, vibrations may also occur within the feed drives since most feed drives consist of mechanical transmission components with limited stiffness. For example, ball-screw driven motion stages are commonly used in modern machine tools [12]. A ball-screw driven stage delivers translational/linear motion by converting the rotary motion generated by its motor through a ball-screw shaft/nut interface. Limited stiffness of their ball-screw shaft and support bearings causes ball-screw drives to exhibit lightly damped torsional and axial vibration modes [13]. This causes the work-table to vibrate, causing large dynamic errors during positioning [5].

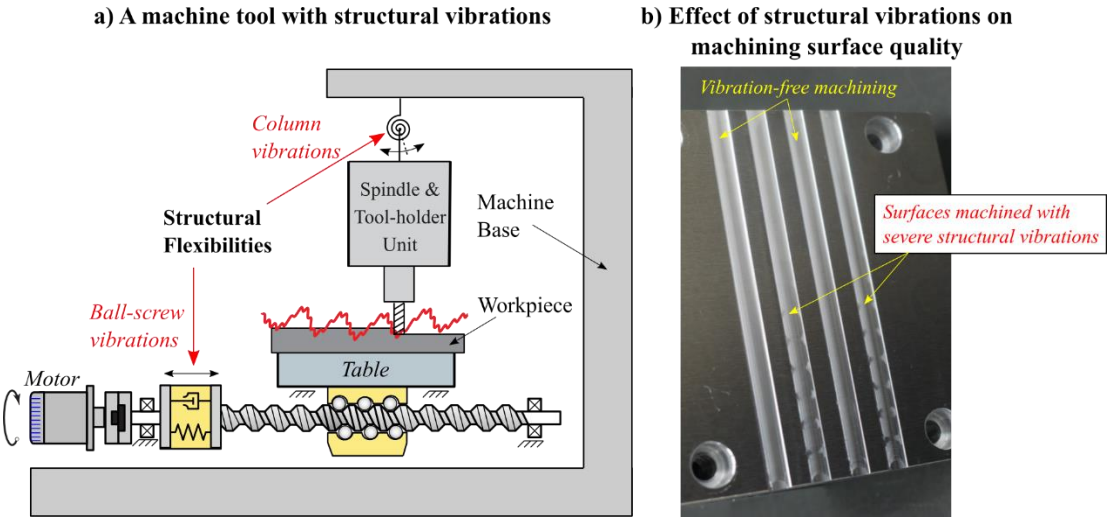

Figure 2. Illustration of a machine tool exhibiting ball-screw and column vibrations (a), and the effect of structural vibrations on machining surface quality (b) [10].

In addition to structural vibrations, dynamics of the servo controller also induce command tracking errors, limiting the positioning accuracy of feed drives. As the motion axes try to follow a rapidly accelerating trajectory, servo controller overcomes inertial and viscous friction forces, which cause the axes lag the original trajectory [14], and therefore cause dynamic positioning errors. This lagging effect is further exacerbated by power amplifiers of actuators [1], non-minimum phase zeros introduced

by higher order mechanical dynamics [15] and time-discretization, all of which introduce additional phase loss within the control loop.

Another significant source of dynamic positioning errors (and thus manufacturing inaccuracy) is disturbance forces. Disturbances can either be inherent to the mechanical design of feed drives (such as friction) [7], or they could be external, injected to the system by the manufacturing process, such as cutting forces in machining applications [16]. Friction forces can either be induced by lubricants in mechanical bearing and guiding units as viscous friction [12]. Or, they can be induced by microscale mechanical breakage dynamics between rubbing surfaces of bearings and guiding components, which is typically known as pre-motion (pre-sliding or pre-rolling) friction [17]. Viscous friction linearly depends on the velocity, and it typically varies slowly [18]. Thus, conventional feedback controllers can easily eliminate errors induced by viscous friction forces. Pre-motion friction, on the other hand, varies rapidly anytime the feed drive comes to a full stop and changes its direction of motion (i.e. velocity reversals), following a Hysteresis behavior as demonstrated in Figure 3.a. These forces are difficult to compensate, and they induce large tracking errors [14]. These command tracking errors are imprinted on surfaces that are being produced in machining applications, and therefore they limit the achievable accuracy of machined parts as shown in Figure 3.b.

In addition to internal disturbances, external disturbances such as process (cutting) forces decrease positioning accuracy of precision motion systems and hinders manufacturing quality. A cutting process can either be stable or unstable [19]. Stable cutting occurs when disturbance forces are bounded (do not increase over time) during the cutting process. These forces can either be constant (e.g. turning), or periodic (milling), and they are easily suppressed by dynamically stiff feedback controllers. Elastic deformations of the machine's structure, feed drive, workpiece and the cutting tool may result in a wavy surface on the workpiece during the cutting process. This waviness results in cutting forces to fluctuate. For instance, in turning processes, fluctuations in cutting forces may get exacerbated at each rotation of the spindle, depending on the spindle speed. As a result, cutting forces increase at every cycle of the spindle rotation, causing an unstable cut [16]. These fluctuations in cutting forces

cause unstable vibrations, which are known as regenerative self-excited chatter vibrations, and they are the most detrimental type of process disturbances. They decrease the surface quality of the workpiece greatly and may damage the manufacturing equipment.

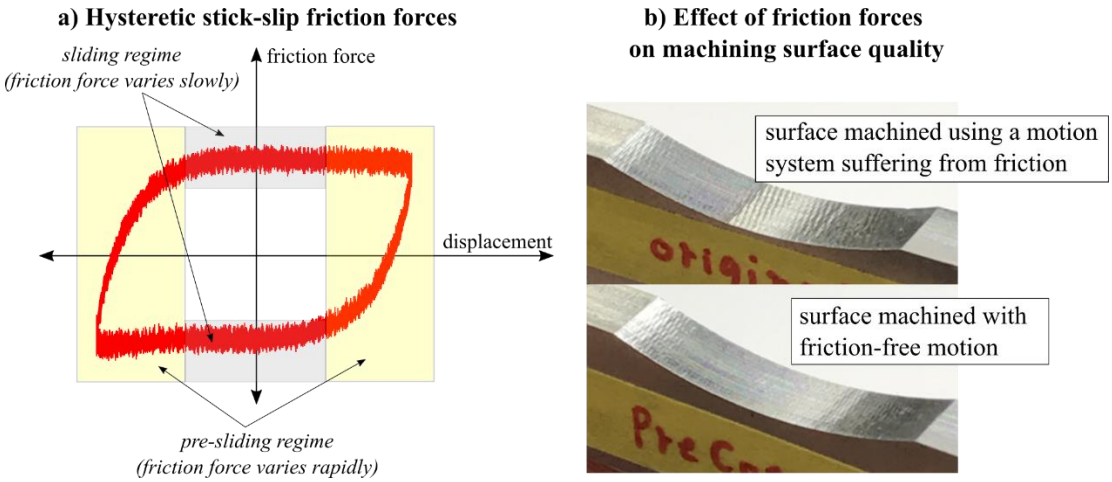

Figure 3. Hysteretic stick-slip behavior of friction forces w.r.t. displacement (a) and the effect of friction forces on surface quality in precision machining applications (b) [14].

In this dissertation, strategies for mitigating dynamic errors and increasing achievable positioning accuracy of precision mechatronic systems are presented. The dissertation consists of 5 papers appearing in or submitted to *IEEE/ASME Transactions on Mechatronics* and/or *CIRP Annals – Manufacturing Technology* journals. Each paper is presented in a separate section. Section 2 presents a robust trajectory generation algorithm to generate multi-axis position, velocity, acceleration, and jerk commands to avoid exciting lightly damped column vibrations commonly seen in modern machine tools and 3D-Printer systems (see Figure 2). Sections 3 and 4 present trajectory shaping (pre-compensating) strategies to eliminate dynamic positioning errors induced by servo-controller dynamics, structural vibrations of motion transmission components (see Figure 2), and pre-motion (pre-sliding/pre-rolling) friction forces (see Figure 3). In section 5 and 6, motion control algorithms are presented to improve stability margins of turning processes by utilizing a piezo-actuated cutting tool assembly. Finally, section 7 summarizes the contributions of this dissertation and provides a conclusion.

ROBUST TRAJECTORY GENERATION FOR MULTIAXIS VIBRATION AVOIDANCE

Alper Dumanli and Burak Sencer

IEEE/ASME Transactions on Mechatronics
Volume 25, No. 6, December 2020, Pages 2938-2949

2. Robust Trajectory Generation for Multiaxis Vibration Avoidance

Precision manufacturing equipment suffer from unwanted vibrations triggered in rapid motion. Unless mitigated, these vibrations limit achievable accuracy and productivity of motion systems. This article presents a novel technique to generate reference motion trajectories that can robustly avoid triggering unwanted inertial vibrations. The reference trajectory is defined in B-spline form, and its frequency spectrum is optimized to attenuate spectral energy in a desired frequency band to avoid excitation of unwanted vibrations. A novel time-domain smoothing objective is also proposed to improve tracebility of generated trajectories. The trajectory optimization problem is put in a convex form, and a novel windowing scheme is designed to solve it efficiently for real-time implementation. Robustness and effectiveness of the proposed method is validated experimentally on an industrial three-axis Cartesian machine tool. Experiments show that the proposed method can robustly avoid unwanted structural vibrations without introducing delay to the motion and outperform state-of-the-art prefiltering methods.

2.1. Introduction

Speed and accuracy are contradicting objectives for modern manufacturing equipment such as industrial robots [3], computer numerical control (CNC) machine tools [10], three-dimensional printers [11], or even gantry [20] cranes and conveyor systems. High speed and acceleration induce positioning errors and trigger unwanted vibrations. Although servo positioning errors can be eliminated through effective use of feedforward control [5], unwanted vibrations cannot be easily mitigated due to complex coupled dynamics of the machine structure. As the axes in motion accelerate and decelerate, inertial forces excite the structure. When frequency spectrum of this excitation matches lightly damped resonances, it induces unwanted forced vibrations. These vibrations elongate settling time [3] or even damage safe manipulation of pay loads on industrial robots. For precision manufacturing equipment, unwanted vibrations may easily destroy surface finish quality [10]. Similarly, in semiconductor

manufacturing, they limit the achievable productivity and accuracy of the equipment [21].

Structural vibrations can be dampened by employing additional hardware. These add-on dampers can be passive [22] or active [23]. Tuned-mass-dampers [22] are some of the widely used passive damper systems. Active dampers provide greater robustness. Nevertheless, they require additional sensors and actuators [24], which make them costly; they consume significantly more energy, and their application is limited by design constraints.

Active vibration suppression can also be realized by utilizing the existing actuator and sensors. If vibration modes are controllable and observable by actuators and sensors already existing in the equipment, active damping can be achieved directly by feedback control. The most common approach is use of feed-drive systems and by design of mode-compensating(damping) controllers. Pole placement control [5], [25], [1] is widely used. Dumanli and Sencer [6] designed a non-collocated linear quadratic regulator for optimal placement of rigid body and structural vibration modes for best performance. Linear parameter varying control strategies are also proposed [26] for increased robustness against parameter variations. In [27], rotor vibrations are controlled actively. In [21], a nonlinear controller design is proposed based on Heuristics on vibratory behavior and Lyapunov analysis.

These active vibration control schemes have two shortcomings. First, a robust controller must be designed for practical implementation. Second, controllability and observability of the modes are limited. Most industrial systems suffer from crosstalk, where vibration modes are coupled and cannot be observed without additional measurement points and sensor systems [10], [28]. Therefore, the use of passive techniques such as introducing a notch filter into the controller becomes more favorable. Notch filters remove the spectral energy from control signal around target frequencies. They can help avoid exciting lightly damped modes in the system. However, introducing notch filters into the feedback control loop limits achievable tracking bandwidth and at the same time degrades dynamic stiffness of the servo system [5], [29] which makes them not suitable for high performance positioning systems.

One way to overcome deficiencies of notch filters is to shift the filtering into the feedforward control. Singer and Seering [30] pioneered this approach by designing the first input shaper (IS) filter. ISs are essentially finite impulse response (FIR)-based notch filters that filter the reference command trajectory to control frequency spectrum of the inertial forces during rapid motion. Nevertheless, ISs introduce a motion delay that is inversely proportional to the notch frequencies. Typically, the cycle time elongation due to IS is shorter than the settling time of the vibration for lightly damped structural modes. As a result, it still makes ISs favorable for generating vibration-less point-to-point (P2P) motion. However, IS-induced delay is detrimental in multiaxis contouring. When interpolating spline, circular, or even multisegmented linear toolpaths, shaper delay causes large contouring errors [10], [31]. Therefore, ISs are avoided in multiaxis contouring motion unless those errors are pre-compensated [32]. In practice robust ISs with wider attenuation bandwidth [33] should be employed, or multiple ISs must be used to accommodate parameter variations and introduce robustness to the operation.

To overcome drawbacks of ISs, model-less trajectory generation approaches have been developed. Most modern motion systems generate reference trajectories with continuous acceleration and jerk. Flash and Hogan [34] showed that smooth motion of humans is generated by minimizing the jerk. Industrial robot systems use min.-jerk trajectories for generating rapid and accurate end-effector trajectories [35]. Altintas and Erkorkmaz [36], adopted this approach on CNC machine tools [37]. Since jerk is the derivative of acceleration, it controls high frequency spectrum of the trajectory. Even though this implies that a min.-jerk trajectory will have less excitation at high frequencies, it cannot quantitatively control the trajectory's frequency spectrum, which is critical for avoiding unwanted forced vibrations in precision equipment.

To overcome this, Sencer and Tajima optimized reference trajectories with respect to their frequency spectrum [38]. Since this approach optimizes the profile in a fixed Fourier window, residual vibration at the end of a motion window is avoided. For longer toolpaths, unwanted vibration may still be observed. Furthermore, application of this method on curved, spline toolpaths is limited due to the nonlinearity of toolpath kinematics [10]. Duan and Okwudire [11] addressed this by designing a nonlinear FIR

filter for inverting individual drive dynamics with nonminimum phase zeros. They were able to generate vibrationless motion on long toolpaths. However, their method requires precise identification of structural dynamics, which is limited in practice.

This article proposes a novel reference trajectory generation method that overcomes deficiencies of the above techniques. In-stead of relying on filtering, frequency spectrum of the reference tangential acceleration profile [10] is optimized using a convex optimization scheme to robustly mitigate residual vibrations in linear P2P and complex curved toolpaths. Section II outlines the basis of the method and application on P2P toolpaths, whereas Section III presents solution of the convex optimization problem for complex curved toolpaths. An efficient windowing scheme is presented in Section IV to plan frequency optimal trajectories for long toolpaths. Section V presents experimental implementation and benchmarks against state-of-the-art techniques [30], [39].

2.2. Optimal Trajectory Generation for Vibration Avoidance in P2P Linear Interpolation

Numerical control (NC) unit of servo control systems generates (plans) reference motion trajectories consisting of position ($s(k)$), velocity ($\dot{s}$), acceleration ($\ddot{s}$), and jerk ($\dddot{s}$) profiles, and commands them to the axis servo controllers in real-time at a fixed servo control interval, T_s [sec]. The torque/force delivered by the servo motors are proportional to the reference acceleration (s). Due to rich frequency spectrum of the acceleration, lightly damped modes of the servo system or the machine structure maybe excited during high-speed motion causing unwanted residual vibrations. In an effort to avoid unwanted vibrations, frequency spectrum of the reference acceleration must be controlled infrequency domain around critical modes of the structure. This objective is achieved by minimizing the discrete Fourier trans-form of acceleration in a frequency band [ω_1, ω_M] as also reported in [10]:

$$\underset{s(t)}{\text{minimize}}(J),$$

where: (2.1)

$$J=\sum_{l=1}^{M}\left(\sum_{k=1}^{N}\mathrm{Re}(e^{-j\omega_l t_k})\ddot{s}_k\right)^2+\sum_{l=1}^{M}\left(\sum_{k=1}^{N}\mathrm{Im}(e^{-j\omega_l t_k})\ddot{s}_k\right)^2$$

where N is the number of samples in the Fourier window, and $1/M$ the frequency resolution. Note that attenuating frequency spectrum in a band ensures robustness to avoid residual vibrations. The objective function in (2.1) is put in compact matrix-vector form:

$$\underset{\mathbf{s}}{\text{minimize}}\left\|\mathbf{W}\ddot{\mathbf{s}}\right\|_2^2 \tag{2.2}$$

where $\ddot{\mathbf{s}}$ is the sampled acceleration profile, i.e., $\ddot{\mathbf{s}}=[\ddot{s}_1, \ddot{s}_2, \ldots, \ddot{s}_N]^T$, and $\mathbf{W}$ is the $2M\times N$ discrete Fourier kernel generated for the target attenuation band $[\omega_1, \omega_M]$ as:

$$\mathbf{W}=\begin{bmatrix}
\mathrm{Re}\left\{e^{-j\omega_1 t_1}\right\} & \mathrm{Re}\left\{e^{-j\omega_1 t_2}\right\} & \ldots & \mathrm{Re}\left\{e^{-j\omega_1 t_N}\right\}\\
\vdots & \vdots & \ddots & \vdots\\
\mathrm{Re}\left\{e^{-j\omega_M t_1}\right\} & \mathrm{Re}\left\{e^{-j\omega_M t_2}\right\} & \ldots & \mathrm{Re}\left\{e^{-j\omega_M t_N}\right\}\\
\mathrm{Im}\left\{e^{-j\omega_1 t_1}\right\} & \mathrm{Im}\left\{e^{-j\omega_1 t_2}\right\} & \ldots & \mathrm{Im}\left\{e^{-j\omega_1 t_N}\right\}\\
\vdots & \vdots & \ddots & \vdots\\
\mathrm{Im}\left\{e^{-j\omega_M t_1}\right\} & \mathrm{Im}\left\{e^{-j\omega_M t_2}\right\} & \ldots & \mathrm{Im}\left\{e^{-j\omega_M t_N}\right\}
\end{bmatrix} \tag{2.3}$$

The objective is to determine the reference acceleration profile $\ddot{\mathbf{s}}$ that minimizes the objective function in (2.2). In this article, reference acceleration profile is defined in B-spline form [40]. This will be the foundation for numerically stable and efficient generation of frequency optimal reference motion profiles. Trajectory profiles in B-spline form can be written in compact vector-matrix from as:

$$\mathbf{s} = \mathbf{B}\mathbf{q}, \quad \dot{\mathbf{s}} = \dot{\mathbf{B}}\mathbf{q}, \quad \ddot{\mathbf{s}} = \ddot{\mathbf{B}}\mathbf{q}$$

where:

$$\mathbf{B} = \begin{bmatrix} B_{1,n}(t_1) & B_{2,n}(t_1) & \dots & B_{P,n}(t_1) \\ B_{1,n}(t_2) & B_{2,n}(t_2) & \dots & B_{P,n}(t_2) \\ \vdots & \vdots & \ddots & \vdots \\ B_{1,n}(t_N) & B_{2,n}(t_N) & \dots & B_{P,n}(t_N) \end{bmatrix}_{N \times P} \tag{2.4}$$

$$B_{m,n}(t) = \frac{t - \mathbf{g}_m}{\mathbf{g}_{m+n} - \mathbf{g}_m} B_{m,n-1}(t) n + \frac{\mathbf{g}_{m+n+1} - t}{\mathbf{g}_{m+n+1} - \mathbf{g}_{m+n}} B_{m+1,n-1}(t)$$

$$B_{m,0}(t) = \begin{cases} 1 & \mathbf{g}_m \le t \le \mathbf{g}_{m+1} \\ 0 & \text{otherwise} \end{cases}$$

Notice that $\mathbf{q} \in \mathbb{R}^P$ is the optimal control point vector, which is to be determined to minimize J defined in (2.1). As shown in Figure 4, shape of the acceleration profile is controlled by control points $\mathbf{q}$ based on the basis function matrix $\mathbf{B}$, which consists of n^{th} order basis polynomials evaluated at a fixed sampling interval $\mathbf{B}(t=kT_s)$. $n>3$ should be selected to ensure a jerk-continuous acceleration profile. $\mathbf{g}$ is the homogeneous knot vector. $\dot{\mathbf{B}}$ and $\ddot{\mathbf{B}}$ are the first and second order time derivatives of $\mathbf{B}$.

Residual vibrations are only triggered during acceleration/deceleration transients. Therefore, the B-spline-based frequency-optimal acceleration profile is used to plan the acceleration transients between target velocities v_{init} and v_{final}. This is achieved by introducing kinematic boundary conditions. First, initial and final zero acceleration and jerk constraints are imposed to ensure smooth and continuous motion, i.e., $a_{init}=a_{final}=0$, $j_{init}=j_{final}=0$. Next, initial and final velocity constraints (v_{init}, v_{final}) are imposed to ensure target velocity traverse is achieved. Finally, initial position constraint is imposed, $s_{init}=0$. These constraints can be postulated as linear equality constraints by making use of the B-spline basis representation of the trajectory from (2.4) as:

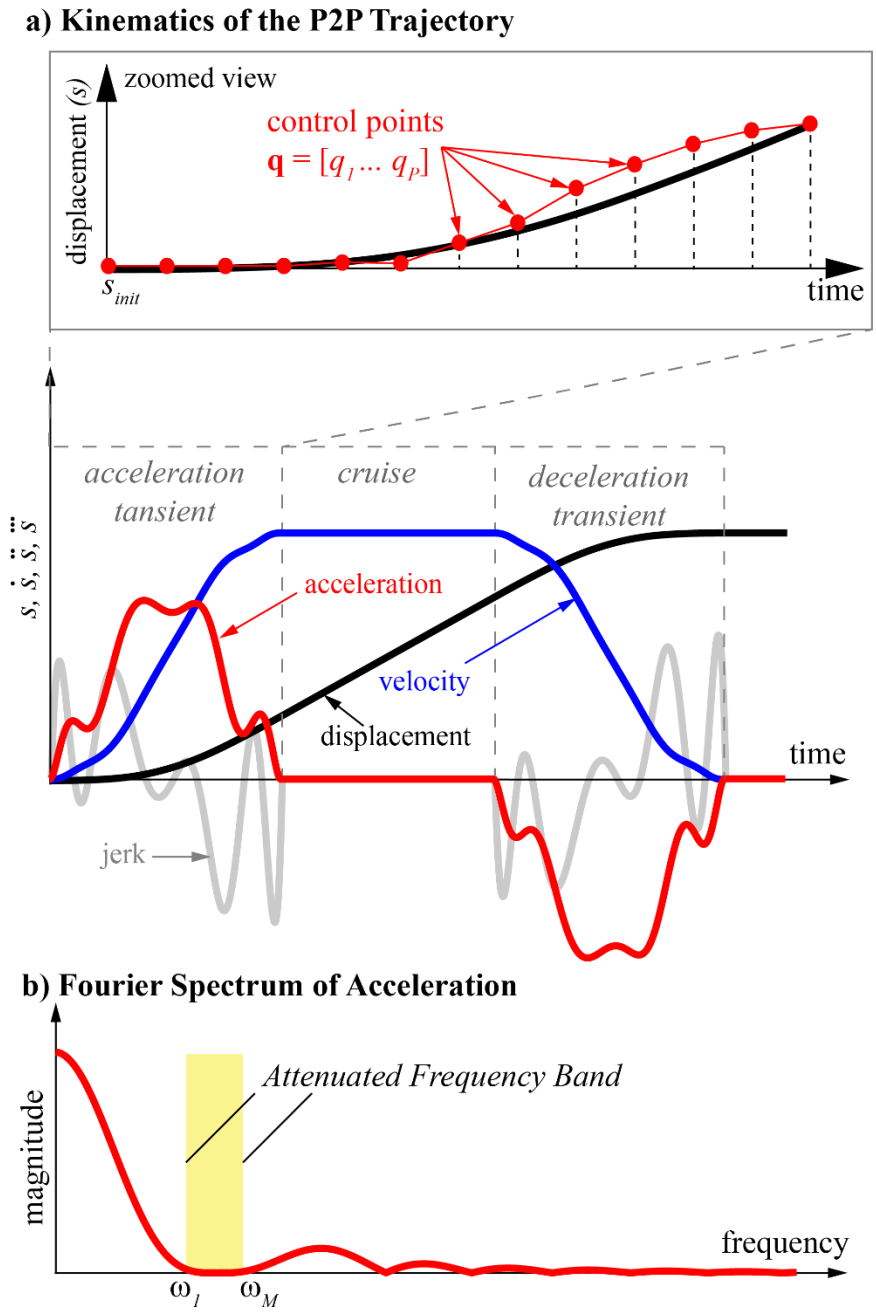

Figure 4. Illustration of frequency optimal displacement, velocity, acceleration and jerk profiles.

$$\underbrace{\begin{bmatrix} \mathbf{B}_{1,1} & \mathbf{B}_{1,2} & \dots & \mathbf{B}_{1,P} \\ \mathbf{B}_{N,1} & \mathbf{B}_{N,2} & \dots & \mathbf{B}_{N,P} \\ \dot{\mathbf{B}}_{1,1} & \dot{\mathbf{B}}_{1,2} & \dots & \dot{\mathbf{B}}_{1,P} \\ \dot{\mathbf{B}}_{N,1} & \dot{\mathbf{B}}_{N,2} & \dots & \dot{\mathbf{B}}_{N,P} \\ \ddot{\mathbf{B}}_{1,1} & \ddot{\mathbf{B}}_{1,2} & \dots & \ddot{\mathbf{B}}_{1,P} \\ \ddot{\mathbf{B}}_{N,1} & \ddot{\mathbf{B}}_{N,2} & \dots & \ddot{\mathbf{B}}_{N,P} \\ \dddot{\mathbf{B}}_{1,1} & \dddot{\mathbf{B}}_{1,2} & \dots & \dddot{\mathbf{B}}_{1,P} \\ \dddot{\mathbf{B}}_{N,1} & \dddot{\mathbf{B}}_{N,2} & \dots & \dddot{\mathbf{B}}_{N,P} \end{bmatrix}}_{\mathbf{L}} \mathbf{q} = \underbrace{\begin{bmatrix} s_{init} \\ s_{final} \\ v_{init} \\ v_{final} \\ a_{init} \\ a_{final} \\ j_{init} \\ j_{final} \end{bmatrix}}_{\mathbf{p}} \tag{2.5}$$

The optimization problem is postulated by combining the objective function from (2.2) to control frequency spectrum of the acceleration profile and the constraints from (2.5) to impose boundary conditions as:

$$\underset{\mathbf{q}}{\text{minimize}} \left\| \mathbf{W}\ddot{\mathbf{B}}\mathbf{q} \right\|_2^2, \quad \text{subject to: } \mathbf{L}\mathbf{q} = \mathbf{p} \tag{2.6}$$

Equation (2.6) is a linear least squares minimization problem with equality constraints. Employing vector of Lagrange Multipliers ($\boldsymbol{\lambda}$), following linear system of equations can be solved analytically to obtain optimal control points **q** that govern the reference trajectory with desired frequency spectrum:

$$\begin{bmatrix} (\ddot{\mathbf{B}}^T \mathbf{W}^T \mathbf{W} \ddot{\mathbf{B}})_{P\times P} & \mathbf{L}^T_{P\times 8} \\ \mathbf{L}_{8\times P} & \mathbf{0}_{8\times 8} \end{bmatrix} \begin{bmatrix} \mathbf{q}_{P\times 1} \\ \boldsymbol{\lambda}_{8\times 1} \end{bmatrix} = \begin{bmatrix} \mathbf{0}_{P\times 1} \\ \mathbf{p}_{8\times 1} \end{bmatrix} \tag{2.7}$$

P2P trajectories start from zero initial velocity and accelerate toa target cruise feedrate, which is then followed by a deceleration transient to reach a full stop as shown in Figure 4.a. Above approach only plans the acceleration/deceleration transients. This results in an acceleration frequency spectrum illustrated in Figure 4.b, where the frequency components between$\omega_1$and$\omega_M$are attenuated to avoid residual vibrations. The deceleration portion can be planned similarly by swapping the initial and final kinematic constraints. It should also be noted that only the initial position boundary condition is imposed in generating the acceleration transient. Displacement traveled during acceleration phase is known once the profile is planned, and it is subtracted by the total travel distance to calculate the cruise (constant speed) motion duration.

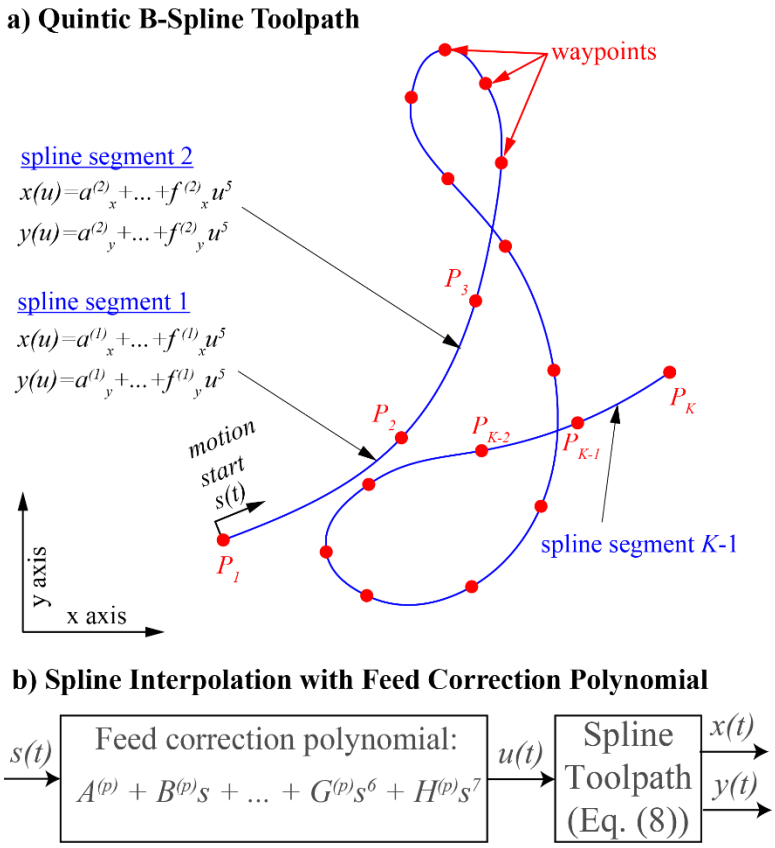

Figure 5. Multiaxis spline interpolation strategy. (a) Quintic B-spline tool-path. (b) Spline interpolation with feed correction polynomial.

Multiaxis P2P motion can be planned using the trajectory shown in Figure 4.a. Since axis accelerations are linear projections of the path acceleration $\ddot{s}$(t), i.e., $\ddot{x}(t) = \ddot{s}(t)\cos(\alpha)$ and $\ddot{y}(t) = \ddot{s}(t)\sin(\alpha)$, simply tuning frequency spectrum of tangential feed(velocity) profile is sufficient. However, for curved tool paths such as arcs and splines, the axis kinematic profiles are controlled by the tangential feed profile as well as the continuously varying curvature of the path geometry [10]. Next section presents convex optimization of tangential trajectory profiles for robust vibration avoidance along complex curved toolpaths.

2.3. Optimal Trajectory Generation for Vibration Avoidance in Spline Interpolation

Spline interpolation is commonly used in machining [39] and additive manufacturing [2] processes. Spline toolpaths are either defined in the B-spline [41], NURBS or in cubic (3rd order) or quintic (5th order) polynomial form [42]. NURBS and B-spline representations can be mapped to their basic polynomial form [43]. Quintic spline paths [44] ensure C^2 continuous motion that is most suitable for high-speed motion. Figure 5 shows an example Quintic spline toolpath. Fifth-order polynomials are used to interpolate continuous motion between knots (waypoint) and axis positions are defined as:

$$\begin{aligned} x(u) &= a_x^{(p)} + b_x^{(p)}u + c_x^{(p)}u^2 + d_x^{(p)}u^3 + e_x^{(p)}u^4 + f_x^{(p)}u^5 \\ y(u) &= a_y^{(p)} + b_y^{(p)}u + c_y^{(p)}u^2 + d_y^{(p)}u^3 + e_y^{(p)}u^4 + f_y^{(p)}u^5 \end{aligned} \tag{2.8}$$

where $u \in [0,\ l_p]$ [42] is the spline parameter and $a...f_x^{(p)}$ and $a...f_y^{(p)}$ are spline coefficients of each segment $p=1...K-1$ (see Figure 5.a), where K is the total number of waypoints. C^2 motion is achieved by ensuring zeroth-, first- and second-order geometric continuity constraints at each knot as

$$\begin{aligned} x^{(p)}(0) &= x^{(p-1)}(l_p), & y^{(p)}(0) &= y^{(p-1)}(l_p) \\ \frac{dx^{(p)}}{du}(0) &= \frac{dx^{(p-1)}}{du}(l_p), & \frac{dy^{(p)}}{du}(0) &= \frac{dy^{(p-1)}}{du}(l_p) \\ \frac{d^2x^{(p)}}{du^2}(0) &= \frac{d^2x^{(p-1)}}{du^2}(l_p), & \frac{d^2y^{(p)}}{du^2}(0) &= \frac{d^2y^{(p-1)}}{du^2}(l_p) \end{aligned} \tag{2.9}$$

where $x^{(p)}$ and $y^{(p)}$ are displacement polynomials for the p^{th} segment, and l_p is its Euclidean length between waypoints.

The relationship between the spline parameter u and the arc displacement s are nonlinear due to the varying curvature of the toolpath. Therefore, the spline parameter u for each arc displacement must be computed either iteratively [44] or by mapping [42]. Here, the feed correction polynomial approach from Erkorkmaz [42] is adapted, and the relationship between spline parameter and arc displacement is captured by a seventh-order polynomial:

$$u = A^{(p)} + B^{(p)}s + ... + G^{(p)}s^6 + H^{(p)}s^7 \tag{2.10}$$

As shown in Figure 5.b, once arc displacement $s(t)$ is commanded, corresponding spline parameter is obtained from (2.10) and the axis position, velocity, and accelerations profiles are interpolated.

Axis kinematics are controlled by the tangential velocity and acceleration as well as the geometrical path derivatives. The relation between axis velocities ($\dot{x}$, $\dot{y}$), tangential velocity ($\dot{s}$) and toolpath geometry (x',y') is obtained by applying the chain rule on (2.8) and (2.10):

$$\dot{\mathbf{x}} = \frac{\partial \mathbf{x}(s)}{\partial s}\dot{\mathbf{s}} = \mathbf{x}'\dot{\mathbf{s}}, \quad \dot{\mathbf{y}} = \frac{\partial \mathbf{y}(s)}{\partial s}\dot{\mathbf{s}} = \mathbf{y}'\dot{\mathbf{s}} \tag{2.11}$$

and axis accelerations are obtained as:

$$\begin{aligned} \ddot{\mathbf{x}} &= \frac{\partial^2 \mathbf{x}(s)}{\partial s^2}\dot{\mathbf{s}}^2 + \frac{\partial \mathbf{x}(s)}{\partial s}\ddot{\mathbf{s}} = \mathbf{x}''\dot{\mathbf{s}}^2 + \mathbf{x}'\ddot{\mathbf{s}} \\ \ddot{\mathbf{y}} &= \frac{\partial^2 \mathbf{y}(s)}{\partial s^2}\dot{\mathbf{s}}^2 + \frac{\partial \mathbf{y}(s)}{\partial s}\ddot{\mathbf{s}} = \mathbf{y}''\dot{\mathbf{s}}^2 + \mathbf{y}'\ddot{\mathbf{s}} \end{aligned} \tag{2.12}$$

Typically, geometric path derivatives (∂x/∂s, ∂y/∂s) are evaluated along the arc displacement in advance and stored in memory. They are then used for calculating axis velocity and acceleration commands. This strategy is essential for computationally efficient planning of time-optimal reference trajectories and widely adapted for real-time interpolation [42].

2.3.1. Frequency Domain Optimization for Residual Vibration Avoidance

As introduced in the previous section, tangential feed profile combined with the geometric derivatives of the toolpath control axis kinematic profiles. Here, the idea is to plan the tangential feed/acceleration profiles ($\ddot{s}(t)$) to shape frequency spectrum of the reference axis acceleration profiles and thereby avoid un-wanted vibrations. In this article, robust vibration attenuation is achieved by jointly shaping the tangential trajectory kinematics based on weighted frequency and time-domain objectives.

First, tangential acceleration profile $\ddot{s}(t)$ is planned to ensure that axis acceleration profiles $\ddot{x}(t)$ and $\ddot{y}(t)$ have minimum spectral energy within a desired frequency band. This guarantees that residual vibrations at the end of a Fourier window is eliminated. Similar to (2.2), this frequency domain objective is postulated as:

$$\underset{\mathbf{s}}{\text{minimize}}\left(\left\|\mathbf{W}\ddot{\mathbf{x}}\right\|_2^2+\left\|\mathbf{W}\ddot{\mathbf{y}}\right\|_2^2\right) \tag{2.13}$$

where $\mathbf{W}$ is the Fourier Kernel from (3). $\ddot{\mathbf{x}}=\begin{bmatrix}\ddot{x}_1 & \ddot{x}_2 & \cdots & \ddot{x}_N\end{bmatrix}^T$ and $\ddot{\mathbf{y}}=\begin{bmatrix}\ddot{y}_1 & \ddot{y}_2 & \cdots & \ddot{y}_N\end{bmatrix}^T$ are the sampled axis acceleration commands.

Note that, unlike linear interpolation, axis acceleration pro-files are controlled by both tangential velocity and acceleration as well as the path derivatives in spline interpolation (see (2.12)). This introduces two crucial nonlinearities that prevent convex formulation of the optimization problem. First, square of tangential velocity $\dot{\mathbf{s}}^2$ appears in (2.12) and poses a direct nonlinearity. Second, the first- and second-order path derivatives (x', x'', y', and y'') in (2.12) are defined as high order polynomials and vary with the arc length along toolpath. These nonlinearities banish convex minimization of (2.13). In order to circumvent them and recover the convexity of the optimization objective, the following steps are taken.

First, in an effort to eliminate the $\dot{\mathbf{s}}^2$ term, axis accelerations are simply obtained from backward differentiation of axis velocity profiles in frequency domain:

$$\begin{aligned}\mathcal{F}\left(\ddot{x}(t)\right)&\approx\frac{\left(1-e^{-j\omega T_s}\right)}{T_s}\mathcal{F}\left(\dot{x}(t)\right)\\ \mathcal{F}\left(\ddot{y}(t)\right)&\approx\frac{\left(1-e^{-j\omega T_s}\right)}{T_s}\mathcal{F}\left(\dot{y}(t)\right)\end{aligned} \tag{2.14}$$

where $\mathcal{F}(.)$ is the Fourier transform operator, i.e., $\mathcal{F}(\ddot{x}(t))=\int_{t=0}^{\infty}\ddot{x}(t)e^{-j\omega t}dt$. Since sampling time in modern CNC systems are around 0.5–1 [msec], this approach provides high-fidelity acceleration kinematics. Another benefit of the above approach is that the second-order path derivatives x'' and y'' are no longer required, which partially eliminates the second nonlinearity. However, first-order geometric derivatives x' and y' are arc dis-placement dependent and are still required. This nonlinearity is overcome by relaxing the displacement dependency as follows.

The toolpath is first interpolated at constant speed by a smooth “template” feed profile, se. Planning of a constant feed template motion profile is computationally insignificant [36], and path derivatives at sampled displacement points s(t=kTs),dx/ds,dy/ds can be stored in a lookup table for further evaluation. As long as

the generated displacement profiles and the template displacement profile s_e are sufficiently close, $|s-s_e|<\epsilon$, stored path derivatives can be used safely in planning optimal feed profiles. Keeping the discrepancy $\epsilon \leq 200$ [μm] ensures accurate evaluation of axis accelerations.

Finally, the objective function for generating the frequency optimal trajectory originally given in (2.13) is repostulated as a linear least-squares problem to minimize frequency spectrum of axis accelerations as:

$$\begin{aligned} &\underset{\mathbf{q}}{\text{minimize}} \left\| \mathbf{W}_D \left(\mathbf{x}'(s_e) \circ (\dot{\mathbf{B}}\mathbf{q}) \right) \right\|_2^2 + \left\| \mathbf{W}_D \left(\mathbf{y}'(s_e) \circ (\dot{\mathbf{B}}\mathbf{q}) \right) \right\|_2^2 \\ &\text{subject to: } \mathbf{s}_e - \epsilon \leq \mathbf{B}\mathbf{q} \leq \mathbf{s}_e + \epsilon \end{aligned} \tag{2.15}$$

where ◦ denotes Hadamard (entry-wise) vector product. The inequality constraints guarantee that s_e is sufficiently close to s. The regressor matrices in above optimization objective ($\mathbf{W}_D \text{diag}(x')(s_e)\dot{\mathbf{B}}$ and $\mathbf{W}_D \text{diag}(y')(s_e)\dot{\mathbf{B}}$) contain $\mathbf{W}_D$ instead of $\mathbf{W}$, where $\mathbf{W}_D$ is the Fourier differentiation matrix obtained using (2.14) and given as:

$$\mathbf{W}_D \triangleq \frac{1}{T_s}(\mathbf{W} - \mathbf{W}_\delta)$$

where:

$$\mathbf{W}_\delta = \begin{bmatrix} \text{Re}\left\{e^{-j\omega_1(t_1+T_s)}\right\} & \dots & \text{Re}\left\{e^{-j\omega_1(t_N+T_s)}\right\} \\ \vdots & \ddots & \vdots \\ \text{Re}\left\{e^{-j\omega_M(t_1+T_s)}\right\} & \dots & \text{Re}\left\{e^{-j\omega_M(t_N+T_s)}\right\} \\ \text{Im}\left\{e^{-j\omega_1(t_1+T_s)}\right\} & \dots & \text{Im}\left\{e^{-j\omega_1(t_N+T_s)}\right\} \\ \vdots & \ddots & \vdots \\ \text{Im}\left\{e^{-j\omega_M(t_1+T_s)}\right\} & \dots & \text{Im}\left\{e^{-j\omega_M(t_N+T_s)}\right\} \end{bmatrix} \tag{2.16}$$

As a result, frequency optimal reference motion trajectories can be solved through convex optimization, and global optimum is sought.

2.3.2. Time Domain Optimization for Forced Vibration Avoidance

The optimization objective formulated in the previous section minimizes frequency spectrum of the trajectory (15) within a desired frequency band. This band is designed to robustly encapsulate natural frequencies of vibratory modes of the

structure. It attenuates residual vibrations that occur at the end of an acceleration transient. In other words, residual vibrations are eliminated when the acceleration phase is completed. If the acceleration phase is long, forced vibrations may be triggered and deteriorate the performance before they are cancelled.

Unwanted forced vibrations during long acceleration transients are avoided by augmenting the original frequency domain objective function with the time domain response. In this article, the difference between reference acceleration ($\ddot{x}$) and acceleration response of a lightly damped vibratory system ($\ddot{x}_{act}$) is considered to eliminate forced vibrations in time domain (i.e., $\ddot{x} - \ddot{x}_{act}$), and it is called the "acceleration response error." Series of lightly damped oscillators are used to estimate residual vibrations from:

$$G(\xi) = \prod_{i=1}^{Q} \frac{\omega_{n,i}^2}{\xi^2 + 2\zeta_i \omega_{n,i} \xi + \omega_{n,i}^2} \tag{2.17}$$

where ξ is the Laplace-domain frequency variable, ζ_i and $\omega_{n,i}$ are the damping ratio and the natural frequency of the i^{th} mode. Note that each $\omega_{n,i}$ is selected to lie within the target frequency attenuation band. The optimization problem to penalize acceleration response error is defined as:

$$\underset{\mathbf{q}}{\text{minimize}} \left\| \underset{\ddot{\mathbf{x}}}{\ddot{\mathbf{B}}\mathbf{q}} - \mathbf{G} \underset{\ddot{\mathbf{x}}_{act}}{\ddot{\mathbf{B}}\mathbf{q}} \right\|_2^2 \tag{2.18}$$

where **G** is the discretized convolution matrix, which is obtained from the lifted-domain representation of $G(\xi)$ as:

$$\mathbf{G} = \begin{bmatrix} 0 & 0 & \dots & \dots & 0 \\ \mathbf{c}^T\mathbf{b} & 0 & \dots & \dots & 0 \\ \mathbf{c}^T\mathbf{A}\mathbf{b} & \mathbf{c}^T\mathbf{b} & \dots & \dots & 0 \\ \vdots & \vdots & \ddots & \ddots & \vdots \\ \mathbf{c}^T\mathbf{A}^{N-2}\mathbf{b} & \mathbf{c}^T\mathbf{A}^{N-3}\mathbf{b} & \dots & \mathbf{c}^T\mathbf{b} & 0 \end{bmatrix} \tag{2.19}$$

with:

$$\mathbf{z}(k+1) = \mathbf{A}\mathbf{z}(k) + \mathbf{b}u(k), \quad z_{out}(k) = \mathbf{c}^T\mathbf{z}(k)$$

where **A**, **b**, and **c** are state transition, input, and output matrices of $G(\xi)$, respectively. Axis accelerations are derived from differentiation of axis velocities using the following filter:

$$D(z) = \frac{z-1}{T_s(z-e^{-2\pi f_c})} \tag{2.20}$$

where z is the z-transform frequency variable, T_s is the sampling time, and f_c is the cutoff frequency of the filter. $D(z)$ behaves as a numerical differentiator for frequencies smaller than f_c. With this modification, the optimization problem from (2.18) is augmented to:

$$\begin{aligned} &\underset{\mathbf{q}}{\text{minimize}} \left(\left\| (\mathbf{D}-\mathbf{DG}) \left(\mathbf{x}'(s_e) \circ (\dot{\mathbf{B}}\mathbf{q}) \right) \right\|_2^2 + \left\| (\mathbf{D}-\mathbf{DG}) \left(\mathbf{y}'(s_e) \circ (\dot{\mathbf{B}}\mathbf{q}) \right) \right\|_2^2 \right) \\ &\text{subject to:} \quad \mathbf{s}_e - \epsilon \le \mathbf{Bq} \le \mathbf{s}_e + \epsilon \end{aligned} \tag{2.21}$$

where **D** is the convolution matrix of $D(z)$. Equation (2.21) ensures that the response acceleration follows the reference acceleration, which implicitly suppresses any forced vibration that may occur. For best performance, an accurate system model could be used instead of a simple resonator as in (2.17).

Both the frequency (2.13) and the time domain (2.18) objectives attenuate excitation of lightly damped vibratory modes and have complementary strengths. The frequency domain objective in (2.13) provides robustness against parameter variations and guarantees suppression of residual vibrations in a wide attenuation band, whereas the time domain objective given in (2.18) provides suppression of forced vibrations that occur during a long acceleration transient. A weighted objective function is postulated to exploit the benefits of these two objectives as:

$$\begin{aligned} &\underset{\mathbf{q}}{\text{minimize}} \left(\begin{aligned} &\left\| \mathbf{W}_D \left(\mathbf{x}'(s_e) \circ (\dot{\mathbf{B}}\mathbf{q}) \right) \right\|_2^2 + \lambda_x \left\| (\mathbf{D}-\mathbf{DG}) \left(\mathbf{x}'(s_e) \circ (\dot{\mathbf{B}}\mathbf{q}) \right) \right\|_2^2 \cdots \\ &\qquad \cdots + \left\| \mathbf{W}_D \left(\mathbf{y}'(s_e) \circ (\dot{\mathbf{B}}\mathbf{q}) \right) \right\|_2^2 + \lambda_y \left\| (\mathbf{D}-\mathbf{DG}) \left(\mathbf{y}'(s_e) \circ (\dot{\mathbf{B}}\mathbf{q}) \right) \right\|_2^2 \end{aligned} \right) \\ &\text{subject to:} \mathbf{s}_e - \epsilon \le \mathbf{Bq} \le \mathbf{s}_e + \epsilon \end{aligned}$$

(2.22)

where λ_x and λ_y are the weights for x- and y-axis profiles. The ratio of singular values of the regressor matrices are employed so that above objectives are normalized against each other and well balanced by setting:

$$\lambda_x = \frac{\sigma_{max}\left(\mathbf{W}_D \text{diag}(\mathbf{x}'(s_e))\dot{\mathbf{B}}\right)}{\sigma_{max}\left((\mathbf{D}-\mathbf{DG})\text{diag}(\mathbf{x}'(s_e))\dot{\mathbf{B}}\right)}$$
$$\lambda_y = \frac{\sigma_{max}\left(\mathbf{W}_D \text{diag}(\mathbf{y}'(s_e))\dot{\mathbf{B}}\right)}{\sigma_{max}\left((\mathbf{D}-\mathbf{DG})\text{diag}(\mathbf{y}'(s_e))\dot{\mathbf{B}}\right)} \tag{2.23}$$

Equation (2.23) poses an optimization problem where a balance between forced and residual vibration avoidance is achieved through combining frequency and time domain objectives. Once this optimization objective is postulated, kinematic constraints for the motion can be introduced into the formulation. First, as defined in (2.6), boundary conditions need to be included to impose initial and final motion kinematic states, i.e., **Lq**=**p**. Additionally, it is desirable to introduce limits on axis accelerations to avoid actuator saturation. These requirements are introduced as a convex set of inequality constraints:

$$\underbrace{\begin{bmatrix} \mathbf{B} \\ -\mathbf{B} \\ \dot{\mathbf{B}} \\ -\dot{\mathbf{B}} \\ \mathbf{D}(\mathbf{x}'(s_e)\circ\dot{\mathbf{B}}) \\ -\mathbf{D}(\mathbf{x}'(s_e)\circ\dot{\mathbf{B}}) \\ \mathbf{D}(\mathbf{y}'(s_e)\circ\dot{\mathbf{B}}) \\ -\mathbf{D}(\mathbf{y}'(s_e)\circ\dot{\mathbf{B}}) \end{bmatrix}}_{\mathbf{C}} \mathbf{q} \leq \underbrace{\begin{bmatrix} \mathbf{s}_e + \epsilon \\ \epsilon - \mathbf{s}_e \\ v_{max} \\ v_{max} \\ \ddot{x}_{max} \\ \ddot{x}_{max} \\ \ddot{y}_{max} \\ \ddot{y}_{max} \end{bmatrix}}_{\mathbf{d}} \tag{2.24}$$

dsas where v_{max}, $\ddot{x}_{\max}$, and $\ddot{y}_{\max}$ are the maximum allowable tangential velocity and axis acceleration values, respectively. Notice that the tangential displacement constraint ensures geometric derivative accuracy and also included in (24). Imposing kinematic equality and inequality constraints onto (22), the final optimization problem is postulated as:

$$\begin{aligned}
&\underset{\mathbf{q}}{\text{minimize}}\left(J_F + J_T\right),\\
&\text{subject to: } \begin{Bmatrix}\mathbf{Lq} = \mathbf{p}\\ \mathbf{Cq} \le \mathbf{d}\end{Bmatrix}\\
&\text{with:}\\
&J_F = \left\|\mathbf{W}_D\left(\mathbf{x}'(s_e)\circ(\dot{\mathbf{B}}\mathbf{q})\right)\right\|_2^2 + \left\|\mathbf{W}_D\left(\mathbf{y}'(s_e)\circ(\dot{\mathbf{B}}\mathbf{q})\right)\right\|_2^2\\
&J_T = \lambda_x\left\|(\mathbf{D}-\mathbf{DG})\left(\mathbf{x}'(s_e)\circ(\dot{\mathbf{B}}\mathbf{q})\right)\right\|_2^2 + \lambda_y\left\|(\mathbf{D}-\mathbf{DG})\left(\mathbf{y}'(s_e)\circ(\dot{\mathbf{B}}\mathbf{q})\right)\right\|_2^2
\end{aligned} \tag{2.25}$$

In (2.25), JF refers to the frequency-domain objective, whereas JT indicates time-domain objective. This formulation allows us to generate multiaxis trajectories with optimal frequency spectrum in the axis-level. In the following section, a computationally efficient solution scheme is proposed for solving this convex optimization problem for longer toolpaths.

2.4. Windowing Approach for Long Trajectories

Proposed trajectory generation method can efficiently avoid unwanted vibrations within an attenuation band. However, for trajectories with longer motion duration (cycle time), size of the optimization problem grows in both number of optimization variables (control points, P) as well as the constraints imposed on the profile. Solving the convex problem globally in a single shot may not be suitable for real-time trajectory generation on a NC system. Instead, the problem is solved in "solution windows," and the feed profile is planned for portions of the toolpath which are then connected together. This approach is similar to model predictive control (MPC) control framework [45], also known as the "look-ahead" functionality, found in modern NC systems [46].

Typically, "windowing" approach is implemented by solving the feed optimization problem within a "displacement window(interval)" [46]. In other words, the problem has been solved in feed-displacement phase plane where the feedrate (velocity)is defined as a function of arc displacement. In this article, we keep the trajectory optimization problem in time-feedrate plane so that the Fourier transform and time domain behavior of the acceleration profile could be retained.

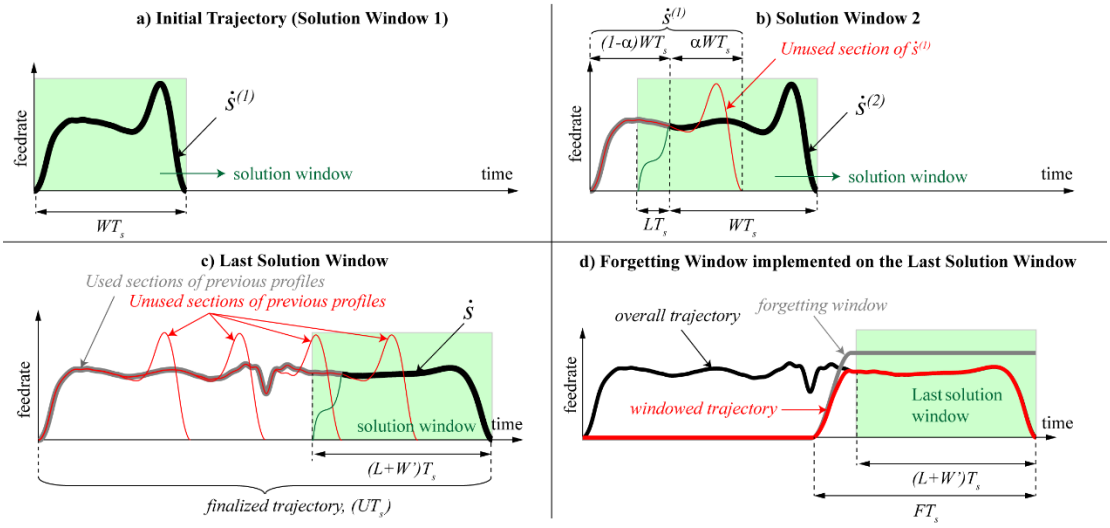

Figure 6. Windowing approach for efficient trajectory optimization for real-time implementation.

The presented solution is illustrated in Figure 6. Optimal feed profile is first solved for the first window ($\dot{s}^{(1)}$, see Figure 6.a) by imposing zero initial and final kinematic (velocity, acceleration, and jerk) constraints commanding a short start-stop motion. Control points only within a solution window are optimized to minimize the objective function. $\dot{s}^{(1)}$ is solved for W samples (WT_s [sec]), and i is the window counter. For this first window, the objective function (2.25) can be evaluated easily. Next, the window is shifted in time whereαcontrols the overlapping portion between successive windows (see Figure 6.b). For this subsequent window, the feed profile $\dot{s}^{(2)}$ is solved again with zero initial and final boundary conditions. In order to ensure sufficient duration for accelerating to the peak velocity, the window width is extended by L samples. Furthermore, to ensure that the feed profiles of successive windows are continuously connected; velocity, acceleration, and jerk constraints are introduced into the optimization problem as:

$$\begin{aligned} s^{(1)}\left((1-\alpha)WT_s\right) &= s^{(2)}(LT_s) \\ \dot{s}^{(1)}\left((1-\alpha)WT_s\right) &= \dot{s}^{(2)}(LT_s) \\ \ddot{s}^{(1)}\left((1-\alpha)WT_s\right) &= \ddot{s}^{(2)}(LT_s) \\ \dddot{s}^{(1)}\left((1-\alpha)WT_s\right) &= \dddot{s}^{(2)}(LT_s) \end{aligned} \tag{2.26}$$

Although objective function can be easily evaluated for the first window, care must be taken for its evaluation in the intermediate windows i >1. First, let us focus on the second solution window, i=2. The objective function in (2.25) contains both the Fourier transform of acceleration profile and the vibratory dynamics of the system. It requires time history, i.e., the past motion trajectory, so that vibration within the current solution window is accurately attenuated. One way to address this is to simply evaluate the objective function spanning from the motion start ($\dot{s}^{(1)}(0)$) to the end of the current solution window ($\dot{s}^{(2)}((L+W)T_s)$. Since past control points $\mathbf{q}^{(1)}$ are already solved, objective function affecting only the current unknown control points $\mathbf{q}^{(2)}$ within the current (i=2) solution window is solved from the following reduced optimization problem:

$$\underset{\mathbf{q}^{(2)}}{\text{minimize:}} \begin{cases} \left\| \mathbf{W}_D \left(\mathbf{x}'(s_e) \circ \begin{bmatrix} \dot{\mathbf{B}}^{(1)}\mathbf{q}^{(1)} \\ \dot{\mathbf{B}}^{(2)}\mathbf{q}^{(2)} \end{bmatrix} \right) \right\|_2^2 \\ + \left\| \mathbf{W}_D \left(\mathbf{y}'(s_e) \circ \begin{bmatrix} \dot{\mathbf{B}}^{(1)}\mathbf{q}^{(1)} \\ \dot{\mathbf{B}}^{(2)}\mathbf{q}^{(2)} \end{bmatrix} \right) \right\|_2^2 \\ + \lambda_x \left\| (\mathbf{D}-\mathbf{DG}) \left(\mathbf{x}'(s_e) \circ \begin{bmatrix} \dot{\mathbf{B}}^{(1)}\mathbf{q}^{(1)} \\ \dot{\mathbf{B}}^{(2)}\mathbf{q}^{(2)} \end{bmatrix} \right) \right\|_2^2 \\ + \lambda_y \left\| (\mathbf{D}-\mathbf{DG}) \left(\mathbf{y}'(s_e) \circ \begin{bmatrix} \dot{\mathbf{B}}^{(1)}\mathbf{q}^{(1)} \\ \dot{\mathbf{B}}^{(2)}\mathbf{q}^{(2)} \end{bmatrix} \right) \right\|_2^2 \end{cases} \tag{2.27}$$

subject to:

$$\begin{Bmatrix} \mathbf{L}\mathbf{q}^{(2)} = \mathbf{p} \\ \mathbf{C}\mathbf{q}^{(2)} \le \mathbf{d} \end{Bmatrix} \text{ and Eq. (2.26)}$$

where $\dot{\mathbf{B}}^{(1)}$ and $\dot{\mathbf{B}}^{(2)}$ are the first derivative of B-spline function matrices for the first and second solution windows defined as:

$$\dot{\mathbf{B}}^{(1)} = \begin{bmatrix} \dot{\mathbf{B}}_{1,1} & \dot{\mathbf{B}}_{1,2} & \cdots & \dot{\mathbf{B}}_{1,P_W} \\ \dot{\mathbf{B}}_{2,1} & \dot{\mathbf{B}}_{2,2} & \cdots & \dot{\mathbf{B}}_{2,P_W} \\ \vdots & \vdots & \ddots & \vdots \\ \dot{\mathbf{B}}_{(1-\alpha)W,1} & \dot{\mathbf{B}}_{(1-\alpha)W,2} & \cdots & \dot{\mathbf{B}}_{(1-\alpha)W,P_W} \end{bmatrix} \tag{2.28}$$

$$\dot{\mathbf{B}}^{(2)} = \begin{bmatrix} \dot{\mathbf{B}}_{L,1} & \dot{\mathbf{B}}_{L,2} & \cdots & \dot{\mathbf{B}}_{L,P_W} \\ \dot{\mathbf{B}}_{L+1,1} & \dot{\mathbf{B}}_{L+1,2} & \cdots & \dot{\mathbf{B}}_{L+1,P_W} \\ \vdots & \vdots & \ddots & \vdots \\ \dot{\mathbf{B}}_{L+W,1} & \dot{\mathbf{B}}_{L+W,2} & \cdots & \dot{\mathbf{B}}_{L+W,P_W} \end{bmatrix} \tag{2.29}$$

where P_W is the number of B-spline control points per window. Notice that this approach limits the amount of unknown parameters at each solution window to P_W despite the increasing trajectory length. This procedure is followed for successive solution windows until the desired trajectory length is reached, and B-spline control points are solved from (2.27). Finally, the length of the profile in the last window (see Figure 6.c) is selected slightly larger ($L+W'$) to ensure that full stop at the end of the tool paths safely ensured.

The above strategy is effective for solving the global convex optimization problem efficiently for longer toolpaths. However, since the optimization problem given by (2.27) is solved by gradient-based methods, computational effort still grows for longer toolpaths due to increased size of data points to evaluate the objective function. For instance, in order to solve the optimization problem given by (2.27), $\mathbf{W}_D$ is constructed for the entire trajectory length up to second window, which is $(2-\alpha)W$. For the following (third) window, this length increases to$(3-2\alpha)W$. Similarly, sizes of D, G, $x'(s_e)$, and $y'(s_e)$ also increase. Furthermore, at each successive optimization, number of B-spline matrices to reconstruct (2.27) grow ($\mathbf{B}^{(2)}$, $\mathbf{B}^{(3)}$). In order to limit the computational expense, an additional windowing approach, which emphasizes the most recent samples in the trajectory is implemented. The basic idea is presented in Figure 6.d. As shown, a Tukey (tapered cosine) window is used. This window is referred to as the forgetting window. The objective function is simply multiplied by the forgetting window in the vicinity of the current solution window [47] similar to short-time Fourier transform. The forgetting window (f) is given by:

$$f(\tau) = \begin{cases} \dfrac{1}{2}\left(1+\cos\left(\dfrac{2\pi}{r}(\tau-\dfrac{r}{2})\right)\right), & \tau < \dfrac{r}{2} \\ 1, & \tau \geq \dfrac{r}{2} \end{cases} \tag{2.30}$$

where$\tau \geq 0$ is the shifted time parameter, i.e., $\tau = t - t_{start}$, and t_{start} is the window start time. The window undergoes a transient from "0" to "1" for $r/2$ [sec], and it saturates at "1" for $\tau \geq r/2$. The width (F) of the Tukey window is selected slightly longer than the duration of the solution window ($L+W$) so that $L+W+(r/2)<F<U$ is satisfied, where U is the length of the complete trajectory. In practice, transient length ($r/2$) is selected as 25%–50% of the total forgetting window length (F).

With the introduction of the forgetting window, dimensions of $\mathbf{W}_D$ in (2.27) at the second solution window ($i=2$) are fixed at $2M \times F$ instead of $2M \times (2-\alpha)W$. For the following window ($i=3$), the size of $\mathbf{W}_D$ remains constant at $2M \times F$, as opposed to increasing to $2M \times (3-2\alpha)W$. Furthermore, sizes of $\mathbf{D}$, $\mathbf{G}$, $x'(s_e)$, and $y'(s_e)$ also remain constant for each successive window. This ensures that the computational cost of calculating the objective function gradient of (2.27) remains unchanged even though the trajectory length increases, which makes the developed trajectory generation method suitable for real-time implementation.

2.5. Experimental Validation

Experiments are conducted on an industrial three-axis CNC machine tool shown in Figure 7.a. Accelerometers in X-Y directions with 103 mV/m/s2sensitivity are attached on spindle head to measure residual vibrations when the Cartesian X- and Y-axes are moved. Frequency response functions in Figure 7.b show that the machine suffers from several lightly damped resonances and the spindle head is easily excited by the motion of the table in both X- and Y-directions.

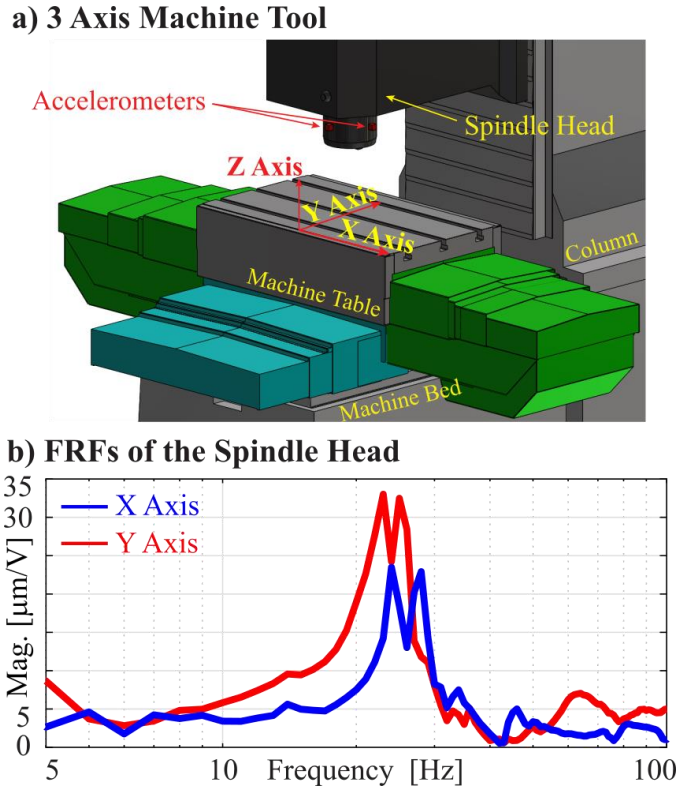

Figure 7. Illustration of the three-axis CNC machine tool used in experimental validation and the frequency response functions of its spindle head.

First set of experiments are performed along P2P linear trajectories. The min.-jerk [39] trajectory generation technique is used as a benchmark. A X-axis trajectory for 110 [mm] stroke is planned with 10 [m/sec^2] max acceleration to reach 400 [mm/s] cruise speed. Total acceleration transient lasts 0.075 [sec]. Based on this min.-jerk trajectory, proposed frequency optimal trajectory is generated with a frequency attenuation band of 25–60 [Hz]. The attenuation band is selected to robustly avoid all the low frequency modes shown in Figure 8.c. At first only frequency domain objective is minimized by solving the optimization problem given in (2.25). The control point resolution is set to 400 [points/sec]. Next, proposed optimal trajectory is generated by minimizing only the time domain objective through (2.25). The resonator model is selected with ω_n=28 [Hz] and ζ=0.03 to target the most critical mode. Finally, both frequency and time-domain objectives are minimized from (2.25). Convex optimization Toolbox, CVX [48] is used to solve the problem. Figure 8 summarizes time and frequency domain analysis of generated trajectories. As shown, basic min.-

jerk trajectory triggers large residual vibrations during acceleration/deceleration transients. Note that frequency spectrum of min.-jerk trajectory cannot be controlled. When only the frequency domain optimization is used, acceleration's frequency spectrum is well attenuated and residual vibrations are avoided; however, high frequency spectrum is amplified. When the proposed time and frequency optimal reference trajectory technique is applied, frequency spectrum of reference acceleration in the desired band is attenuated, and at the same time high frequency spectrum is also controlled to avoid exciting higher order modes. Note that cycle time is not altered from the template min.-jerk trajectory. Input-shaping strategy is also implemented on the min.-jerk trajectory by filtering it with 3 cascade IS with delays of 0.0179, 0.0143, and 0.0109 [sec] to cancel structural resonances at 28, 35, and 46 [Hz]. As seen, the IS provides frequency attenuation comparable to the proposed strategy. However, it adds 0.043 [sec] delay to the original acceleration profile. It elongates the cycle time and sacrifices from productivity. Overall, proposed technique avoids residual vibrations effectively while not elongating cycle time in linear P2P interpolation.

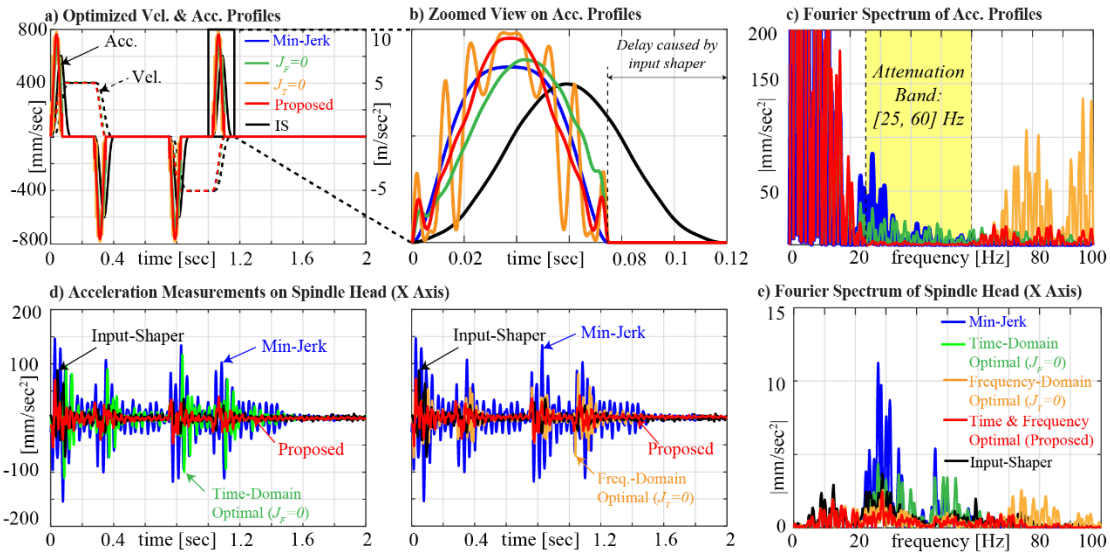

Figure 8. P2P linear interpolation trajectories.

Experimental validations are conducted also on the quintic spline toolpath shown in Figure 9.a. The toolpath consist of 220 waypoints (knots) with a total arc length of 975.9 [mm]. A constant feedrate (80 [mm/sec]) trajectory is generated based on min.-jerk acceleration transients and used as the template [s_e in (24)]. Reference kinematic

profiles are depicted in Figure 9.b. As shown, axis accelerations exceed 1 [g] due to varying path curvature. Proposed windowing approach is used, and the time/frequency optimal trajectory is generated. Parameters used in the optimization are identical as the ones used in the P2P interpolation case. Solution window length is set to be $L+W=332$ samples (0.332 [sec]). The overlap ratio α is chosen as 0.5 [see (26)]. This results in 73 solution windows, each of which is solved using a 1 [sec] long forgetting window with a resolution of 150 [points/sec]. This ensures that problem size remains unchanged as trajectory length grows. Note from Figure 9.b that the cycle time is kept unchanged from the template trajectory.

The machine is commanded with the template constant feed, proposed optimal trajectory and additionally constant feed trajectory filtered by identical ISs used in single-axis experiments (see Figure 8). Results are summarized in Figure 9. As shown, constant feedrate trajectory triggers large residual vibrations due to varying path curvature. Proposed trajectory generation technique provides robust vibration avoidance (see Figure 9.(c–h)). All of the target modes are within the cancellation band ([22, 55] [Hz]), and their vibrations are avoided. ISs also provides effective vibration avoidance. However, it clearly jeopardizes contouring performance and elongates the cycle time by 0.043 [sec] [see Figure 9.e]. Contouring errors are measured by the method given in [49]. IS increases max contour errors by$\sim$1.5×. In contrary, proposed method avoids residual vibrations and does not induce contouring errors. In fact, contouring performance is even improved by 60% since the time domain objective provides some feedforward action. Also, notice that the cycle time is unchanged from the template profile.

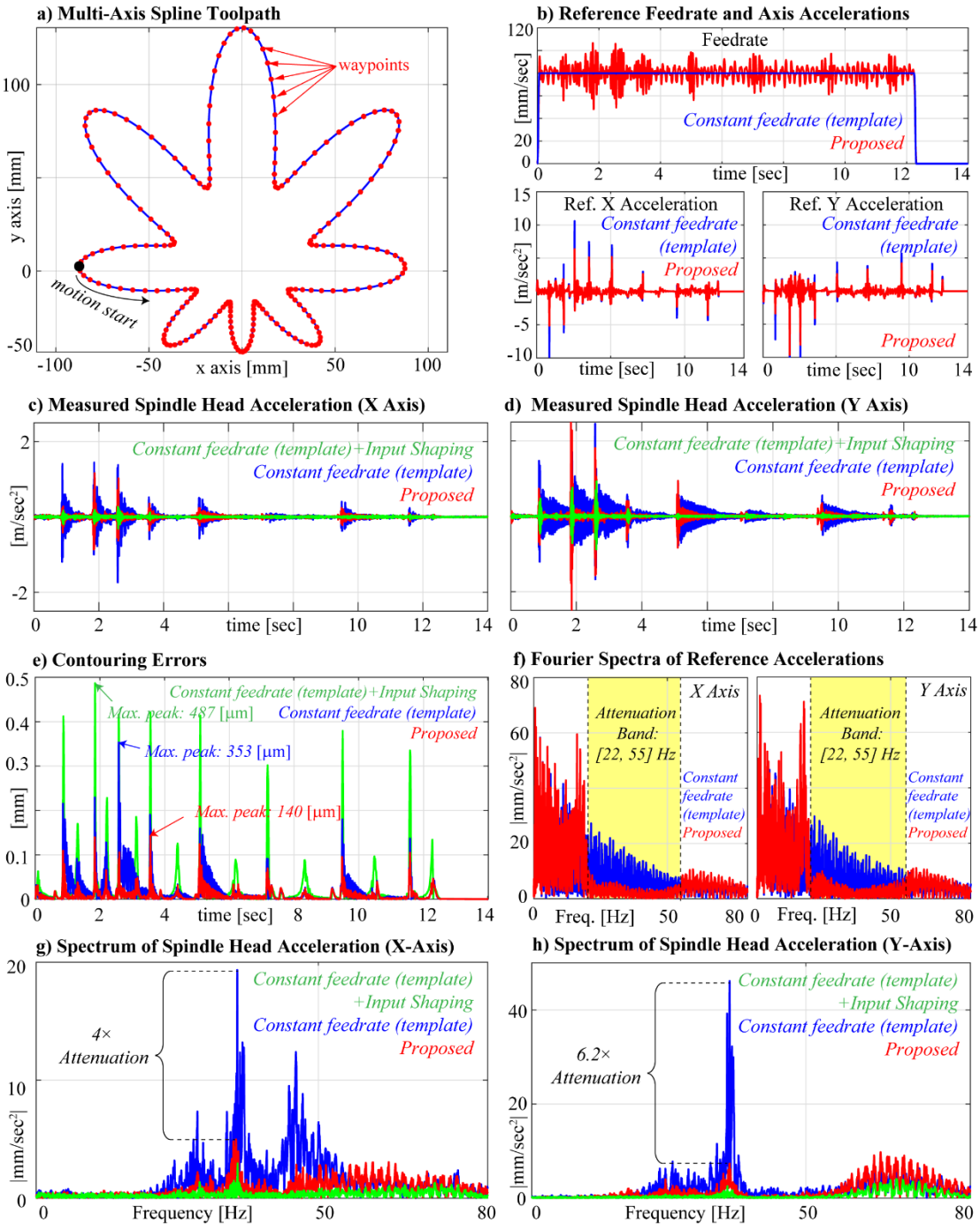

Figure 9. Experimental validation of the proposed method for a multiaxis trajectory.

2.6. Conclusions

This article presented a trajectory generation method with optimal frequency spectrum in order to robustly avoid excitation of lightly damped structural resonances of precision motion generation systems. The proposed method is formulated forbothP2Pmotiongenerationandcoordinatedmultiaxistrajectorygeneration. Proposed method is posed as a linear least squares minimization problem with convex equality and inequality constraints. The resulting problem is a convex optimization problem, and therefore can be efficiently solved to global optimality. A windowing-based solution method is proposed in order to efficiently implement the proposed method for industrial ap-plications. Proposed method is validated on an industrial-scale machine tool with multiple vibration-modes. The experimental results show that the proposed method provides superior vibration avoidance compared to min.-jerk trajectories. Additionally, it is demonstrated that the proposed method is able to deliver vibration avoidance and reduce contouring errors simultaneously, whereas IS-based trajectories deteriorates the contouring performance.

PRE-COMPENSATION OF SERVO TRACKING ERRORS THROUGH DATA-BASED REFERENCE TRAJECTORY MODIFICATION

Alper Dumanli and Burak Sencer

CIRP Annals – Manufacturing Technology
Volume 68, No. 1, May 2019, Pages 397-400

3. Pre-Compensation of Servo Tracking Errors through Data-Based Reference Trajectory Modification

This paper presents a new dynamic errors compensation approach with novel data-based tuning scheme to enhance tracking accuracy of machine tool feed-drives. Both plant's dynamic and friction disturbance induced positioning errors are compensated by modifying the reference trajectory. Velocity, acceleration, jerk and snap profiles of reference trajectory are modulated to achieve perfect tracking. Reference position profile is modified based on the pre-sliding regime to eliminate quadrant glitches. Optimal compensation parameters are identified iteratively by making on-the-fly adjustments to the reference trajectory through machine-in-the-loop type optimization. Effectiveness of proposed compensation approach is validated experimentally in multi-axis feed drive systems.

3.1. Introduction

Productivity and overall accuracy of machine tools depend on speed and accuracy of its feed drive systems [12]. Feed drives suffer from quasi-static volumetric and dynamic tracking errors. Volumetric errors can be measured and compensated through reference trajectory modification without interfering with servo controller [50]. Dynamic tracking errors occur constantly as servo controller tries to compensate for inertial and viscous damping forces, and struggles to overcome non-linear friction and process induced disturbances [51].

Machine tool literature focuses on two major strategies to mitigate dynamic feed-drive errors: (i) exhausting limits of feedback (FB) control through design of non-linear, robust adaptive [12], [51], [29], [52] controllers with modal damping [29], [6], and (ii) compensating rest of the dynamic errors through feedforward (FF) control, which is not only used to cancel known servo dynamics [51], [53] but also disturbances such as the non-linear friction [51], pitch error induced loads and harmonic cogging forces [12], [29]. If the dynamics to be compensated is represented accurately by casual, stable models; FF compensation is safe and effective [51], [53]. However, modelling stage is typically by-passed in practice, and FF compensator gains are hand-

tuned via trial-and-error. Drive dynamics vary with both position and workpiece inertia [12], [52]. Friction dynamics vary by time, and hence compensator re-tuning is necessary to regain lost dynamic accuracy, which is time consuming and costly.

Relying solely on FB and FF control is insufficient. Recently, benefits of reference trajectory generation are recognized as they are optimized to avoid residual vibrations [10] or pre-compensate for the servo lag to enhance machine's contouring performance [32]. Most NC systems provide digital trajectory pre-filters [50] and external trajectory command input functions to help end-users exploit limits of their machines, and also integrate with the industry 4.0 [54].

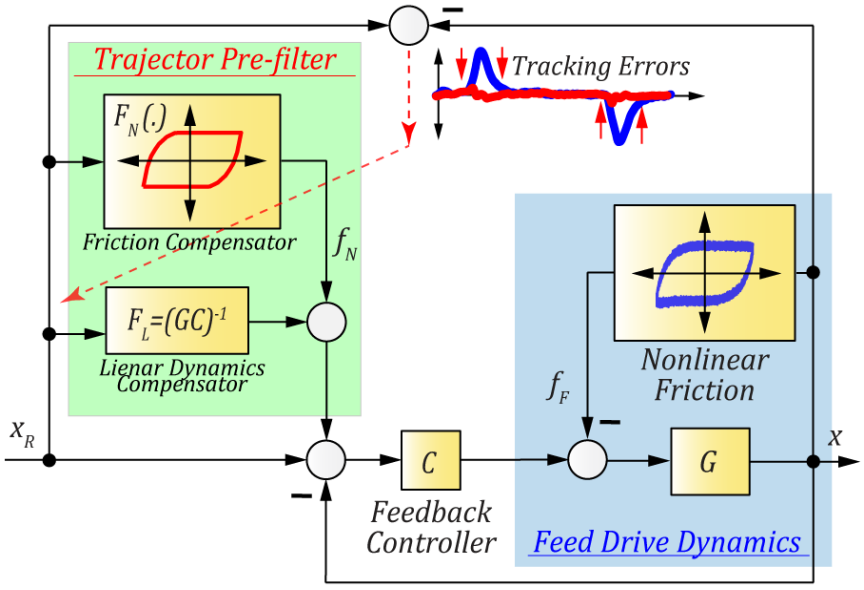

Figure 10. Proposed trajectory modification strategy.

This paper presents a novel strategy to pre-compensate dynamic feed drive errors through reference trajectory modification. Reference velocity and acceleration commands are modified to pre-compensate servo dynamics induced errors. Whereas, reference position profile is modified locally to cancel pre-sliding (stick/slip) friction induced positioning errors to achieve near-perfect tracking. 2 key contributions are presented to achieve this compensation scheme effectively. Firstly, the trajectory pre-compensation is realized by a fixed-structured digital pre-filter whose parameters are identified automatically via machine-in-the-loop learning, which is data-based and does not require any expert knowledge. Secondly, identification of trajectory pre-filter

is posed as a convex optimization problem, which provides rapid, save and reliable auto-tuning. The proposed approach is simple. It can improve dynamic accuracy of older or newer CNC machines either through offline or online trajectory modification and demonstrated experimentally on feed drives.

As shown in Figure 10 reference commands x_R are modified by two pre-compensation filters, F_N and F_L, and the modified trajectory $x_M=x_R+F_L(x_R)+F_N(x_R)$ is sent to the closed loop servo control system so that final axes position x perfectly follow x_R. The pre-compensation filter F_L is used to cancel feed drive's linear closed loop dynamics. $F_N(.)$, is designed to cancel the non-linear stick/slip friction induced errors by offsetting the trajectory during velocity reversals. The following sections describes pre-filter design and its auto-tuning using data-based optimization.

3.2. Pre-Compensation of Linear Servo Dynamics

Machine tool feed-drives are mostly controlled by cascade P-PI or PID controllers tuned carefully to avoid exciting structural resonances [12]. As a result, typical feed-drive tracking response is dominated by rigid-body plant $G(s)$ and FB controller $C(s)$ dynamics, which induces large servo errors during rapid acceleration and deceleration. If the original trajectory is modified by a pre-filter F_L (see Figure 10) whose transfer function in Laplace (s) domain is selected as:

$$F_L = \frac{1}{GC} = \frac{ms^3 + bs^2}{K_D s^2 + K_P s + K_I} \;\rightarrow\; \frac{x}{x_R} = \left(1 + F_L\right)\underbrace{\left(\frac{GC}{1+GC}\right)}_{G_{CL}} \simeq 1 \qquad (3.1)$$

closed loop servo dynamics $G_{CL}(s)$ can be compensated to achieve near-perfect tracking ($x \approx x_R$). Above pre-filter structure satisfies 2 key assumptions. Firstly, the numerator amplifies original acceleration and velocity profiles only by the uncompensated mass (m) and viscous friction (b) amount. Secondly, the denominator tries to compensate for the FB controller dynamics. Note that all linear servo controllers can be implemented by mapping their parameters into basic PID gains, K_P, K_D and K_I [29], [6]. Therefore, proposed pre-filter design can capture dynamics of most industrial servo systems.

Initial pre-filter parameters are identified automatically from a single closed-loop tracking experiment. The machine is instructed by a simple back-and-forth trajectory and the resulting error profile e_L is recorded. The error dynamics is governed by:

$$\frac{e_L}{x_R} = \frac{1}{1+GC} = \frac{ms^3 + bs^2}{ms^3 + \ K_D + b \ s^2 + K_P s + K_I}$$
$$e_L = x_R - \frac{1}{m}\left((K_D + b)\int_0^t e_L d\tau + K_P \int_0^t \int e_L d\tau + K_I \int_0^t \int \int e_L d\tau - b\int_0^t x_R d\tau \right) \tag{3.2}$$

Eq. (3.2) is sampled at servo loop period T_s and mass-normalized (m) pre-filter parameters are identified from least squares (LS) fitting:

$$\min_{\boldsymbol{\theta}} \frac{1}{2}\left\| \Phi\boldsymbol{\theta} - \boldsymbol{\gamma} \right\|_2^2 \quad \text{subject to: } \boldsymbol{\theta} \geq 0$$
$$\boldsymbol{\gamma} = \begin{bmatrix} x_R(0) - e_L(0) \\ x_R(T_s) - e_L(T_s) \\ \vdots \\ x_R(MT_s) - e_L(MT_s) \end{bmatrix}, \ \boldsymbol{\theta} = \begin{bmatrix} \theta_1 \\ \theta_2 \\ \theta_3 \\ \theta_4 \end{bmatrix} = \begin{bmatrix} K_D + b \\ K_P \\ K_I \\ b \end{bmatrix} \frac{1}{m} \tag{3.3}$$
$$\boldsymbol{\Phi} = \begin{bmatrix} e_i(0) & e_{ii}(0) & e_{iii}(0) & -x_{Ri}(0) \\ e_i(T_s) & e_{ii}(T_s) & e_{iii}(T_s) & -x_{Ri}(T_s) \\ \vdots & \vdots & \vdots & \vdots \\ e_i(MT_s) & e_{ii}(MT_s) & e_{iii}(MT_s) & -x_{Ri}(MT_s) \end{bmatrix}$$

where e_i, e_{ii}, e_{iii} are digitally integrated error e_L profiles in Eq. (3.2) over $0 \ldots M$ samples.

In practice, above transfer function fitting approach may not provide the most suitable compensator parameters. If the feed-drive suffers from strong non-linear guideway friction, identified rigid-body parameters could be biased [18], or even the pre-filtered trajectory may excite resonances [53]. To alleviate those practical problems following machine-in-the-loop fine-tuning approach is developed, and numerator of the pre-filter is updated.

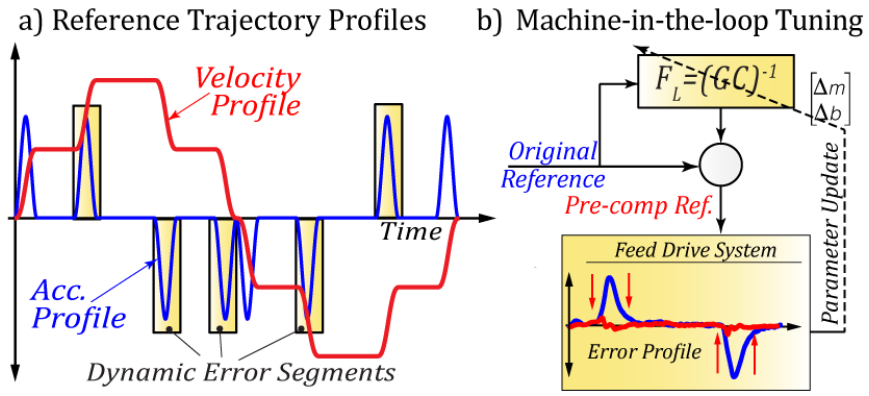

Figure 11. Machine-in-the-loop tuning of trajectory pre-filter F_L.

The machine is commanded by an NC code containing non-stop speed changes shown in Figure 11.a. Pre-filter parameters are updated to minimize the tracking errors around acceleration transients, which helps to eliminate non-linear friction bias and at the same time penalizes excitation of higher order error dynamics. This can be postulated by the following optimization problem:

$$\min_{m,\,b}\left(J_L = \frac{1}{2}\|\mathbf{e}_L\|_2^2 = \frac{1}{2}\mathbf{e}_L^T\mathbf{e}_L \right), \quad \text{subject to: } m \geq 0,\ b \geq 0 \tag{3.4}$$

where $\mathbf{e}_L$ is the tracking error vector. Based on Eq. (3.4) pre-filter parameters are adjusted; compensated trajectory is sent to the machine again, and resulting error trend is used to update the filter parameters for the next run as shown in Figure 11.b. Machine-in-the-loop iterations are continued until convergence is achieved.

This approach mimics manual trial-and-error tuning by an expert. Safe and reliable convergence is crucial. Automatic parameter update is achieved by solving Eq. (3.4). This is a convex optimization problem, and thus utilizing gradient (Jacobian) of its cost function $\nabla J_L=[\partial J_L/\partial m,\ \partial J_L/\partial m]^T=\mathbf{e}_L{}^T\nabla\mathbf{e}_L$, and the positive definite Hessian matrix $\nabla^2 J_L=\nabla\mathbf{e}_L{}^T\nabla\mathbf{e}_L$ enables us to rapidly and safely guide the search to global minimum. Notice that $\mathbf{e}_L$ is already available as a measurement data, and its gradient $\nabla\mathbf{e}_L$ can be obtained by filtering reference trajectory x_R or the original uncompensated response x from Eq. (3.1) as:

$$e_L = x_R - x = \left(\frac{1 - F_L GC}{1 + GC}\right) x_R \rightarrow \nabla e_L = \begin{bmatrix} \frac{\partial e_L}{\partial m} \\ \frac{\partial e_L}{\partial b} \end{bmatrix} = -\nabla F_L \underbrace{\left(\frac{GC}{1 + GC}\right) x_R}_{x} \tag{3.5}$$

$$\text{where: } \nabla F_L = \begin{bmatrix} s^3 \\ s^2 \end{bmatrix} \frac{1}{K_D s^2 + K_P s + K_I}$$

Filter parameters are updated by simply making use of Newton's second order iteration scheme:

$$\begin{bmatrix} m \\ b \end{bmatrix}^{k+1} = \begin{bmatrix} m \\ b \end{bmatrix}^{k} - \alpha \left(\nabla^2 J_L\right)^{-1} \left(\nabla J_L\right) \tag{3.6}$$

where α is the learning gain, and k is the iteration number. Notice that above iteration scheme is a discrete linear dynamic system. Range of learning gains for reliable convergence can be analyzed [8] and $1 > \alpha > 0$ provides reliable convergence. Inequality constraints are included using primal-dual interior point algorithm [55].

3.2.1. Experimental Validation

Proposed algorithm is tested on a cartesian micro-machine tool shown in Figure 12. *X* and *Y* axes are controlled by cascade P-PI controllers with hand-tuned FF compensators on the deltaTau NC system. Axes are moved by a single G-code back-and-forth at 50 and 100 [mm/sec]. Reference trajectory and error profiles are recorded at 1 [kHz]. As shown in Figure 12.c, tracking errors peak around acc/dcc sections of reference trajectory. Proposed trajectory prefiltering is applied by tuning (training) the prefilter F_L using Eqs. (3.3) and (3.6) on the same trajectory. As shown in Figure 12.b, best filter parameters are identified within 5-6 iterations with α=0.75, and tracking errors are reduced to less than +/-3[μm]. Remaining tracking errors are due to non-linear friction disturbance. They are eliminated by the reference trajectory pre-filtering technique presented in the following section.

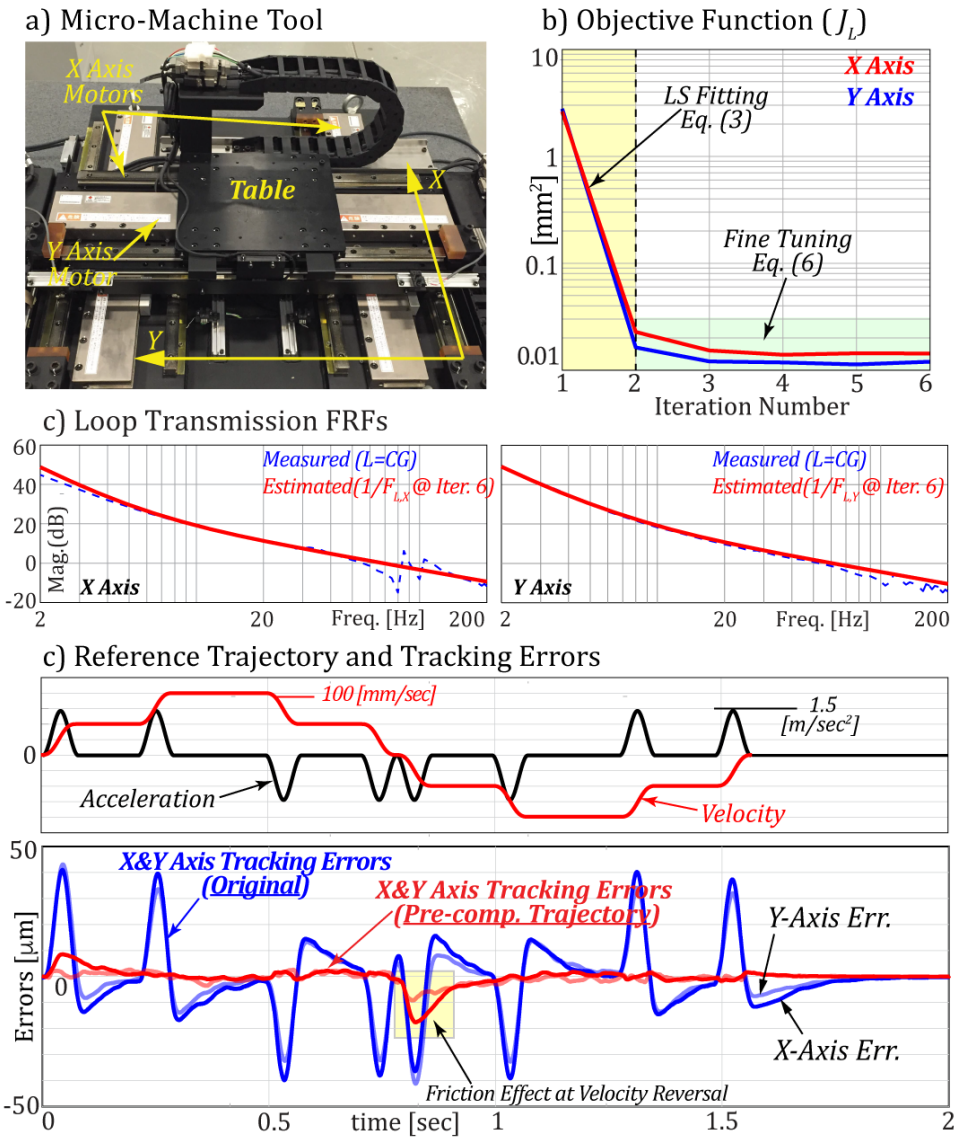

Figure 12. Experimental validation of servo dynamics compensation.

Once the trajectory pre-filter F_L is trained for the machine's feed drive dynamics, it can be applied to any trajectory for perfect tracking. This is demonstrated by eliminating contouring errors along a curved tool-path presented in the following section 3.3.1.

3.3. Pre-Compensation of Nonlinear Pre-Sliding Friction

Another major source of dynamic servo errors is the non-linear friction. As shown in previous section, industrial servo controllers cannot effectively reject rapidly

changing friction forces, which leaves quadrant glitches and surface location errors during velocity reversals [51], [29], [52], [53]. This section shows how reference trajectory can be modified to compensate for them.

Trajectory pre-filter F_L is used to cancel linear servo dynamics. Therefore, only friction induced errors are apparent at velocity reversals and can be predicted from closed-loop dynamics as:

$$e = f_F \underbrace{\left(\frac{G}{1+GC}\right)}_{D(s)} - x_F \underbrace{\left(\frac{GC}{1+GC}\right)}_{G_{CL}(s)} \rightarrow e = \left(\frac{f_F}{C} - x_F\right)\underbrace{\left(\frac{GC}{1+GC}\right)}_{G_{CL}(s)} \tag{3.7}$$

where x_F is the pre-compensation command generated by $F_N(.)$ (see Figure 10), $D(s)$ is the disturbance TF, and f_F is the nonlinear friction disturbance. Eq. (3.7) reveals an important fact: If the reference trajectory is offset by controller ($C(s)$) filtered friction forces $x_F = x_R + C^{-1} f_F$, it can cancel friction induced errors as well. This requires **(i)** knowledge of controller dynamics $C(s)$, which is already identified from LS fitting in Eq. (3.3), and **(ii)** an accurate estimation of friction forces. The following describes how nonlinear stick/slip friction could be identified automatically (adaptively) from closed-loop experiments and cancelled by the pre-compensation signal generated by trajectory prefilter, $F_N(.)$.

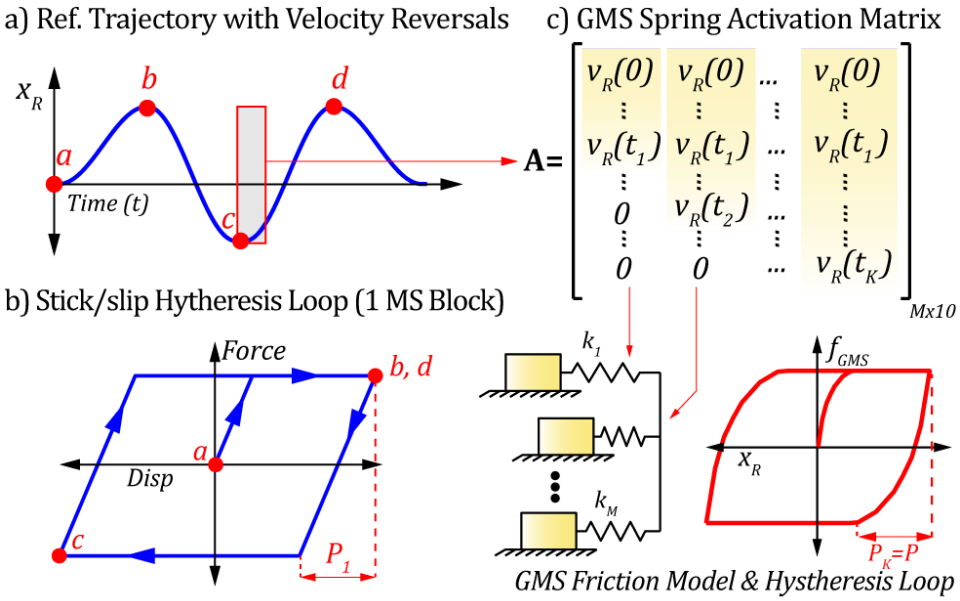

Figure 13. Modified GMS Model and the Spring Activation Matrix (**A**).

Generalized Maxwell-slip (GMS) model [51], [56] accurately captures hysteretic stick/slip induced pre-sliding friction dynamics with non-local memory. However, it must be tuned either manually [51], [56] or using non-linear optimization [57] to compensate or cancel friction disturbances. To facilitate automatic tuning, a modified GMS form is proposed here as:

$$f_{GMS}=\sum_{i=1}^{K}k_i z_i,\quad \frac{dz_i}{dt}=\begin{cases}\dot{x}_R=v_R, & \text{if stick } \left(i.e.\ z_i\le\left|P_i/2\right|\right)\\ 0, & \text{if slip } \left(i.e.\ z_i>\left|P_i/2\right|\right)\end{cases} \tag{3.8}$$

where K is the number of MS blocks that stick and slip (see Figure 13), and k_i is i^{th} block's spring coefficient while sticking. As blocks undergo local micro-translation (z_i), they slip only when they exceed their break-away (stick) distance, P_i. The fundamental difference of above modified GMS formulation (Eq. (3.8)) from the conventional one is that; here, the stick/slip conditions are governed by break-away distances rather than break-away forces [56]. Stick distance of feed-drives range 10~100[μm] [56], which can be observed from a simple tracking experiment. The stick distance is divided and distributed to individual MS block's stick distances as; $P_1<P_2<\ldots<P_K=P$. As a result, only unknowns in this modified GMS model are spring coefficients k_i that can be identified simply in the sense of linear least squares (LS). Furthermore, above GMS formulation preserves all the properties of original GMS including the non-local hysteresis memory [51], [56].

Eq. (3.8) can be put in a simple linear matrix-vector form as:

$$\frac{d}{dt}\mathbf{f}_{GMS}=\mathbf{A}\mathbf{k},\quad \text{where } \mathbf{A}=\begin{bmatrix}\dot{\mathbf{z}}_1 & \dot{\mathbf{z}}_2 & \cdots & \dot{\mathbf{z}}_K\end{bmatrix} \tag{3.9}$$

where, $\mathbf{k}=[k_1\ldots k_K]^T$ contains spring constants, and $\mathbf{A}$ is the *spring activation matrix*, which contains stick/slip velocities v_R for each individual block. Its structure is illustrated in Figure 13 for a sinusoidal trajectory. Each column of $\mathbf{A}$ represents individual MS block's stick/slip kinematics during velocity reversals. For instance, first MS block sticks during a velocity reversal ($t=0$) until $x_r=P_1$, which occurs at $t=t_1$. The next block sticks a little longer, until $x_R=P_2$, $t=t_2$. The $\mathbf{A}$ matrix is generated from reference trajectory, and it is "velocity reversal dependent". Combined with spring constants, it captures the friction induced hysteresis behavior shown in Figure 13.

Identification of GMS spring constants to compensate (minimize) friction errors is postulated by the following optimization problem:

$$\min_{\mathbf{k}}\left(J_N = \frac{1}{2}\|\mathbf{e}_v\|_2^2 = \frac{1}{2}\mathbf{e}_v^T\mathbf{e}_v \right), \quad \text{subject to: } \mathbf{k} \geq 0 \tag{3.10}$$

where $\mathbf{e}_v$ is the tracking error vector recorded around a velocity reversal. Similar to the previous section, Eq. (3.10) depicts an optimization problem with quadratic objective J_N, and it can be solved utilizing its gradient $\nabla J_N = [\partial J_N/\partial k_1 \ldots \partial J_N/\partial k_N]^T = \mathbf{e}_v^{\mathrm{T}}\nabla\mathbf{e}_v$ and Hessian $\nabla^2 J_N = \nabla\mathbf{e}_v^{\mathrm{T}}\nabla\mathbf{e}_v$. $\nabla\mathbf{e}_v$ that are available analytically by filtering measured tracking error data by plugging Eq. (3.9) into (3.7):

$$\begin{aligned} & e = \left(f_F - f_{GMS} \right)\frac{1}{C}\left(\frac{GC}{1+GC}\right) \rightarrow \nabla e = -\nabla f_{GMS}\,\frac{1}{C}\left(\frac{GC}{1+GC}\right) \\ & \text{where: } \nabla\mathbf{f}_{GMS} = \int_{t=0}^{MT_s} \mathbf{A}dt, \text{ and } \nabla = \left[\frac{\partial}{\partial k_1} \quad \cdots \quad \frac{\partial}{\partial k_K}\right]^T \end{aligned} \tag{3.11}$$

where ∇f_{GMS} is the friction pre-compensation signal, and $\nabla\mathbf{f}_{GMS}$ is its discretized vector containing M samples.

As shown, proposed formulation of GMS friction model (Eq. (3.8)) allows us to define friction induced error gradient explicitly as a function of the reference trajectory. Machine-in-the-loop iterations are used to safely train the friction pre-compensator parameters $F_N = f_{GMS}/C$ using Newton iterations:

$$\mathbf{k}^{k+1} = \mathbf{k}^k - \alpha\left(\nabla^2 J_N\right)^{-1}\left(\nabla J_N\right) \tag{3.12}$$

3.3.1. Experimental Validation

Effectiveness of the proposed trajectory pre-filtering scheme for friction compensation is tested on the same linear motor driven micro-machine tool (see Figure 12.a). A spiral curved tool-path shown in Figure 14.a is commanded at a feed of 50[mm/sec]. The linear F_L filter (tuned previously) is used to compensate for servo dynamics. As a result, large quadrant glitches occur around velocity reversals due to *X-Y* drive's friction disturbances, and they are visible in the contour error trend in Figure 14.c. Friction compensator pre-filter F_N is trained using Eq. (3.12) at each velocity reversal (iteration) *on-the-fly* to offset the trajectory and cancel friction. 10 GMS blocks

are used to capture the pre-sliding friction regime of the feed-drive. As shown in Figure 14, after the 15^{th} velocity crossing, stick/slip hysteresis curve is automatically identified, and reference trajectory is modified to perfectly cancel quadrant glitches as shown in Figure 14.a and c. Contour errors are reduced down to 1[μm]. By combining both linear servo dynamics and the friction pre-compensator filters, near-perfect tracking could be achieved. Once trained, the trajectory compensation filters can be used at any trajectory to enhance the contouring performance.

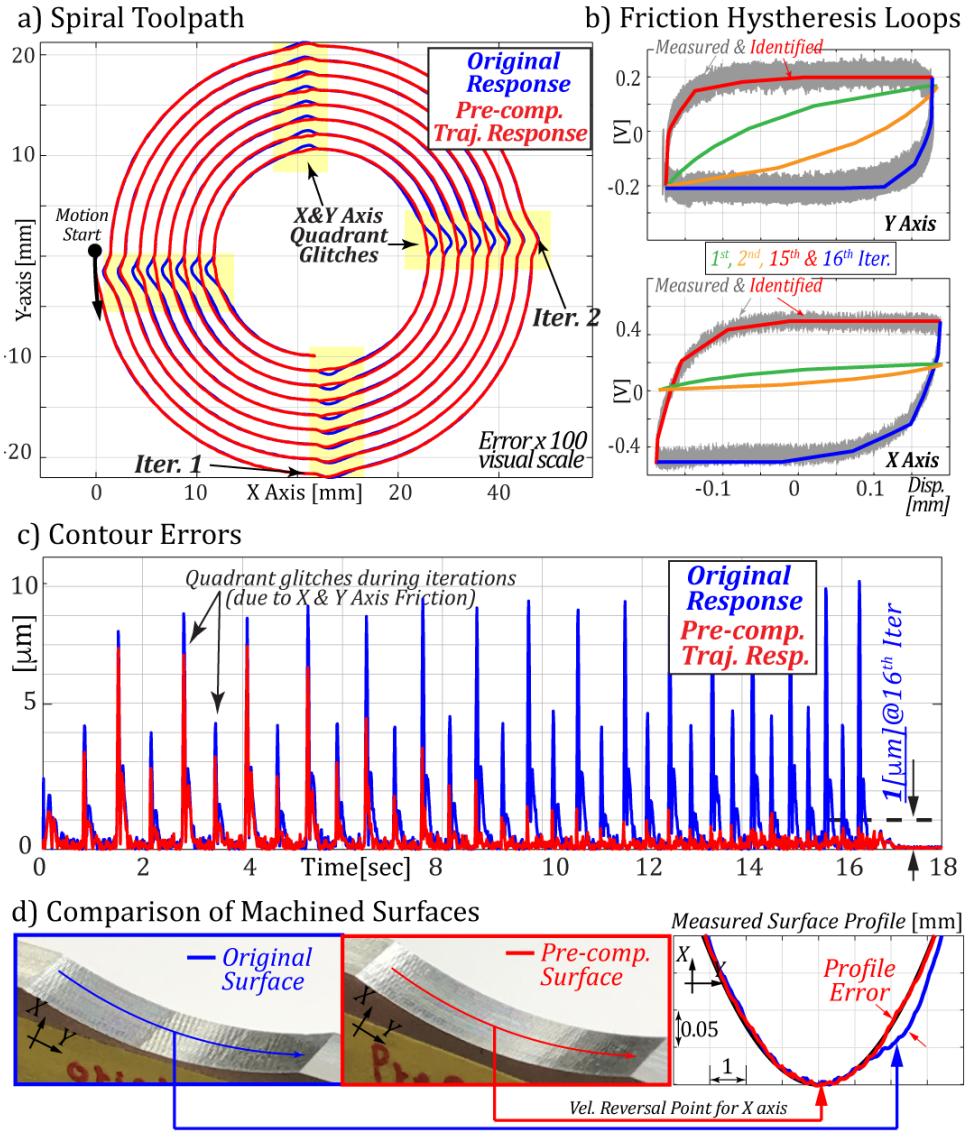

Figure 14. Experimental compensation of Stick/Slip friction.

Finally, micro milling experiments are conducted to showcase the importance of stick/slip pre-sliding fiction compensation in surface finish quality in Figure 14.d. A concave surface is cut on A5052 workpiece at 5[mm] depth and 0.1[mm] radial immersion with 15[krpm] spindle speed and 0.02[mm/rev-tooth] feed. *X-axis* reverses its motion direction at the bottom of surface. At that instant pre-sliding friction starts kicking in and causes surface profile errors over ~20[μm] (Figure 14.d, measured by Surfcom Flex-50A). Notice that profile errors occur slightly delayed from velocity reversal point due to friction breakaway distance. Proposed pre-compensated trajectory cancels friction errors and thereby enables machining of near-ideal surface profile.

3.4. Conclusions

A novel error pre-compensation scheme is proposed, which greatly improves dynamic accuracy of machine tools by compensating for the closed-loop servo and stick/slip (pre-sliding) friction induced errors by modifying reference trajectory. Proposed scheme does not need prior knowledge of feed-drive dynamics nor it requires complicated open-loop identification experiments. It is implemented by a digital pre-filter whose parameters are tuned automatically from simply moving the axes back-and-forth by standard G-code, or even on-the-fly as machine travels along a known tool-path. It requires no expertise. Safe and reliable auto-tuning is achieved by formulating the tuning problem based on iterative learning and convex optimization. Overall, proposed technique can improve dynamic accuracy of newer or older machines equipped with a modern NC system.

3.5. Acknowledgement

Authors gratefully thank Prof. Kakinuma and Mr. Yamato from Keio University in Japan for their support and assistance, and NSF (Award No: 1661926) for partially funding this research.

DATA-DRIVEN ITERATIVE TRAJECTORY SHAPING FOR PRECISION CONTROL OF FLEXIBLE FEED DRIVES

Alper Dumanli and Burak Sencer

IEEE/ASME Transactions on Mechatronics
Published in December 2020, Early Access Available Online

4. Data-Driven Iterative Trajectory Shaping for Precision Control of Flexible Feed Drives

With recent advances on material processing technologies, design requirements on modern manufacturing equipment are shifting towards achieving higher speed and accuracy rather than stiffness and load capacity. Motion systems used in additive or ultra-precision manufacturing equipment need to be designed to achieve greater dynamic positioning accuracy. As a result, Feed-forward (FF) control becomes an effective tool. This paper presents a novel and practical FF controller design methodology to widen tracking bandwidth of precision motion systems suffering from structural dynamics and friction induced disturbances. The proposed feedforward controller is designed to (1) compensate for the closed-loop servo dynamics to widen the command tracking bandwidth, (2) mitigate unwanted vibrations and (3) compensate friction disturbance induced positioning errors. The FF controller is structured in a trajectory pre-filter form where the FF compensation signal is injected into the reference trajectory rather than torque command. This facilitates the FF controller to be applied conveniently without intervention with the servo controller. FF controller parameters are identified (tuned) automatically through machine in-the-loop-iterations. Parameter identification is posed as a convex optimization problem to realize safe and reliable auto-tuning. Proposed FF controller and its parameter tuning methodology are tested experimentally on an industrial scale multi-axis machine tool and its performance is validated.

4.1. Introduction

Accuracy and productivity of modern manufacturing equipment, such as machine tools [5], 3D-printers [2], industrial robots and ultra-precision systems [4] are largely influenced by dynamic positioning accuracy of their motion delivery (feed drive) systems. The ultimate goal is to widen the command tracking bandwidth, which is typically limited by the drive's structural dynamics and disturbance loads. This paper presents a novel trajectory pre-filter design and its practical auto tuning method to widen tracking bandwidth of flexible feed drives and overcome friction induced

disturbances.

Disturbances greatly limit dynamic accuracy of motion systems, and they can be categorized as internal or external. External disturbances originate from the (manufacturing) process. For CNC machines, external disturbances are due to cutting forces between tool and workpiece, and their frequency spectra is dictated by the rotational speed of the tool/workpiece [16]. High-gain feedback (FB) control design is needed to reject those process induced disturbances. FB control strategies based on loop shaping [1], pole placement [5][6], and H_∞ synthesis [26], or nonlinear techniques such as Sliding Mode Control [13] are employed to improve dynamic stiffness of motion system.

Modern positioning systems used in advanced manufacturing equipment, on the other hand, don't necessarily suffer from external disturbances. Instead, friction forces are more significant. Friction induced disturbances are wideband and inherent (internal) to the mechanical design. Unless these disturbances are tackled through hardware-based solutions such as frictionless bearings and guides [58], or hybrid drives [59]; their effect needs to be rejected through feedforward (FF) compensation [51]. Due to the complex pre-rolling/pre-sliding (stick/slip) friction regimes of disturbance forces, they exhibit nonlinear dynamics with position and velocity. Dahl, LuGre [60] and Generalized Maxwell Slip (GMS) [61] models are proposed to capture hysteretic displacement/friction force characteristics. Accurate parameter identification and adaptation are critical for successful FF compensation. Friction forces are sensitive to operating conditions including environmental temperature [57]. Frequency [56] and time domain-based parameter [17] identification methods are available. However, these methods are cumbersome to apply and not frequently used in practice. Built on the original GMS architecture, this paper proposes a modified GMS formulation to apply linear parameter regression to accurately and conveniently tune friction FF compensators for precision positioning.

Unwanted vibrations are another major source of errors affecting dynamic accuracy of precision motion platforms. They originate from the structural dynamics, e.g. lightly damped resonances of the feed-drive system and mostly triggered by inertial forces generated during high speed/acceleration motion [6], [10]. Therefore, they are referred

to as “trajectory induced (residual) vibrations” and most successfully mitigated by feedforward compensation. Input shaping (IS) [20], notch filtering [5], moving average (FIR) filtering [62], or frequency shaped trajectory generation [10] are used to control the spectral energy of reference motion commands and thereby mitigate trajectory induced unwanted vibrations.

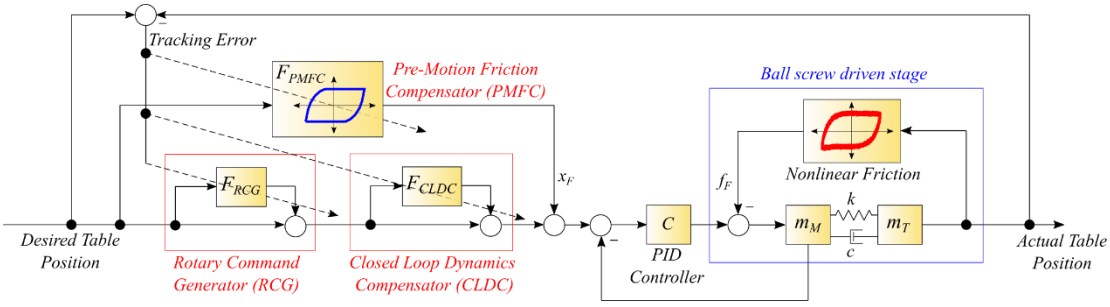

Figure 15. Overall block diagram of the proposed reference trajectory modification strategy.

Input shaping, when robustified [63], is effective in mitigating residual vibrations; however, robust shapers add extra delay to the system and elongate cycle times [10]. They can avoid excitation of resonances and improve point-to-point positioning accuracy. But, they distort original reference trajectory and degrade contouring accuracy in multi-axis applications [31]. Therefore, ISs are applied only to point-to-point (P2P) positioning. Inverse dynamic filtering (plant inversion) based on Zero Phase Error Tracking (ZPET) [64] or Perfect Tracking pre-filters (PTP) [5] are used to pre-filter reference trajectories to both avoid vibrations and improve tracking accuracy at the same time. These filtering techniques are effective in widening the tracking bandwidth of most motion systems. Nevertheless, they rely on dynamics inversion and thus require precise identification of system dynamics.

Plant-inversion based pre-filters and FF controllers can also be designed by making use of Iterative-Learning-Control (ILC) framework, where filter parameters are optimized through Machine-In-the-Loop (MIL) iterations [65]. Simple Finite-Impulse-Response (FIR) pre-filters can be easily tuned using data-driven ILC methods [8]. However, compensating flexible dynamics of feed drive systems with Infinite-Impulse-Response (IIR) pre-filters promises much better performance [4]. Iteratively tuning IIR

coefficients requires solving a nonconvex optimization problem that does not guarantee convergence to global optimum [66]. Furthermore, executing such optimization schemes in a MIL fashion may jeopardize equipment safety and largely avoided in practice.

This paper proposes a novel multi-step trajectory pre-filtering technique, which suppresses trajectory induced vibrations in flexible feed drive systems, widens tracking bandwidth and also rejects friction induced disturbances to attain greater positioning accuracy. The pre-filter pack is tuned automatically through use of *convex* MIL iterations so that lengthy identification and testing procedures are eliminated. Figure 15 shows the proposed pre-filtering scheme, which consists of the following 3 key components:

i) A Closed Loop Dynamic Compensator (CLDC) is designed to invert collocated closed-loop dynamics and widen the tracking bandwidth.

ii) Next, a Rotary Command Generator (RCG) is designed to mitigate excitation of lightly damped structural vibrations modes (resonances).

iii) Lastly, a Pre-Motion Friction Compensator (PMFC) is designed to directly offset the reference trajectory, so that friction induced tracking errors are eliminated.

Through design of these trajectory pre-filters, this paper presents the following contributions:

C1) Instead of relying on single-shot plant inversion, a systematic multi-stage trajectory pre-filter design approach is put forward, where each pre-filter targets a specific error source inherent to flexible feed drives.

C2) Filter parameters are tuned through data-driven (MIL) *convex* optimization, which provides numerical efficiency and guarantees global optimality.

C3) A linear Generalized Maxwell Slip (GMS) friction model formulation is presented, which allows convex parameter tuning through MIL iterations.

The paper is outlined as follows. Section 4.2 presents control oriented modeling of flexible ball-screw drives widely used in modern feed drive systems. Sections 4.3, 4.4 and 4.5 introduce design, auto-tuning and experimental validation of the proposed RCG, CLDC and PMFC pre-filters in sequences.

4.2. Dynamics of Ball-Screw Drives

Most industrial feed-drive systems are driven by ball-screw (BS) transmission mechanisms. A typical BS driven feed-drive, and its physical lumped-mass model are illustrated in Figure 16.a and b. A rotary motor drives a ball-screw to realize linear motion of the table. Due to their transmission components, most BS feed-drives are flexible, and their attainable positioning accuracy (bandwidth) is limited by structural vibrations [6]. Figure 16.c shows frequency response function (FRF) of a flexible BS drive. The 1st resonance at (ω_n) generally originates due to the flexibilities in the bearing system [5]. When excited, it induces relative motion between motor and table as shown in Figure 16.d. Control oriented flexible BS models [6] are based on a lumped mass model as shown in Figure 16.b, where m_M and m_T denote motor and table inertias, whereas k and c are spring and viscous damping coefficients. b_M and b_T depict viscous friction originating from guideways and bearing systems.

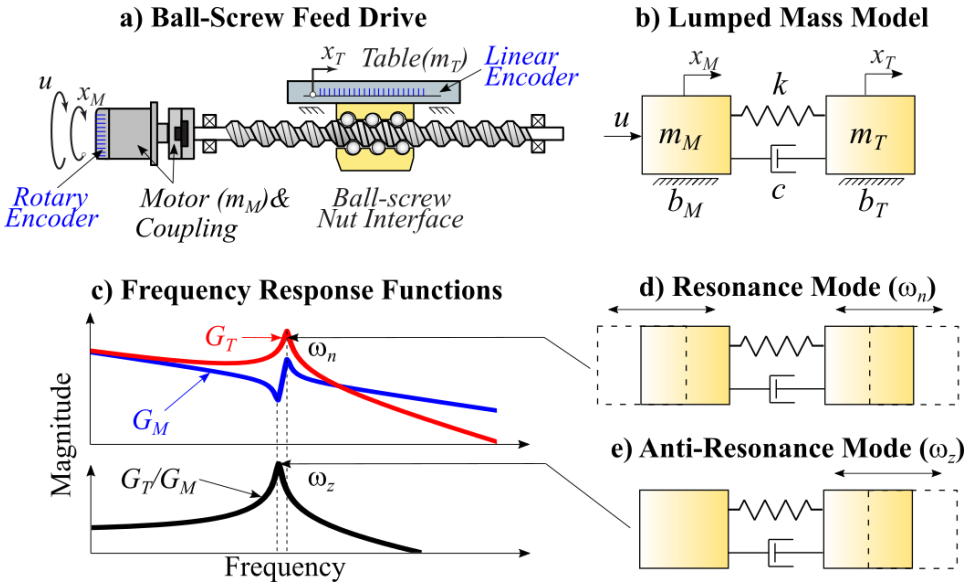

Figure 16. 2DOF ball-screw driven feed drive system dynamics.

Equation of motion for a flexible BS drive can be written as:

$$\begin{aligned} m_M \ddot{x}_M &= u - b_M \dot{x}_M - c\left(\dot{x}_M - \dot{x}_T\right) - k\left(x_M - x_T\right) \\ m_T \ddot{x}_T &= -b_T \dot{x}_T - c\left(\dot{x}_T - \dot{x}_M\right) - k\left(x_T - x_M\right) \end{aligned} \tag{4.1}$$

where x_M and x_T are the motor and table displacements. u is the control signal. Equation (4.1) can be written in Laplace (s) domain as:

$$\begin{aligned} G_M &= \frac{X_M}{U} = \frac{m_T s^2 + (c + b_T)s + k}{P},\ G_T = \frac{X_T}{U} = \frac{cs + k}{P} \\ P &= m_M m_T s^4 + (m_M b_T + m_T b_M + (m_M + m_T)c)s^3 \cdots \\ &\quad + (b_M b_T + (b_M + b_T)c + (m_M + m_T)k)s^2 + (b_M + b_T)ks \end{aligned} \tag{4.2}$$

where G_M and G_T are the motor and table side transfer functions (TF). In non-collocated control, FB measurements are taken from the table side (G_T), and only the resonance vibration mode is observed at $\omega_n = \sqrt{k(m_M + m_T)/(m_M m_T)}$ as illustrated in Figure 16.d. On the other hand, in collocated FB control strategy, rotary encoder feedback is used, and based on G_M, an anti-resonance at $\omega_z = \sqrt{k/m_T}$ appears exhibiting another relative vibration mode shown in Figure 16.e.

Understanding these vibration modes is critical in designing the feedforward pre-filter to widen the positioning bandwidth. In practice, most industrial servo control systems rely on *collocated* control schemes [1] to attain larger stability margins. This strategy ensures that motor follows reference position command precisely, and it assumes that the table follows the motor accurately. The ultimate goal is always to position the table rather than the motor. Nevertheless, both anti-resonance and resonance vibration modes can induce relative motion between motor and the table, and thus degrade the positioning accuracy of the table. The objective of the proposed pre-filtering strategy presented in following sections II and III is to pre-compensate table positioning errors during *collocated* motion control so that the table is positioned accurately.

4.3. Design of the Closed Loop Dynamics Compensator (CLDC)

This section presents design of the Closed Loop Dynamics Compensator (CLDC) pre-filter, $F_{CLDC.}$ The objective of F_{CLDC} is to widen the tracking bandwidth in collocated control of flexible BS systems. CLDC is designed to compensate for the slow dynamics of the controller and the resonance vibration mode shown in Figure 16.d. Structure of the CLDC is shown in Figure 15. As shown, reference motor position

command (trajectory) x_R is filtered by the F_{CLDC} and injected back into the reference position signal. Compensated reference command becomes $(1+F_{CLDC})x_R$, and by selecting F_{CLDC} as inverse of loop transmission $L^{-1}=(G_MC)^{-1}$, near-perfect collocated (motor-side) tracking can be achieved by:

$$F_{CLDC}=\frac{1}{G_MC}\rightarrow\frac{x_{M,C}}{x_R}=\left(1+F_{CLDC}\right)\underbrace{\frac{G_MC}{1+G_MC}}_{T_M}\cong 1 \tag{4.3}$$

where $x_{M,C}$ denotes the CLDC compensated motor position. C is the FB controller, and $T_M=L/(1+L)$ depicts the uncompensated motor-side closed-loop tracking TF.

The objective is to estimate the unknown loop transmission dynamics L without prior knowledge by simple time-domain motion tests from closed-loop tracking response, T_M. In order to estimate T_M, reference-acceleration to motor-error TF (E_A) is used:

$$\begin{aligned}E_A&=\frac{e_M}{a_R}=\frac{1}{s^2}\left(1-T_M\right)=\frac{c_4s^3+c_3s^2+c_2s+c_1}{s^5+\alpha_1s^4+\alpha_2s^3+\alpha_3s^2+\alpha_4s+\alpha_5}\\&=\frac{Ps}{Ps^3+s^2\left(K_Ds^2+K_Ps+K_I\right)\left(m_Ts^2+\left(c+b_T\right)s+k\right)}\end{aligned} \tag{4.4}$$

where a_R is the reference acceleration command, and e_M is the motor-side tracking error, i.e. $e_M=x_R-x_M$. P is the open-loop denominator already given in (4.2). Notice that acceleration error TF E_A is used instead of position tracking (e_M/x_R) dynamics. Doing so amplifies contribution of high frequency dynamics and thereby increases accuracy and robustness of parameter identification. Parameters of E_A are to be identified from a simple command tracking test by moving the motion system (axis) back-and-forth along a motion trajectory. Tracking error and reference acceleration signals are sampled at T_s period during the tracking experiment and stacked in matrix form:

$$\mathbf{U}=\begin{bmatrix} a_R(0) & a_R(T_s) & \cdots & a_R\big((j-1)T_s\big) \\ a_R(T_s) & a_R(2T_s) & \cdots & a_R(jT_s) \\ \vdots & \vdots & \ddots & \vdots \\ a_R\big((i-1)T_s\big) & a_R(iT_s) & \cdots & a_R\big((i+j-2)T_s\big) \end{bmatrix}$$
$$\mathbf{E}=\begin{bmatrix} e(0) & e(T_s) & \cdots & e\big((j-1)T_s\big) \\ e(T_s) & e(2T_s) & \cdots & e(jT_s) \\ \vdots & \vdots & \ddots & \vdots \\ e\big((i-1)T_s\big) & e(iT_s) & \cdots & e\big((i+j-2)T_s\big) \end{bmatrix} \quad (4.5)$$

where i is the number of rows and j is the number of columns in **U** and **E** matrices such that; $\mathbf{U}=\mathbf{U}_{i\times j}$ and $\mathbf{E}=\mathbf{E}_{i\times j}$. i and j are selected by following the guidelines given in [67], such that a_R is persistently exciting of order $2i$, and j is significantly larger than i, i.e. $j>>i$. E_A in (4.4) is written in the extended state-space form as:

$$\mathbf{E}=\boldsymbol{\Gamma}\mathbf{X}+\boldsymbol{\Pi}\mathbf{U}+\mathbf{N},\ \ \mathbf{X}=\begin{bmatrix}\mathbf{x}(0) & \mathbf{x}(T_s) & \cdots & \mathbf{x}\big((j-1)T_s\big)\end{bmatrix} \quad (4.6)$$

where $\mathbf{x}_{5\times 1}$ is the vector of system states, and **N** is the noise data matrix with the same structure as **E** and **U** given by (4.6). $\boldsymbol{\Gamma}$ is the extended observability matrix, and $\boldsymbol{\Pi}$ is the input Toeplitz matrix defined as:

$$\boldsymbol{\Gamma}=\begin{bmatrix}\mathbf{C}\\ \mathbf{CA}\\ \vdots\\ \mathbf{CA}^{j-1}\end{bmatrix},\ \ \boldsymbol{\Pi}=\begin{bmatrix}0 & 0 & \cdots & 0\\ \mathbf{CB} & 0 & \cdots & 0\\ \vdots & \vdots & \ddots & \vdots\\ \mathbf{CA}^{j-2}\mathbf{B} & \mathbf{CA}^{j-3}\mathbf{B} & \cdots & 0\end{bmatrix} \quad (4.7)$$

$\mathbf{A}_{5\times 5}$ is the state transition matrix, $\mathbf{B}_{5\times 1}$ and $\mathbf{C}_{1\times 5}$ are input and output matrices of the discrete-time state space representation of (4.4).

The goal is to identify the state transition matrix **A**, which yields parameter estimation for E_A (see (4.4)). To achieve this, $\boldsymbol{\Gamma}$ is identified by adopting the Multi-variable Output-Error State Space (MOESP) method [67]. Once $\boldsymbol{\Gamma}$ is obtained, it is used to obtain a stable estimation of the state transition matrix **A** as outlined in the following paragraphs.

Firstly, shift invariance property of the extended observability matrix ($\boldsymbol{\Gamma}$) is utilized, and $\boldsymbol{\Gamma}$ is partitioned into two overlapping sections from (4.7) as:

$$\boldsymbol{\Gamma}_1 = \begin{bmatrix} \mathbf{C} \\ \mathbf{CA} \\ \vdots \\ \mathbf{CA}^{j-2} \end{bmatrix}, \boldsymbol{\Gamma}_2 = \begin{bmatrix} \mathbf{CA} \\ \mathbf{CA}^{2} \\ \vdots \\ \mathbf{CA}^{j-1} \end{bmatrix}, \text{ where: } \boldsymbol{\Gamma}_1\mathbf{A} = \boldsymbol{\Gamma}_2 \tag{4.8}$$

Equation (4.8) implies that the *ideal* **A** matrix satisfies: $\boldsymbol{\Gamma}_1\mathbf{A}=\boldsymbol{\Gamma}_2$, and thus, it is used to postulate the following optimization problem in order to extract **A** matrix as:

$$\min_{\mathbf{A},\,\mathbf{P}} \left\| \boldsymbol{\Gamma}_1\mathbf{A} - \boldsymbol{\Gamma}_2 \right\|_F^2, \text{ subject to: } \begin{cases} \mathbf{A}^T\mathbf{P}\mathbf{A} - \mathbf{P} \prec \mathbf{0} \\ \mathbf{P} = \mathbf{P}^T \succ \mathbf{0} \end{cases} \tag{4.9}$$

where $\|.\|_F$ denotes the Frobenius norm [68]. Linear matrix inequality (LMI) constraints of (4.9) guarantee that **A** is stable according to Lyapunov's stability criterion [68], with **P** being the Lyapunov matrix. Notice that, (4.9) poses a non-convex optimization problem, which typically suffers from numerical inefficiency, inaccuracy and local minima. Hence, the problem in (4.9) is converted into a convex optimization problem.

The inequality constraints in (4.9) are rewritten using their equivalent Schur complement [55]:

$$\left.\begin{matrix} \mathbf{A}^T\mathbf{P}\mathbf{A} - \mathbf{P} \prec \mathbf{0} \\ \mathbf{P} = \mathbf{P}^T \succ \mathbf{0} \end{matrix}\right\} \Leftrightarrow \begin{bmatrix} \mathbf{P}^{-1} & \mathbf{A}\mathbf{P}^{-1} \\ \mathbf{P}^{-1}\mathbf{A}^T & \mathbf{P}^{-1} \end{bmatrix} \succ \mathbf{0} \tag{4.10}$$

Next, nonlinearities in (4.10) are circumvented by defining the new variables $\mathbf{R}=\mathbf{A}\mathbf{P}^{-1}$ and $\mathbf{Q}=\mathbf{P}^{-1}$, and Eq. (4.9) could be rewritten as a convex optimization problem as:

$$\min_{\mathbf{R},\,\mathbf{Q}} \left\| \Gamma_1\mathbf{R} - \Gamma_2\mathbf{Q} \right\|_F^2, \text{ subject to: } \begin{bmatrix} \mathbf{Q} & \mathbf{R} \\ \mathbf{R}^T & \mathbf{Q} \end{bmatrix} \succ \mathbf{0} \tag{4.11}$$

Equation (4.11) poses a convex semi-definite program [55], and it can be solved efficiently to global optimality. Its solution provides **R** and **Q** where **A** is easily recovered from $\mathbf{A}=\mathbf{R}\mathbf{Q}^{-1}$.

Eigenvalues of **A** are the poles of E_A - poles of the closed-loop servo dynamics T_M. Note that **A** is the *discrete-time* state transition matrix, whereas the desired acceleration error dynamics model E_A is written in continuous time (see (4.4)). Thus, **A** is converted to its continuous counterpart $\mathbf{A}_C$ in controllable canonical form as:

$$\mathbf{A}_C = \begin{bmatrix} 0 & 1 & 0 & 0 & 0 \\ 0 & 0 & 1 & 0 & 0 \\ 0 & 0 & 0 & 1 & 0 \\ 0 & 0 & 0 & 0 & 1 \\ -\alpha_5 & -\alpha_4 & -\alpha_3 & -\alpha_2 & -\alpha_1 \end{bmatrix} \tag{4.12}$$

with $\alpha_1 \ldots \alpha_5$ are defined as:

$$\begin{aligned} &s^5 + \alpha_1 s^4 + \cdots + \alpha_5 = (s - p_1)(s - p_2)\cdots(s - p_5) \\ &p_k = \ln\left(\text{eig}_k(\mathbf{A})\right)/T_s \end{aligned} \tag{4.13}$$

Utilizing the $\mathbf{A}_C$ matrix, E_A can be written in continuous state-space form as:

$$\dot{\mathbf{x}}_C = \mathbf{A}_C \mathbf{x}_C + \mathbf{B}_C \mathbf{a}_R,\ e = \mathbf{C}_C \mathbf{x}_C,\ \text{where: } \mathbf{x}_C = \left[x_C\ \dot{x}_C\ \ddot{x}_C\ \dddot{x}_C\ \ddddot{x}_C\right]^T \tag{4.14}$$

where $\mathbf{x}_C$ is the vector of continuous states. e and a_R are the tracking error and reference acceleration given by (4.4). Structure of the continuous input matrix $\mathbf{B}_C$ is selected as: $[0,0,0,0,1]^T$ so that all the zeros of E_A are captured by the continuous output matrix $\mathbf{C}_C$=[c_1,c_2,c_3,c_4,c_5]. This allows us to identify zeros of E_A conveniently. To identify $\mathbf{C}_C$, (4.14)is used to calculate $\mathbf{x}_C$, and the following optimization problem is formed:

$$\min_{\mathbf{C}_C} \left\| e - \mathbf{C}_C \mathbf{x}_C \right\|_\infty \text{ subject to: } c_5 = 0 \tag{4.15}$$

Equality constraint c_5=0 is imposed to satisfy the structure of E_A given in (4.4). Equation (4.15) is an infinity norm minimization problem, and it can easily be implemented as a linear program with linear inequality constraints and solved to its global optimum [55]. Finally, E_A is obtained from (4.13) and (4.15) as:

$$\begin{aligned} E_A &= \frac{c_4 s^3 + c_3 s^2 + c_2 s + c_1}{s^5 + \alpha_1 s^4 + \alpha_2 s^3 + \alpha_3 s^2 + \alpha_4 s + \alpha_5} \\ c_1 &= (b_M + b_T) k / (m_M m_T) \\ c_2 &= \left[b_M b_T + (b_M + b_T) c + (m_M + m_T) k \right] / (m_M m_T) \\ c_3 &= \left[b_M m_T + b_T m_M + (m_M + m_T) c \right] / (m_M m_T) \\ \alpha_1 &= \left[b_M m_T + b_T m_M + (m_M + m_T) c + K_D m_T \right] / (m_M m_T) \\ \alpha_2 &= \frac{b_M b_T + (b_M + b_T) c + (m_M + m_T) k + (c + b_T) K_D + K_P m_T}{m_M m_T} \\ \alpha_3 &= \left[(b_M + b_T) k + K_D k + K_P (c + b_T) + K_I m_T \right] / (m_M m_T) \\ \alpha_4 &= \left(K_P k + K_I (c + b_T) \right) / (m_M m_T),\ \alpha_5 = K_I k / (m_M m_T) \end{aligned} \tag{4.16}$$

Once E_A is obtained, inverse loop transmission L^{-1} is estimated:

$$L^{-1} = \left(\left(E_A s^2 \right)^{-1} - 1 \right)^{-1} \tag{4.17}$$

4.3.1. Experimental Validation and Iterative Tuning

The proposed closed-loop identification strategy for the CLDC pre-filter is first validated on an industrial scale 3-axis Cartesian CNC machine tool shown in Figure 17.a. Figure 17.b. shows motor and table side open loop FRFs (G_M and G_T) of x and y axes. As shown, both axes suffer from multiple resonances and anti-resonances. The 1st (dominant) anti-resonance is at ~71[Hz] for x axis, and at ~54[Hz] for y axis, as highlighted in Figure 17.b. These are followed by the resonances at ~84[Hz] (x axis) and ~88[Hz] (y axis). The motor-to-table TF G_{MT} (see Figure 17.c) clearly shows anti-resonance/resonance effects and structural dynamics between motor and the table. Both x and y axes are controlled by industrial collocated (motor FB) PID controllers (C) with inertia (acceleration) FF. In order to identify the filter parameters, both axes are moved by a simple trajectory shown in Figure 18.a. The trajectory consists of simple multi-step velocity commands generated by typical jerk limited acceleration profile [10]. Note that jerk limit should be selected high for wideband excitation of dynamics [1].

The proposed state-space identification procedure described above is then applied to estimate loop transmission TFs (L) for x and y axes (see (4.17)). Figure 18.b shows the identification performance. Estimated L captures fundamental physics of lumped-mass model as well as the controller dynamics. However, notice that at high frequencies (>100[Hz]), severe phase loss is observed. This is caused by higher order dynamics of the feed drive system, low pass filtering and amplifier delay.

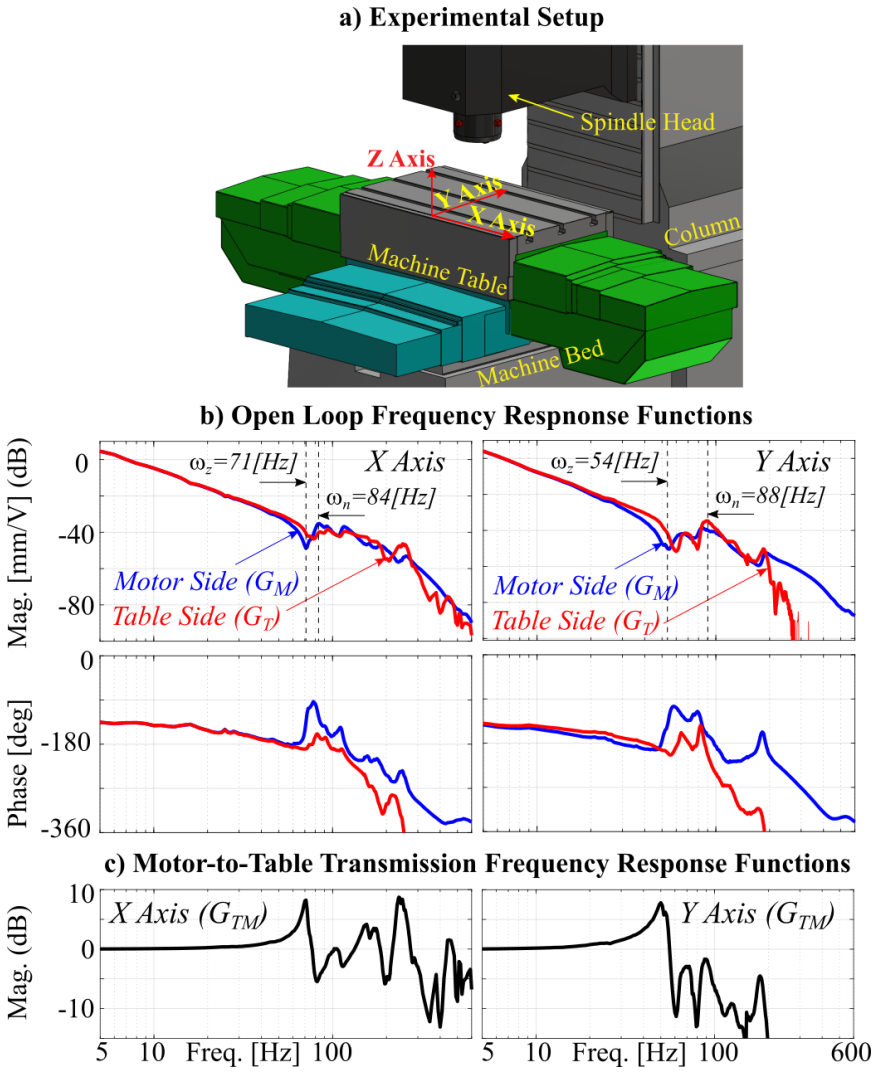

Figure 17. Illustration of the experimental setup used and measured frequency response functions (FRFs).

In an effort to further improve identification fidelity and widen tracking bandwidth, estimate of L is augmented with a finite impulse response (FIR) filter and the final form of F_{CLDC} is postulated as:

$$F_{CLDC} = L^{-1}\left(m_0 + m_1 z^{-1} + m_2 z^{-2}\right) \tag{4.18}$$

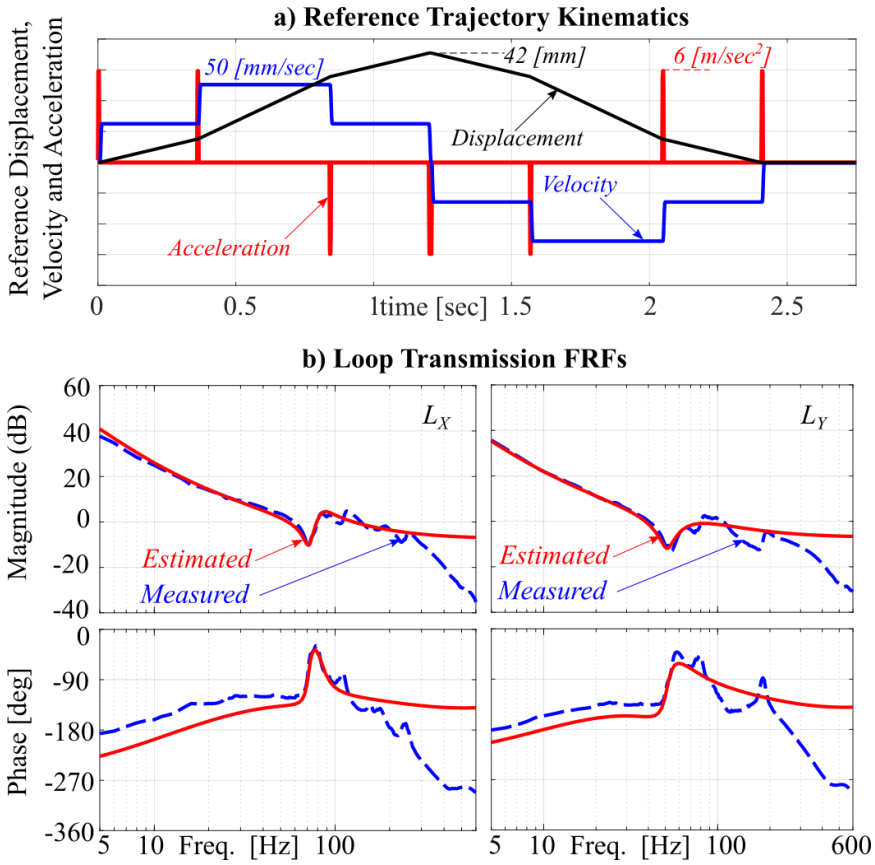

Figure 18. Experimentally measured and estimated loop transmission FRFs (L).

This additional FIR term helps recover the phase loss and retain collocated positioning accuracy. Parameters of added FIR filter, $m_0 \ldots m_2$ are obtained through data-based iterative tuning by solving the following optimization problem

$$\min_{\boldsymbol{\eta}=[m_0 \;\; m_1 \;\; m_2]^T} \left(J_{CLDC} = \frac{1}{2} \mathbf{e}_M^T \mathbf{e}_M \right) \tag{4.19}$$

through machine-in-the-loop (MIL) iterations. Motion trajectory (see Figure 18.a) is commanded, and motor tracking errors $\mathbf{e}_M$ are recorded. Based on the error signal, unknown FIR filter parameters m_0, m_1 and m_2 are iteratively identified by moving the axis back-and-forth with the same reference trajectory several times. In order to solve (4.19) iteratively, gradient (∇J_{CLDC}) and Hessian ($\nabla^2 J_{CLDC}$) of the objective function are needed. This can be extracted from gradient of $\mathbf{e}_M$:

$$
\begin{aligned}
& e_M = x_R - \left(1 + F_{CLDC}\right) T_M x_R \\
& \nabla e_M = \partial e_M / \partial \boldsymbol{\eta} = -\nabla F_{CLDC}\, T_M x_R = -\begin{bmatrix} 1 & z^{-1} & z^{-2} \end{bmatrix}^T L^{-1} x_M \\
& \nabla J_{CLDC} = \mathbf{e}_M^T \nabla \mathbf{e}_M, \;\; \nabla^2 J_{CLDC} = \nabla \mathbf{e}_M^T \nabla \mathbf{e}_M
\end{aligned}
\qquad (4.20)
$$

Notice that the actual motor position (x_M) appears in (4.20), and this means that the gradient (∇) and Hessian (∇^2) of J_{CLDC} can be obtained in a data-based fashion without requiring any system model, and the parameters $\boldsymbol{\eta}=[m_0 \ldots m_2]^T$ are optimized iteratively with the following update law:

$$
\boldsymbol{\eta}^{n+1} = \boldsymbol{\eta}^n - \alpha_{CLDC} \left(\nabla^2 J_{CLDC}\right)^{-1} \left(\nabla J_{CLDC}\right) \qquad (4.21)
$$

where n is the iteration counter, and α_{CLCD} is the learning rate. Substituting (4.20) into (4.21), parameter update law can be expressed as a linear dynamic system in discrete-iteration domain as:

$$
\begin{aligned}
& \boldsymbol{\eta}^{n+1} = \boldsymbol{\lambda}_{CLDC} \boldsymbol{\eta}^n + \boldsymbol{\xi}_{CLDC} \\
& \text{where: } \boldsymbol{\lambda}_{CLDC} = I - \alpha_{CLDC} \left(\mathbf{Q}^T \mathbf{Q}\right)^{-1} \mathbf{Q}^T \mathbf{Q} \\
& \qquad \boldsymbol{\xi}_{CLDC} = \alpha_{CLDC} \left(\mathbf{Q}^T \mathbf{Q}\right)^{-1} \left(\mathbf{x}_M^k - \mathbf{x}_R^k\right) \\
& \qquad \mathbf{Q} = \mathbf{L}_{INV} \begin{bmatrix} \mathbf{x}_M^k & \mathbf{x}_M^{k-1} & \mathbf{x}_M^{k-2} \end{bmatrix}
\end{aligned}
\qquad (4.22)
$$

where $\mathbf{L}_{INV}$ is the Toeplitz matrix representing L^{-1} in lifted domain. k is the time-counter such that $\mathbf{x}_M{}^k=[x_M(2T_s)\ldots x_M(NT_s)]^T$, $\mathbf{x}_M{}^{k-1}=[x_M(T_s)\ldots x_M((N\text{-}1)T_s)]^T$ and $\mathbf{x}_M{}^{k-2}=[x_M(0)\ldots x_M((N\text{-}2)T_s)]^T$, where N is the total number of samples in the experiment, and T_s is the sampling time. $\boldsymbol{\lambda}_{CLDC}$ and $\boldsymbol{\xi}_{CLDC}$ are the state transition and input matrices of the dynamic system represented by (4.22), and stability of (4.22) is guaranteed if the eigenvalues of $\boldsymbol{\lambda}_{CLDC}$ are inside the unit circle, i.e $|\text{eig}(\boldsymbol{\lambda}_{CLDC})|\leq 1$. It follows from (4.22) that all of the eigenvalues of $\boldsymbol{\lambda}_{CLDC}$ are equal to $1\text{-}\alpha_{CLDC}$, and thus MIL iterations described by (4.21) are stable for $0\leq\alpha_{CLCD}\leq 2$ [8]. In the proposed study, $\alpha_{CLCD}=1$ is used to mitigate the effect of measurement noise.

The iterative tuning procedure (4.21) is implemented on the experimental setup (see Figure 17.a) with the reference motion trajectory shown in Figure 18.a. Results are presented in Figure 19. As shown from Figure 19.a, parameter convergence is achieved within 2-3 iterations. Figure 19.b. validates that the command tracking performance on the motor side is improved greatly.

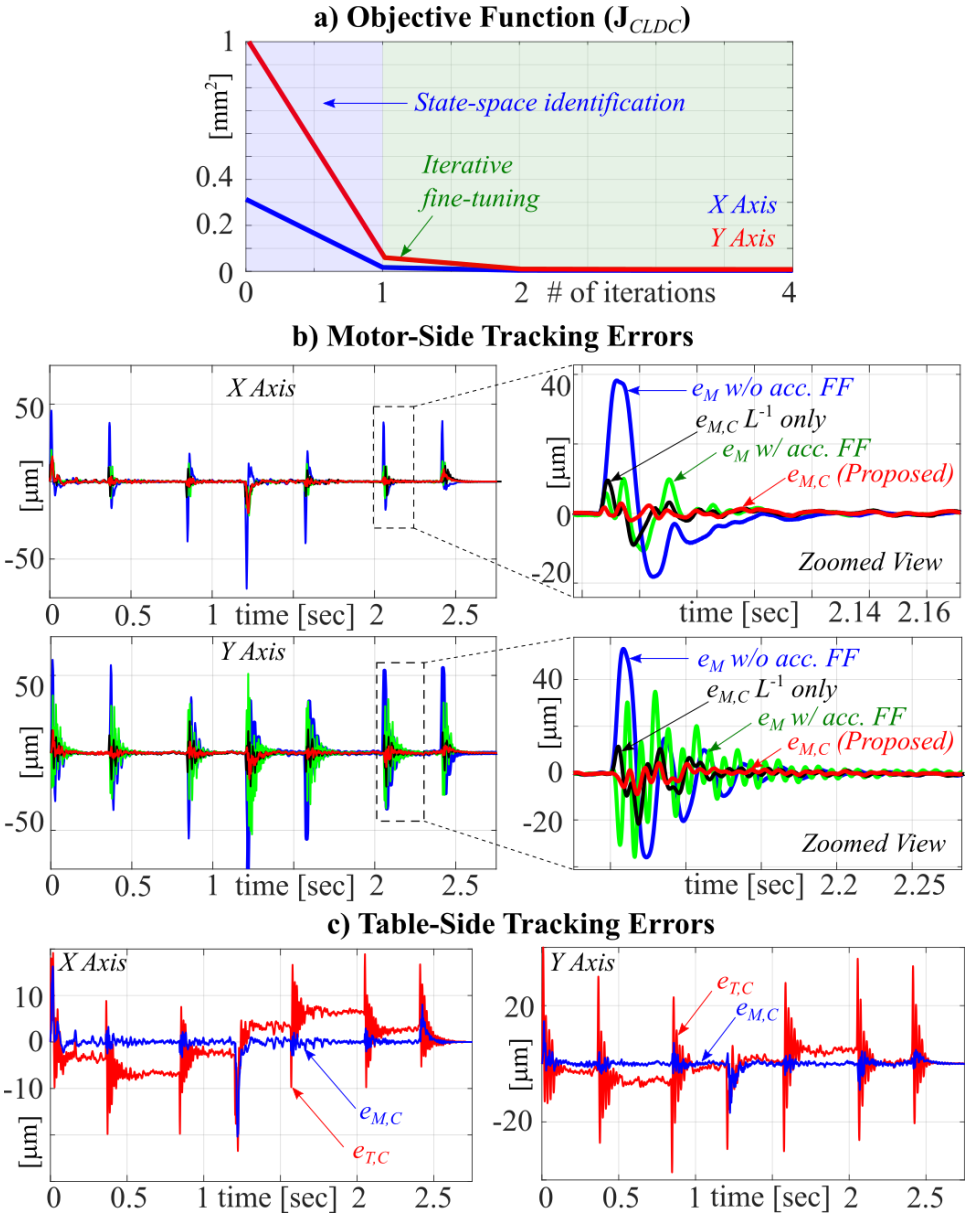

Figure 19. Experimental validation of the CLDC pre-compensator.

Uncompensated PID controller without acceleration FF results in large tracking errors. Adding acceleration FF to the controller increases high frequency tracking errors at the expense of low frequency positioning accuracy. Proposed CLDC ($e_{M,C}$) pre-filter eliminates both low frequency (inertial and viscous friction induced) errors and high frequency (structural vibration-induced) errors. Notice that when CLDC is first implemented as $F_{CLDC}=L^{-1}$, it immediately improves tracking performance. When augmented with the iteratively tuned FIR filter (see (4.18)), it achieves near-perfect

motor-side (collocated) positioning accuracy. Nevertheless, it should be noted from Figure 19.c that the table-side tracking errors ($e_{T,C}$) are still visible and degrade the table positioning accuracy. This is due to the anti-resonance behavior where table mass moves relative to the motor. The pre-filtering strategy in the following section is proposed to compensate those dynamics.

4.4. Design of the Rotary Command Generator (RCG)

CLDC minimizes motor-side (collated) tracking errors. Thus, it provides near-perfect motor side tracking performance. However, the ultimate goal of a BS system is accurate positioning of the table rather than the motor. Table mass vibrates w.r.t. the motor at the anti-resonance frequency, which hinders dynamic table positioning accuracy even with the CLDC pre-filter applied. To circumvent this, as shown in Figure 15, a Rotary Command Generator (RCG) pre-filter F_{RCG} is designed to further modify original reference trajectory. RCG aims to modulate the reference trajectory so that the table (x_T) follows the motor accurately. The form of F_{RCG} is selected as:

$$F_{RCG} = G_{TM}^{-1} - 1 \cong \frac{m_T}{k} s^2 + \frac{(c + b_T)}{k} s \tag{4.23}$$

so that

$$\frac{x_{T,CR}}{x_R} = (1 + F_{RCG}) \underbrace{(1 + F_{CLDC}) T_M}_{\approx 1} G_{TM} \cong 1 \tag{4.24}$$

where G_{TM} is the motor-to-table motion transmission TF, and T_M is the uncompensated closed loop motor dynamics. $x_{T,CR}$ denotes the table position compensated by both CLDC and RCG. Notice that with the use of CLDC, motor-side closed loop tracking performance is assumed to be near-perfect: $(1+F_{CLDC})T_M \cong 1$. Ball-screw stiffness is significantly larger than the viscous damping coefficient; $k >> c$, and hence the zero of G_T is neglected in (4.23). For systems that can accurately be modeled by a 2nd order lumped mass model given by (4.1) (e.g. Figure 16.b), the form of G_{TM} given in (4.23) would suffice to design F_{RCG}. However, as seen in Figure 17.c, in realistic systems both axes exhibit higher order motor-to-table motion transmission dynamics. Therefore, a more generalized approach is adapted here, and higher order structural dynamics

between motor and table is considered by the following TF:

$$\frac{x_T}{x_M} = G_{TM} = \prod_{\substack{r=1 \\ o=1}}^{R,O} \left(\frac{s^2 + 2\zeta_{z,o}\omega_{z,o}s + \omega_{z,o}^2}{s^2 + 2\zeta_{p,r}\omega_{p,r}s + \omega_{p,r}^2} \right) \left(\frac{\omega_{p,r}^2}{\omega_{z,o}^2} \right) \qquad (4.25)$$
$$F_{RCG} = G_{TM}^{-1} - 1$$

where R is the total number of poles, and O is the total number of zeros of G_{TM}. $\omega_{z,o}$ and $\zeta_{z,o}$ are the natural frequency and damping ratio of the anti-resonances, and $\omega_{p,r}$ and $\zeta_{p,r}$ are the natural frequency and damping ratio of the resonances. Parameters of F_{RCG} are identified through a two-step process. Firstly, in step 1) denominator (poles) of F_{RCG} is determined by offline least-squares optimization based on command tracking data. Next, in step 2) its numerator (zeros) is optimized through machine-in-the-loop iterations for best performance. Steps 1) and 2) are realized by solving convex optimization problems as described in the following.

First, axes are moved back-and-forth with a simple trajectory such as the one shown in Figure 18.a. The goal is to acquire a simple estimate for the poles of G_{TM}. Only the CLDC filter is used in this experiment. Reference position as well as the motor ($x_{M,C}$) and table ($x_{T,C}$) displacements are recorded, and the following least squares problem is postulated based on (4.25) as:

$$\min_{\boldsymbol{\theta}} \left\| \boldsymbol{\Phi}\boldsymbol{\theta} - \boldsymbol{\Psi} \right\|_2^2$$
$$\boldsymbol{\Phi} = \begin{bmatrix} \ddot{x}_M(0) & \dot{x}_M(0) & x_M(0) & -\dot{x}_T(0) & -x_T(0) \\ \ddot{x}_M(T_s) & \dot{x}_M(T_s) & x_M(T_s) & -\dot{x}_T(T_s) & -x_T(T_s) \\ \vdots & \vdots & \vdots & \vdots & \vdots \\ \ddot{x}_M(NT_s) & \dot{x}_M(NT_s) & x_M(NT_s) & -\dot{x}_T(NT_s) & -x_T(NT_s) \end{bmatrix} \qquad (4.26)$$
$$\boldsymbol{\Psi} = \begin{bmatrix} \ddot{x}_T(0) \\ \ddot{x}_T(T_s) \\ \vdots \\ \ddot{x}_T(NT_s) \end{bmatrix}, \quad \boldsymbol{\theta} = \begin{bmatrix} \omega_{p,1}^2/\omega_{z,1}^2 \\ 2\zeta_{z,1}\omega_{p,1}^2/\omega_{z,1} \\ \omega_{p,1}^2 \\ 2\zeta_{p,1}\omega_{p,1} \\ \omega_{p,1}^2 \end{bmatrix}, \text{ subject to: } \begin{matrix} \boldsymbol{\theta}(3) = \boldsymbol{\theta}(5) \\ \text{and} \\ \boldsymbol{\theta} \geq \mathbf{0} \end{matrix}$$

By solving (4.26), an initial estimate of RCG parameters are obtained. Next, zeros of F_{RCG} are optimized through machine in the loop iterations. This is achieved by minimizing the difference between the motor displacement compensated by only CLDC ($x_{M,C}$) and table displacement compensated by both CLDC and RCG ($x_{T,CR}$) as:

$$\min_{\boldsymbol{\gamma}}\left(J_{RCG}=\frac{1}{2}\left(\mathbf{x}_{T,CR}-\mathbf{x}_{M,C}\right)^{T}\left(\mathbf{x}_{T,CR}-\mathbf{x}_{M,C}\right)\right) \tag{4.27}$$

where $\boldsymbol{\gamma}$ is the vector of unknowns defined by discretizing G_{TM} and extracting F_{RCG} for R=2 and O=1 as:

$$\begin{aligned} G_{TM}^{-1} &= 1+F_{RCG}=1+\frac{a_4z^{-4}+a_3z^{-3}+a_2z^{-2}+a_1z^{-1}+a_0}{b_2z^{-2}+b_1z^{-1}+b_0} \\ \boldsymbol{\gamma} &= \begin{bmatrix} a_0 & a_1 & a_2 & a_3 & a_4 \end{bmatrix}^{T} \end{aligned} \tag{4.28}$$

where $b_0 \ldots b_2$ define the discrete equivalent of the numerator of G_{TM} identified by solving (4.26), and $a_0 \ldots a_4$ define the numerator of F_{RCG} and are obtained iteratively. Notice that (4.27) poses a convex optimization problem, and its iterative solution can be guided to global optimality with the use of gradient (∇) and Hessian (∇^2) of its cost function J_{RCG}, which can be obtained as:

$$\begin{aligned} x_{T,CR}-x_{M,C} &= \left(1+F_{RCG}\right)\left(1+F_{CLDC}\right)T_M G_{TM} x_R \\ &\quad -\left(1+F_{CLDC}\right)T_M x_R \\ \nabla\left(x_{T,CR}-x_{M,C}\right) &= \nabla F_{RCG}\underbrace{\left(1+F_{CLDC}\right)T_M G_{TM} x_R}_{x_{T,C}} \\ \nabla F_{RCG} &= \frac{\partial F_{RCG}}{\partial \boldsymbol{\gamma}}=\frac{\begin{bmatrix} 1 & z^{-1} & z^{-2} & z^{-3} & z^{-4} \end{bmatrix}^{T}}{b_2z^{-2}+b_1z^{-1}+b_0} \\ \nabla J_{RCG} &= \left(x_{T,CR}-x_{M,C}\right)^{T}\nabla\left(x_{T,CR}-x_{M,C}\right) \\ \nabla^2 J_{RCG} &= \nabla\left(x_{T,CR}-x_{M,C}\right)^{T}\nabla\left(x_{T,CR}-x_{M,C}\right) \end{aligned} \tag{4.29}$$

Notice that the table motion compensated only by CLDC ($x_{T,C}$) naturally appears in the calculation of $\nabla(x_{T,CR}-x_{M,C})$, which is measurable. Therefore, ∇J_{RCG} and $\nabla^2 J_{RCG}$ can be obtained by using only measurement data, without relying on any system model. Once the gradient and Hessian of the objective function J_{RCG} are obtained, (4.27) is solved iteratively by moving each axis back-and-forth at each iteration [4] and updating the filter parameters $\boldsymbol{\gamma}=[a_0 \ldots a_4]^T$ with the following update law:

$$\boldsymbol{\gamma}^{n+1}=\boldsymbol{\gamma}^{n}-\alpha_{RCG}\left(\nabla^2 J_{RCG}\right)^{-1}\nabla J_{RCG} \tag{4.30}$$

where n is the iteration counter and α_{RCG} is the learning rate with α_{RCG}=1. Similar to (4.22), (4.30) can also be written as a linear dynamic system in discrete-iteration domain, and it can be shown that its stability is guaranteed with $0 \leq \alpha_{RCG} \leq 2$ [8].

4.4.1. Experimental Validation

Performance of the RCG is validated on the same experimental setup shown in Figure 17.a. Equations (4.26) and (4.30) are jointly used to optimize poles and zeros of F_{RCG}. The reference trajectory in Figure 18.a is used for machine in the loop iterations. Figure 20 summarizes performance of the RCG pre-filter. As shown in Figure 20.a, when the RCG filter is not used (iteration 0), large discrepancy between motor and table position can be observed. In fact, every-time when an acceleration transient is commanded, it excites the anti-resonance mode and causes large table vibrations. After the least squares fitting and iterative tuning, the RCG filter ensures that table follows reference motion accurately. As shown, the discrepancy in the table position is greatly attenuated. Figure 20.b indicates the monotonic parameter converge, and Figure 20.c shows overall improvement achieved at the table positioning accuracy with the application of combined CLDC + RCG pre-filters. Proposed pre-filters are benchmarked against Zero Phase Error Tracking Controller (ZPETC) [64] and conventional rigid body (acceleration) FF controller. ZPETC is designed to approximate inverse of closed loop table tracking dynamics $(x_T/x_R)^{-1}$ [64], and its numerator parameters are optimized through ILC framework [4] for better performance and a fair comparison.

As seen from Figure 20.c, conventional FF controller clearly excites high order vibratory dynamics of the BS system and causes large positioning errors. ZPETC (optimized with MIL iterations) improves the performance. It aims to eliminate errors caused by resonance and anti-resonance vibrations as well as closed loop servo dynamics all at once. This limits the error reduction provided by ZPETC. In contrast, proposed pre-filter pack (CLDC+RCG) targets resonance and anti-resonance-induced errors separately, and thus it performs the best among the three strategies as demonstrated in Figure 20.c. However, nonlinear friction-induced errors are dominant in the vicinity of the velocity reversal, which occur at t=1.22[sec], as well as at the beginning of motion ($t\cong$0[sec]). These errors cannot be eliminated by such linear pre-filtering. The following section introduces the proposed friction compensator strategy to specifically eliminate those friction induced positioning errors.

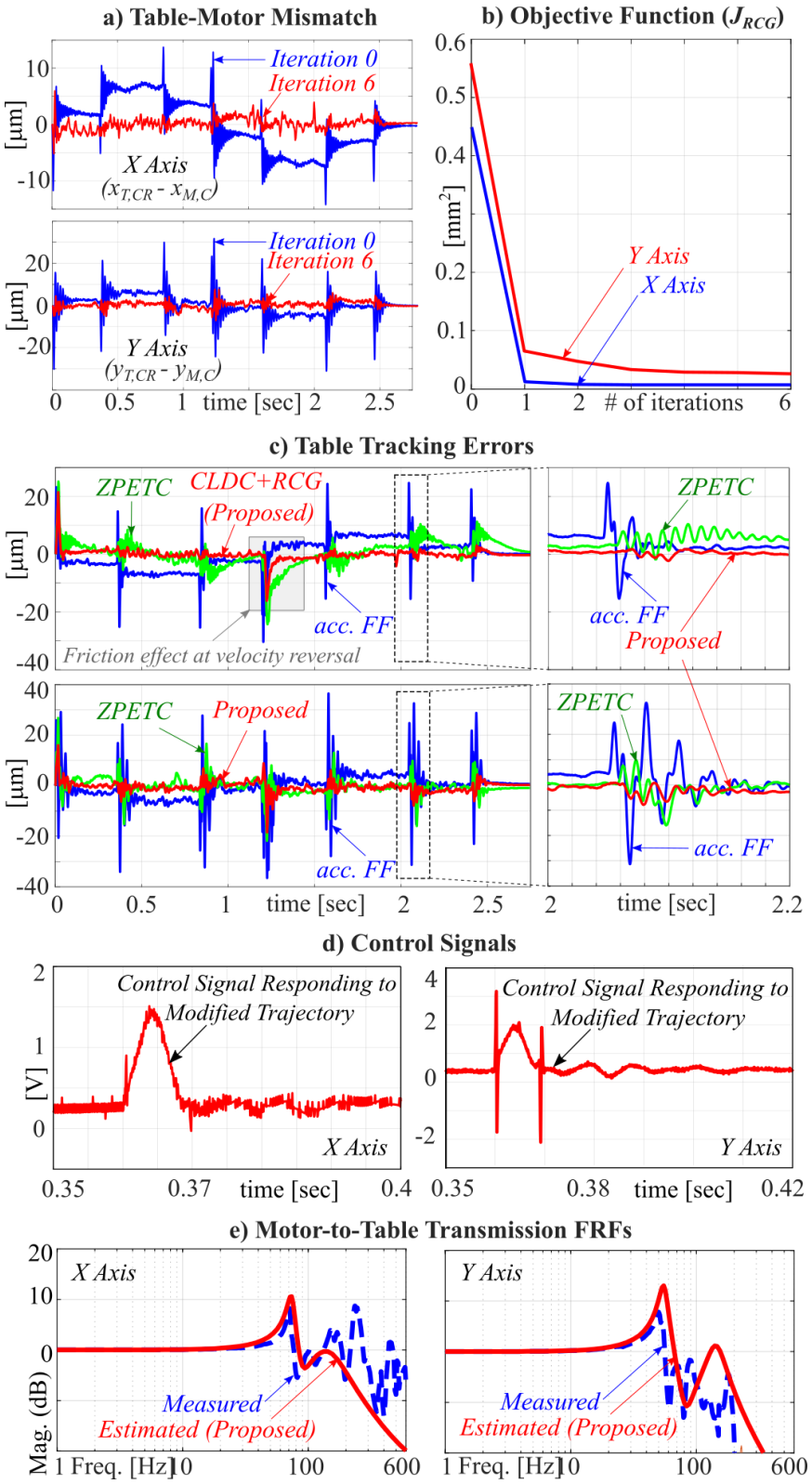

Figure 20. Experimental validation of the RCG pre-compensator.

4.5. Design of the Pre-Motion Friction Compensator (PMFC)

Typical industrial feed drive systems use mechanical bearings and guiding systems to support moving components [12]. As a result, majority of motion systems suffer from friction induced disturbances during motion start [17], or when the motion changes its direction during velocity reversals [14]. Actual friction regime is rather complex, exhibiting both rapidly varying position dependent pre-sliding forces [61], and also slowly varying velocity dependent viscous drag component [60]. Most high bandwidth controllers can reject viscous friction forces [6], or FF compensators can be used to eliminate them efficiently. However, pre-sliding friction forces cannot be rejected easily. This section presents design of a novel Pre-Motion Friction Compensator (PMFC) shown in Figure 15. Proposed compensator offsets (compensates) reference position commands so that friction induced tracking errors are eliminated.

Pre-filters CLDC and RCG eliminate linear servo dynamics induced tracking errors. The remaining source of errors becomes the pre-motion friction, and those friction-induced tracking errors (e_F) can be expressed from Figure 15 as:

$$e_F = f_F \frac{G_M}{1+G_M C} G_{TM} - x_F T_M G_{TM} \tag{4.31}$$

where f_F is the friction force and x_F is the pre-compensation signal generated by the nonlinear PMFC filter (see Figure 15). Equation (4.31) reveals that, in order to eliminate friction induced errors ($e_F \cong 0$), reference trajectory should be offset by $x_F = C^{-1} f_F$ amount. Notice that the compensation signal x_F is the controller-inverse-filtered (C^{-1}) pre-motion friction force (f_F). To construct the x_F signal, controller dynamics C and an estimate of friction forces f_F are required. Controller gains can be either read directly from servo-controller, or C can be estimated from the already identified F_{CLDC} filter dynamics in section 4.3 by $C=(G_R F_{CLDC})^{-1}$, where $G_R=((m_M+m_T)s^2)^{-1}$ can be assumed as the rigid body axis dynamics. The friction force f_F; however, must be identified accurately. Here, it is estimated iteratively and explained as follows.

4.5.1. Novel Re-Formulation of the GMS Friction Model

Generalized Maxwell Slip (GMS) model [61] is well-known and widely used in motion control to model non-linear friction regime. GMS model captures the stick/slip friction regimes using massless Maxwell-Slip (MS) blocks that are connected with parallel springs (see Figure 21.b).

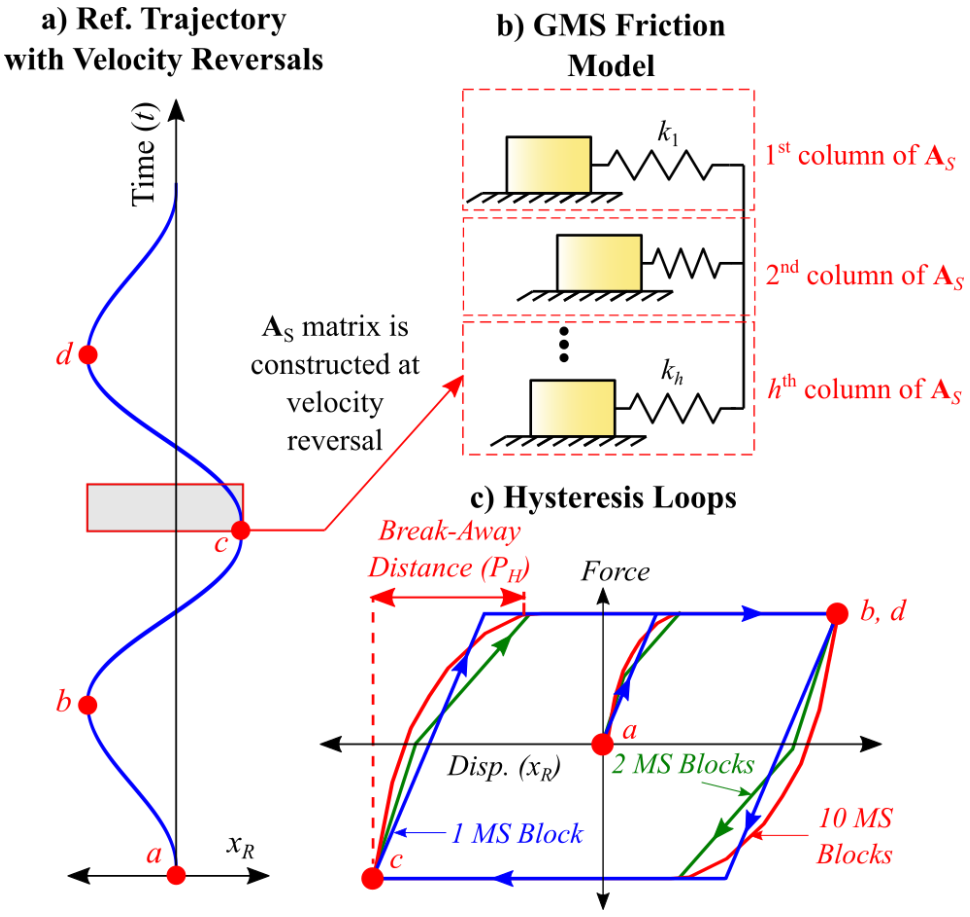

Figure 21. Proposed GMS model re-formulation.

Estimated friction force (f_{GMS}) by the conventional GMS model is given as [59]:

$$f_{GMS} = \sum_{h=1}^{H} f_h, \quad \frac{df_h}{dt} = \begin{cases} k_h \dot{x}_R, & \text{if stick (i.e. } f_h \le F_h) \\ 0, & \text{if slip (i.e. } f_h = F_h) \end{cases} \tag{4.32}$$

where k_h is the spring coefficient, and f_h is the force acting on the h^{th} block. F_h is the Coulomb friction force, and H is the number of MS blocks. During velocity reversal or a motion start, all blocks are stationary, i.e. sticking. As relative displacement is induced, MS blocks are loaded, where friction forces increase linearly w.r.t. axis

displacement. The "slipping" state for each block is then initiated when the load exceeds a threshold friction force, F_h. Notice that to build a GMS model, k_h and F_h must be identified with good fidelity by experimentally constructing force/displacement characteristics in time or frequency domain [17], [51] (see Figure 21.c).

The original GMS model above is designed in force domain, which means the stick/slip condition is controlled by the block forces (f_h in (4.32)) and threshold values F_h as [17]:

$$F_h = k_h P_h F_C \Big/ \left(\sum_{j=1}^{H} k_j P_j \right) \tag{4.33}$$

where P_h is the break-away distance of the h^{th} block, and F_C is constant. Notice that (4.32) and (4.33) clearly indicate that identification of individual spring coefficients (k_h) in the original GMS formulation is indeed non-linear [57], [17], which makes parameter identification cumbersome. Typically, nonconvex optimization techniques such as Dynamic Nonlinear Regression with Direct Application of Excitation (DNLRX) [57] or parameter varying state observers [69] are used that may even produce negative spring coefficients.

Firstly, in order to circumvent *force-dependency* of conventional GMS model, this paper proposes a re-formulated GMS, which postulates the hysteretic force/displacement relationship in a *position-dependent* formulation as:

$$f_{GMS} = \sum_{h=1}^{H} k_h z_h, \; \frac{dz_h}{dt} = \begin{cases} \dot{x}_R = v_R, & \text{if stick (i.e. } z_h \le |P_h/2|) \\ 0, & \text{if slip (i.e. } z_h > |P_h/2|) \end{cases} \tag{4.34}$$

where f_{GMS} is the estimated friction force. P_h is the break-away distance assigned to the h^{th} MS block, which dictates when the block starts slipping. As the motion system moves back-and-forth, friction forces follow a hysteresis loop w.r.t displacement, as shown in Figure 21.c. Each block starts its motion with sticking, and after traveling as much as its break away distance (P_h), it starts slipping. This continues until the block comes to a full stop and changes its direction of motion (velocity reversal). Notice that total break-away (stick) distance, P_H (see Figure 21.c) is a physical attribute to the motion system. Most precision motion platforms have stick distance in the range of 20~200 microns [14], and it can be identified from a simple closed-loop motion experiment by observing the tracking error and control signals. P_h can be then

distributed evenly among MS blocks to satisfy $P_1<P_2<\ldots<P_H$.

Furthermore, (4.34) can be put in matrix-vector form as:

$$\frac{d}{dt}\mathbf{f}_{GMS} = \mathbf{A}_S\mathbf{k}, \text{ where: } \mathbf{k} = \begin{bmatrix} k_1 & k_2 & \cdots & k_h \end{bmatrix}^T$$

$$\mathbf{A}_S = \begin{bmatrix} v_R(0) & v_R(0) & \cdots & v_R(0) \\ \vdots & \vdots & \cdots & \vdots \\ v_R(t_1) & v_R(t_1) & \cdots & v_R(t_1) \\ \vdots & \vdots & \cdots & \vdots \\ 0 & v_R(t_2) & \cdots & v_R(t_2) \\ \vdots & \vdots & \cdots & \vdots \\ 0 & 0 & \cdots & v_R(t_N) \end{bmatrix}_{N\times H} \tag{4.35}$$

where $\mathbf{k}$ is the vector of MS block spring coefficients, and $\mathbf{A}_S$ is the *spring activation matrix* that consists of sampled velocity command v_R. As the feed drive goes through a velocity reversal (Figure 21.a point *c*), columns of $\mathbf{A}_S$ keep track of MS block velocities. For instance, 1st column of $\mathbf{A}_S$ contains velocity of the 1st MS block, and the 2nd column contains velocity of the 2nd MS block. After a velocity reversal, every block starts from a sticking condition. The first block sticks until $t=t_1$, at which point it reaches its break-away displacement, i.e. $x_R(t_1)=P_1/2$. Then, it starts slipping; i.e. $v_R(t>t_1)=0$. The second block sticks a little longer, until $x_R(t_2)=P_2/2$. This pattern continues until each block completes sticking, and it starts over when a velocity reversal occurs. $\mathbf{A}_S$ can be pre-determined (constructed) once the reference trajectory profile (4.35) is known.

4.5.2. Iterative Fine-Tuning and Experimental Validation

The *spring activation matrix* $\mathbf{A}_S$ provides a trajectory dependent *linear* mapping from $\mathbf{k}$ to $\mathbf{f}_{GMS}$ (see (4.35)), and it allows us to formulate the following optimization problem in a convex manner where MS parameters are identified to minimize the friction induced errors by:

$$\min_{\mathbf{k}}\left(J_{PMFC} = \frac{1}{2}\mathbf{e}_F^T\mathbf{e}_F \right), \text{ subject to: } \mathbf{k} \geq \mathbf{0} \tag{4.36}$$

where $\mathbf{e}_F$ is the error vector given in (4.31).

Above optimization problem (4.36) is then solved to identify the MS block spring coefficients through machine-in-the-loop iterations. Notice that inequality constraints

$\mathbf{k} \geq 0$ are required to ensure that spring coefficients are physically meaningful. This is achieved by the help of gradient projection method [70], which is baked into MIL loop iterations as follows.

Firstly, Newton's second order iteration scheme is used to determine the *unconstrained update* of the spring coefficients $\mathbf{k}_{unc}$ as:

$$\begin{aligned} &\mathbf{k}_{unc} = \mathbf{k}^n - \alpha_{PMFC} \left(\nabla^2 J_{PMFC} \right)^{-1} \nabla J_{PMFC} \\ &\text{where: } \nabla J_{PMFC} = \nabla \mathbf{e}_F^T \mathbf{e}_F, \ \nabla^2 J_{PMFC} = \nabla \mathbf{e}_F^T \nabla \mathbf{e}_F \\ &\nabla \mathbf{e}_F = \frac{\partial \mathbf{e}_F}{\partial \mathbf{k}} = \mathbf{C}_{INV} \mathbf{T}_T \left(\int_{t=0}^{t_N} \mathbf{A}_S \, dt \right) \end{aligned} \tag{4.37}$$

where α_{PMFC} is the learning rate for the *unconstrained update*, and n is the iteration counter. $\mathbf{C}_{INV}$ and $\mathbf{T}_T$ are the Toeplitz matrices representing C^{-1} and T_T in lifted domain, and column-wise integration of $\mathbf{A}_S$ can easily be obtained numerically through trapezoidal methods. It is crucial to notice that, owing to the newly proposed reformulation of the GMS model (see (4.34) and (4.35)), $\nabla \mathbf{e}_F$ does not depend on $\mathbf{k}$ (see (4.37)). This makes (4.36) a convex optimization problem, since $\nabla^2 J_{PMFC} = (\nabla \mathbf{e}_F)^T \nabla \mathbf{e}_F \geq 0$. $\mathbf{k}_{unc}$ may violate constraints ($\mathbf{k} \geq 0$) given in (4.36). Thus, it is projected back onto the feasible set:

$$\mathbf{k}_{proj} = \max \left\{ \mathbf{k}_{unc}, \, 0 \right\} \tag{4.38}$$

where $\mathbf{k}_{proj}$ denotes its projection. The active constraints of this iteration are determined by the step size α_{PMFC}, and the goal is to find the first local minimizer of J_{PMFC} along the search path defined by (4.37). This is achieved by performing line search to find the optimal projection learning rate α_{proj} by:

$$\begin{aligned} &\alpha_{proj} = \arg\min_{\alpha_{PMFC}} \left(\left(\mathbf{e}_F^{n+1} \right)^T \mathbf{e}_F^{n+1} \right) \\ &\text{where: } \mathbf{e}_F^{n+1} = \mathbf{e}_F^n + \nabla \mathbf{e}_F \mathbf{k}_{proj} + \underbrace{\frac{\nabla^2 \mathbf{e}_F}{2!} \mathbf{k}_{proj}^2 + \cdots}_{0} \end{aligned} \tag{4.39}$$

where $\mathbf{e}_F{}^n$ is the recorded tracking error signal at the n^{th} iteration. α_{proj} is the projection learning rate (step size), which minimizes the *expected error* at the $(n+1)^{\text{th}}$ iteration according to the update law given by (4.38). Projected MS block spring coefficients ($\mathbf{k}_{proj}$) are calculated from (4.38) using the projection rate α_{proj}. Some components of

$\mathbf{k}_{proj}$ may be on the *boundary* (Ω_n) of the feasible set, which is defined as:

$$\Omega_n\left(\mathbf{k}_{proj}\right)=\left\{i \mid k_{proj,(i)}=0\right\} \tag{4.40}$$

Ω_n contains MS blocks with "zero" stiffness at the n^{th} iteration, and the spring coefficients residing in this set are called the *Cauchy points* [70].

The spring coefficients that are outside of Ω_n are optimized by fixing the Cauchy points and minimizing the expected error at the $(n+1)^{\text{th}}$ iteration by:

$$\begin{aligned}&\min_{\mathbf{k}}\left(J_{PMFC,n}=\frac{1}{2}\left(\mathbf{e}_F^{n+1}\right)^T\mathbf{e}_F^{n+1}\right),\ \text{subject to: } k_i=0,\ i\in\Omega_n\\&\text{where: } \mathbf{e}_F^{n+1}=\mathbf{e}_F^n+\nabla\mathbf{e}_F\mathbf{k}^{n+1}\end{aligned} \tag{4.41}$$

Equation (4.41) is a convex optimization problem with equality constraints, and therefore it can be solved to determine the parameter update law analytically as well;

$$\begin{aligned}&\mathbf{k}^{n+1}=\mathbf{k}^n+\alpha\Delta\mathbf{k}^n\\&\text{with: }\begin{bmatrix}\Delta\mathbf{k}^n\\ \boldsymbol{\lambda}^n\end{bmatrix}=\mathbf{H}^{-1}\begin{bmatrix}-\nabla\mathbf{e}_F^T\mathbf{e}_F^n\\ \mathbf{0}\end{bmatrix},\ \mathbf{H}=\begin{bmatrix}\nabla\mathbf{e}_F^T\nabla\mathbf{e}_F & \mathbf{C}_n^T\\ \mathbf{C}_n & \mathbf{0}\end{bmatrix}\end{aligned} \tag{4.42}$$

where α is the learning rate and $\boldsymbol{\lambda}$ is the vector of Lagrange Multipliers. $\mathbf{C}_n$ is the matrix of equality constraints in (4.41), which changes size every iteration as the contents of Ω_n vary. For example, for an iteration where the active set indices (i, see (4.40)) are only 4 and 5 ($\{4, 5\}\in\Omega_n$) and the number of MS blocks is H=10, $\mathbf{C}_n$ is constructed as:

$$\mathbf{C}_n=\overbrace{\begin{bmatrix}0\ \cdots\ 0 & 1 & 0 & 0\ \cdots\ 0\\ 0\ \cdots\ 0 & \underbrace{0}_{\text{Active constraints = \{4, 5\}}} & 1 & 0\ \cdots\ 0\end{bmatrix}}^{\text{Total number of MS blocks = 10}} \tag{4.43}$$

The solution of (4.42), $\mathbf{k}^{n+1}$, must be kept within the feasible region as well, i.e. $\mathbf{k}^{n+1}\geq 0$. This is achieved by either selecting α small enough to keep $\mathbf{k}^{n+1}$ feasible. Or, α is determined by simple line-search to minimize the predicted error at the $(n+1)^{\text{th}}$ iteration, and $\mathbf{k}^{n+1}$ is projected back onto the feasible set:

$$\begin{aligned}&\mathbf{k}^{n+1}=\max\left\{\mathbf{k}^n+\alpha\Delta\mathbf{k}^n,\ 0\right\}\\&\alpha_{opt}=\arg\min_{\alpha}\left(\left(\mathbf{e}_F^n+\nabla\mathbf{e}_F\mathbf{k}^{n+1}\right)^T\left(\mathbf{e}_F^n+\nabla\mathbf{e}_F\mathbf{k}^{n+1}\right)\right)\end{aligned} \tag{4.44}$$

Finally, (4.42) and (4.44) are used to guide the machine-in-the-loop iterations for optimizing the MS block spring coefficients safely to global optimality. Validation of the proposed friction pre-compensator is outlined in the following.

Cartesian axes of the experimental setup shown in Figure 17.a suffers from large friction induced errors as already shown in Figure 19 and Figure 20. Effectiveness of the proposed PMFC compensator is demonstrated during contouring tests along a diamond shaped trajectory as shown in Figure 22. Notice that the machine axes are commanded to travel around this shape in a non-stop manner by blending sharp corner geometry using the method described in [62]. The tangential velocity profile is shown in Figure 22.a, and the measured contouring errors are shown in Figure 22.b. Large contour errors occur at the corners of the profile when x and y axes reverse their direction of motion. Figure 22.c shows commanded and resultant tool-path geometry measured by the table encoder. Proposed PMFC is then applied on the top of CLDC and RCG pre-filters using 10 MS blocks. Figure 22.d shows convergence of the objective function. Notice that, when the tool-path is traveled only 2-3 times, Maxwell spring coefficients are identified with good accuracy. Proposed strategy is benchmarked against the conventional GMS model-based FF control as well [51]. Parameters of conventional GMS model are identified through offline manual curve-fitting to the hysteresis loops (see Figure 22.e). Notice that conventional (offline) GMS FF also decreases contouring errors; however, it is clearly outperformed by the proposed approach (CLDC+RCG+PMFC), which identifies GMS parameters while penalizing friction induced errors directly (by iteratively solving (4.36)) along the trajectory. In contrast, conventional (offline) GMS parameters are obtained separately from small stroke (300 [μm]) motion experiments. Friction forces estimated by the conventional GMS model fit to the hysteresis curve accurately (see Figure 22.e). However, they cannot capture the friction behavior at higher speed and stroke (see Figure 22.b). Friction characteristics of the machine may vary with the table location. Such offline GMS parameter fitting suffer from robustness and flexibility. In contrast, proposed PMFC pre-filter can be optimized easily to eliminate friction-induced errors on-the-fly while capturing changes in the friction regime based on temperature or operating region for example [59].

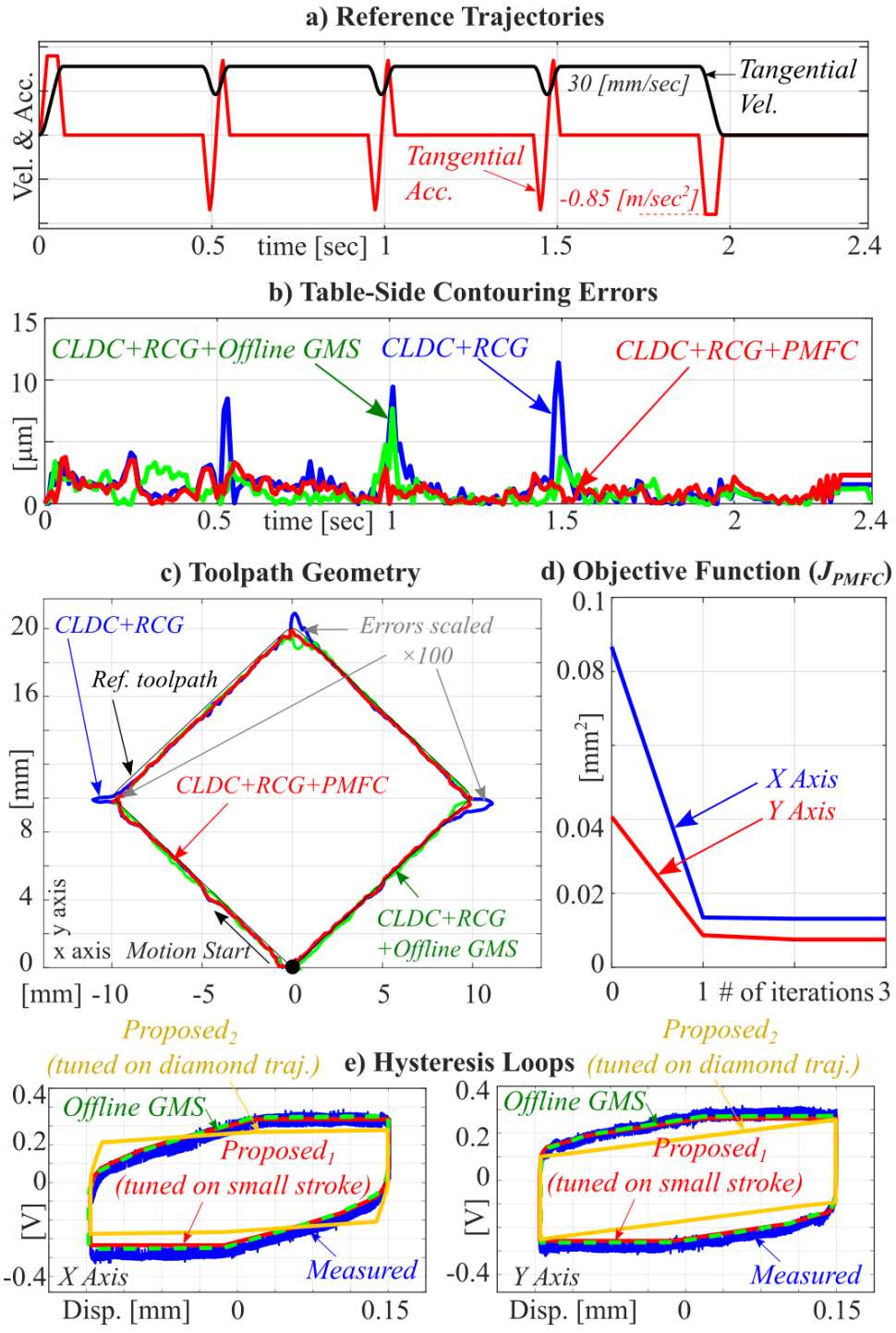

Figure 22. Experimental validation of the PMFC.

Notice from Figure 22.e that the friction forces estimated by PMFC pre-filter can slightly differ from the Hysteresis Loop measurements when its parameters are

optimized using the toolpath given in Figure 22.c (see *Proposed*$_2$ in Figure 22.e). However, since the main goal of the PMFC is to eliminate the positioning errors, inaccurate fitting of the Hysteresis Loop does not pose a problem. Figure 12.e also shows the performance of the PMFC filter iteratively optimized along the small stroke that is used to obtain the conventional GMS model parameters (see *Proposed*$_1$ in Figure 22.e). As observed, PMFC provides accurate curve fitting along the Hysteresis Loop in this case.

4.6. Conclusions

This paper presented a novel trajectory modification scheme based on 3 pre-filters to improve dynamic positioning accuracy of flexible precision motion systems. Each pre-filter targets a specific dynamic error source; namely, (i) positioning errors induced by closed loop servo-dynamics, (ii) structural vibrations (iii) and due to pre-motion friction disturbances. Each pre-filter is auto-tuned iteratively through data-based techniques that can be realized easily on-the-fly. The auto-tuning problem is posed as a convex optimization problem and global optimal solution is reached within several iterations. Proposed strategy is validated on a commercial CNC machine tool and shows that dynamic tracking errors can be improved up to 5× (see Figure 19 and Figure 20) and friction induced errors are reduced more than 3× (see Figure 22). Overall, proposed scheme can be implemented without intervention on the servo controller by only modifying reference motion trajectory conveniently.

ACTIVE CONTROL OF HIGH FREQUENCY CHATTER WITH MACHINE TOOL FEED DRIVES IN TURNING

Alper Dumanli and Burak Sencer

CIRP Annals – Manufacturing Technology
Submitted in January 2021, Under Review

5. Active Control of High Frequency Chatter with Machine Tool Feed Drives in Turning

This paper presents a new active vibration control strategy to mitigate high frequency regenerative chatter vibrations using machine tool feed drives. Rather than modal damping, proposed approach aims to control regenerative process dynamics to shape the Stability Lobe diagrams (SLD) and attain higher material removal rates. The controller is designed as a feedback filter whose parameters are optimized to compensate regeneration. The proposed strategy is applied to actively control orthogonal (plunge) turning dynamics where >2.5[kHz] chatter vibrations are suppressed by low bandwidth machine tool drives. Stability lobes are shaped locally to reach up to 4× higher material removal rates.

5.1. Introduction

Chatter vibrations have been a limiting factor for attaining larger material removal rates (MRR) in turning for decades [71]. They originate due the flexibilities (resonances) in the workpiece-machine-tooling structure and by the regeneration effects [71], [16]. Overall process-machine interaction can be modelled by a delay differential equation (DDE), and chatter-free cutting conditions are selected from Stability Lobe Diagrams (SLDs). Nevertheless, practical spindle speeds in turning are lower and when structural resonances are at high frequency, conventional SLDs have densely packed narrow lobes that cannot be used to maximize MRRs [16].

The overreaching goal has been to exceed stability limitations in turning, and it can be attained by shaping SLDs in two major ways; firstly, regeneration effect is targeted through process parameter selection such as exploiting process damping [72], optimizing tool geometry/posture [73], or by spindle speed variation (SSV) [16]. These efforts shape SLDs locally to create stable pockets to reach higher MRRs and designed to work on a pre-determined spindle speed region.

Another approach focuses on dampening structural resonances by passive or active systems [16], [74], [23], [75], [76], [77]. Increasing modal damping lifts SLDs up, which delivers moderate stability increase over a wider spindle speed range. Tuned-

mass-dampers (TMD), or tools with friction dampers [16] are widely used in practice, and their robustness can be enhanced semi-actively [23], [76]. However, fully active systems are much more effective since they can dampen multiple modes [75], integrate within machine elements [76], and even realized by using machine's existing feed drives [77]. A fundamental requirement for effective active damping is that targeted resonances must lie within the control bandwidth of the actuator or feed drive system, which limits their practical usage to dampen modes within ~200[Hz] range [16], [77]. Control algorithms based on direct velocity [74], [23] or acceleration feedback [77] are widely used. However, when low frequency resonances are damped actively, the lightly damped high frequency modes becomes destabilized. Therefore, loop shaping based tuning should be practiced [77], or model-based techniques such as H∞, μ-synthesis or delayed feedback [75], [78], [79] are employed. Still, fundamental limitation of modal damping-based chatter control techniques is that they rely on servo control bandwidth, which cannot be widened enough to dampen high frequency modes.

This paper presents a novel active chatter vibration control strategy for machine tool feed drives. As opposed to the injecting modal damping by servo loop shaping [80], [74], [23], [75], [76], [77], proposed controller is designed to achieve *process loop shaping*, which focuses on controlling regenerative machining process dynamics using machine tool feed drives. This approach brings two major advantages over state of the art. Firstly, core cause of chatter; regeneration effects are suppressed, which allows local shaping of SLDs to significantly increase MRR. Secondly, it allows control of high frequency chatter that is beyond the position bandwidth of feed drives. Figure 23.a depicts the proposed scheme. Proposed controller is designed as an add-on compensator (filter) strapped around the existing low-bandwidth servo controller to suppress chatter vibrations. Thus, both low frequency position control and high frequency chatter mitigation are achieved jointly. Following sections explain design, parameter tuning and experimental validation of proposed approach in orthogonal (plunge) turning.

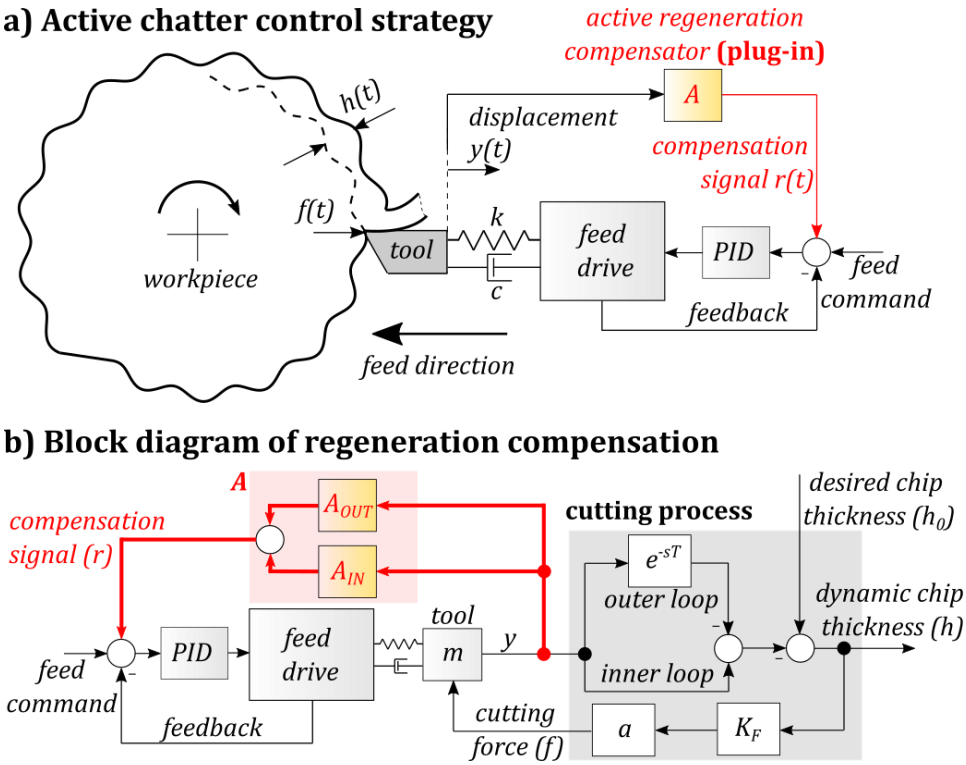

Figure 23. Illustration (a) and block diagram (b) of the proposed strategy.

5.2. Loop Transmission Dynamics of Orthogonal Cutting

Figure 23 illustrates the well-known dynamics of orthogonal turning [71], [16] with a flexible tool assembly carried by a feed drive system. Dynamic chip thickness $h(s)=L\{h(t)\}$ and feed forces $f(s)$ generated by current vibration of the tool tip $y(s)$ and the one left on part surface in previous spindle revolution, $e^{-sT}y(s)$:

$$h(s) = h_0 - [y(s) - e^{-sT} y(s)], \quad f(s) = K_F a h(s) \tag{5.1}$$

where s is the Laplace operator, T is the spindle (delay) period, h_0 is intended (static) chip thickness, K_F is the cutting force coefficient, and a is width (depth) of cut. Cutting forces excite the flexible structure and produce current vibrations as:

$$y(s) = G(s) f(s) = G(s) K_F a \left(h_0 - [y(s) - e^{-sT} y(s)] \right) \tag{5.2}$$

where $G(s)$ is the transfer function of the flexible tooling system. Laplace operator (s) is dropped from signals and functions in the remainder, and Eq. (5.2) is expressed in transfer function form as:

$$\frac{y}{h_0}=\frac{K_F aG}{1+aK_F G\left(1-e^{-sT}\right)}=\frac{K_F aG}{1+aL_P} \tag{5.3}$$

where the $L_P=K_FG(1-e^{-sT})$ term in Eq. (5.3) is the so-called "*process loop transmission*" dynamics with a being the process gain. Figure 24 shows its characteristics for a delay period, T. Process loop transmission follows amplified flexible tooling dynamics K_FG but modulated by the delay term $(1-e^{-sT})$, which contains the "regenerative effects" and introduces gain and phase ripples. It is due to those ripples that phase of L_P drops below -180[deg] right after resonance (ω_n), which marks the "chatter frequency" (ω_c) and determines min. gain margin of the process (See Figure 24.b). Note that limit width of cut becomes $a_{lim}=1/|L_P(j\omega_c)|$. SLDs are generated scanning gain margin of L_P over a set of spindle speeds.

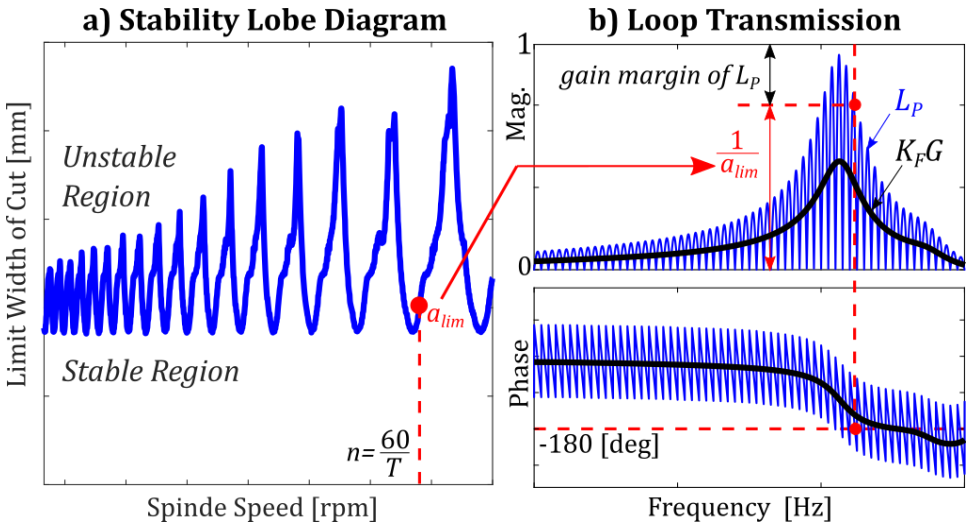

Figure 24. SLDs and Process Loop Transmission Dynamics.

The following sections present the design of proposed vibration compensator that actively uses machine tool feed drives to shape the *process loop transmission*. The design philosophy is to attenuate regeneration induced phase/gain ripples around the resonance to drastically improve process stability and, thereby suppress high frequency chatter vibrations that are beyond the tracking bandwidth of conventional servo control.

5.3. Design of Active Regeneration Cancelling Compensator

Block diagram of proposed control scheme is given in Figure 23.b. As shown, an add-on compensator (filter) is designed that injects a position compensation signal *r* based on the tool vibration measurement *y*. Its design is based on cancelling the inner and outer regeneration effects to shape the SLDs and to maximize the limit width of cut a_{lim} around a desired spindle (cutting) speed region. Therefore, it is called the Active Regeneration Compensator (ARC) and denoted by the transfer function, *A*.

With the introduction of ARC signal *r*, the augmented tool tip and process dynamics can be derived from Eq. (5.2) and Figure 23.b as:

$$y = Gf + AT_T y \rightarrow y = K_F aG\left[h_0 - y\left(1 - e^{-sT}\right)\right] + AT_T y \tag{5.4}$$

where $T_T = y/r$ is the tool tip tracking transfer function of feed drive system, which is typically governed by a low-bandwidth industrial PID controller. Equation (5.4) can be put in a transfer function form as:

$$\frac{y}{h_0} = \frac{K_F aG}{1 + K_F aG\left(1 - e^{-sT}\right) - AT_T} = \frac{K_F aG}{1 + L_{ARC}} \tag{5.5}$$

which reveals that the modified process loop transmission $L_{ARC} = K_F aG(1 - e^{-sT}) - AT_T$ is augmented by the ARC filter, *A*.

In order to effectively alter stability margins of L_{ARC}, *A* is designed with two parts: $A = A_{IN} + A_{OUT}$. A_{IN} targets the inner modulation loop to suppress effect of current tool vibration *y*, whereas A_{OUT} targets the delayed feedback dynamics due to the outer regeneration loop, $e^{-sT}y$. Equation (5.5) can be re-written explicitly in terms of those A_{IN} and A_{OUT} components as:

$$\frac{y}{h_0} = \frac{K_F aG}{1 + \underbrace{\left(K_F aG - A_{IN}T_T\right)}_{\substack{\text{inner modulation} \\ \text{cancellation}}} - \underbrace{\left(K_F aGe^{-sT} + A_{OUT}T_T\right)}_{\substack{\text{outer modulation} \\ \text{cancellation}}}} \tag{5.6}$$

Following sections present design of A_{IN} and A_{OUT} compensators to cancel the inner and outer modulation effects shown in Eq. (5.6).

5.3.1. Design of the Outer Modulation Compensator (A_{OUT})

A_{OUT} is designed to suppress the effect of outer modulation. Notice from Eq. (5.6) that if A_{OUT} could be ideally chosen as:

$$A_{OUT} = -K_F a G T_T^{-1} e^{-sT} \tag{5.7}$$

effect of outer regeneration is completely cancelled. a is the desired stable depth of cut, and G is the disturbance response of tool/feed drive system, which can be measured by tap-testing. However, the inverse of higher-order closed-loop tracking dynamics, T_T^{-1} term, cannot be realized on a practical system due to servo phase losses and non-minimum phase zeros [74], [23], [75], [76], [77]. Therefore, its delayed realization, the $T_T^{-1}e^{-sT}$ term in Eq. (5.7) is considered. The idea is to approximate $-T_T^{-1}e^{-sT}$ by an N^{th} order FIR filter within a meaningful frequency band $\omega \in [\omega_1,\ \omega_M]$ as:

$$P_{OUT} = p_1 z^{-T_1/T_s} + p_2 z^{-T_2/T_s} + \cdots + p_N z^{-T_N/T_s} \approx -T_T^{-1} e^{-sT}, \quad z = e^{sT_s} \tag{5.8}$$

with T_s being position loop sampling time. Frequency band $[\omega_1,\omega_M]$ is selected to confine chatter frequency by setting $\omega_1=\omega_n$ and ω_M is set reasonably larger. Notice that the delay T is known at a given spindle (cutting) speed, $T=60/n$. Filter delays $T_1 \ldots T_N$ are selected centered around that spindle period $[T_1 \ldots T_N] \leftrightarrow [T-2\pi/\omega_1 \ldots T+2\pi/\omega_1]$ to ensure causal inversion of T_T. Finally, gains of the FIR filter $p_1 \ldots p_N$ are determined to minimize its fitting discrepancy from system inverse, $\min \| P_{OUT}+T_T^{-1}e^{-sT} \|$ by:

$$\min_{p_1 \cdots p_N} \begin{pmatrix} \mathrm{Re}\left\{ P_{OUT}(j\omega) T_T(j\omega) + e^{-j\omega T} \right\}^2 \\ + \mathrm{Im}\left\{ P_{OUT}(j\omega) T_T(j\omega) + e^{-j\omega T} \right\}^2 \end{pmatrix} \text{ for all } \omega \in [\omega_1\ \ \omega_M] \tag{5.9}$$

which can be put in a matrix-vector form as:

$$\min_{\mathbf{p}=p_1\cdots p_N} \left\|\mathbf{\Lambda p}+\mathbf{v}\right\|_2^2, \quad \text{where:}$$

$$\mathbf{\Lambda}=\begin{bmatrix} \mathrm{Re}\left\{e^{-j\omega_1 T_1}T_T\left(j\omega_1\right)\right\} & \cdots & \mathrm{Re}\left\{e^{-j\omega_1 T_N}T_T\left(j\omega_1\right)\right\} \\ \vdots & \ddots & \vdots \\ \mathrm{Re}\left\{e^{-j\omega_1 T_1}T_T\left(j\omega_M\right)\right\} & \cdots & \mathrm{Re}\left\{e^{-j\omega_1 T_N}T_T\left(j\omega_M\right)\right\} \\ \mathrm{Im}\left\{e^{-j\omega_1 T_1}T_T\left(j\omega_1\right)\right\} & \cdots & \mathrm{Im}\left\{e^{-j\omega_1 T_N}T_T\left(j\omega_1\right)\right\} \\ \vdots & \ddots & \vdots \\ \mathrm{Im}\left\{e^{-j\omega_1 T_1}T_T\left(j\omega_M\right)\right\} & \cdots & \mathrm{Im}\left\{e^{-j\omega_1 T_N}T_T\left(j\omega_M\right)\right\} \end{bmatrix}$$

$$\mathbf{v}=\left[\cos\left(\omega_1\right)\ \cdots\ \cos\left(\omega_M\right)\ \sin\left(\omega_1\right)\ \cdots\ \sin\left(\omega_M\right)\right]^T \tag{5.10}$$

where M is the frequency resolution. Equation (5.10) is a convex optimization (least squares fitting) problem, which can be solved efficiently to determine FIR gains, and A_{OUT} is implemented as:

$$A_{OUT}=K_F aGP_{OUT} \tag{5.11}$$

An illustrative example is provided in Figure 25. When A_{OUT} is implemented, delay-induced phase ripples are robustly attenuated within [ω_1, ω_M]. As a result, 180[deg] phase crossing is shifted to high frequency, which increases gain margin of process loop transmission providing larger stable depth of cut (a_{lim}).

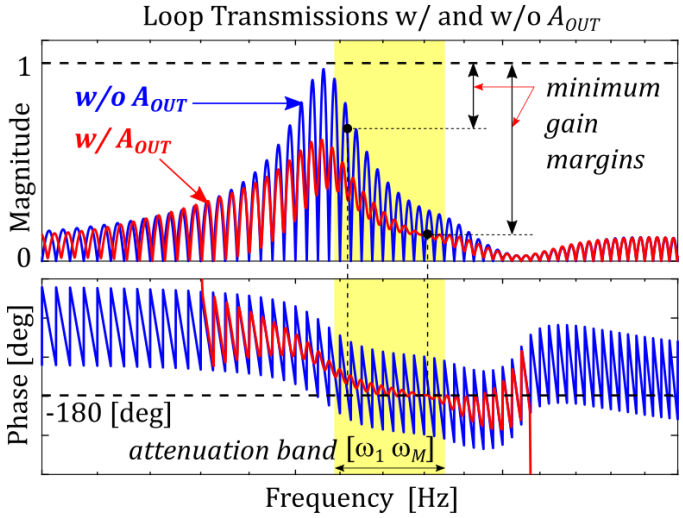

Figure 25. Outer regeneration cancellation using A_{OUT}.

5.3.2. Design of the Inner Modulation Compensator (A_{IN})

The A_{IN} compensator is designed to further increase a_{lim} around a targeted spindle speed by cancelling the effect of inner modulation. To cancel the inner modulation terms (see Eq. (5.6)), A_{IN} is selected in the form of:

$$A_{IN} = -K_F a G \hat{T}_T^{-1} P_{IN} \tag{5.12}$$

where $\hat{T}_T^{-1}$ is an approximate, causal inverse of feed drive's tracking dynamics, which neglects non-minimum phase zeros. Design of the P_{IN} filter in Eq. (5.12) is critical. Similar to the design of A_{OUT} compensator, P_{IN} is selected as simple K^{th} order FIR filter:

$$P_{IN} = q_0 + q_1 z^{-1} + \cdots + q_K z^{-K}, \quad z = e^{sT_s} \tag{5.13}$$

whose parameters $q_0 \ldots q_K$ are determined to maximize a_{lim} by minimizing the real part of process loop transmission. Based on Eq. (5.6), this parameter search is set as an optimization problem:

$$\min_{q_0 \cdots q_K} \left(\frac{1}{a_{\lim}} \right) \quad \text{subject to:}$$
$$-\mathrm{Re}\left\{ \underbrace{\left(K_F G - \underbrace{K_F G T_T \hat{T}_T^{-1} P_{IN}}_{A_{IN} T_T / a} \right)}_{\text{Inner modulation}} - \underbrace{\left(K_F G e^{-sT} + T_T A_{OUT} / a \right)}_{\text{Outer modulation}} \right\} \le \frac{1}{a_{\lim}} \tag{5.14}$$

Above optimization problem has two key elements. Firstly, the objective function tries to minimize $1/a_{lim}$, whereas its only constraint tries to keep the negative real part of loop transmission below that. Therefore, optimal filter parameters are sought that maximizes gain margin of the process by pushing the real crossing of process loop transmission to right-hand side of the complex plane. This parameter search is governed by Eq. (5.14), and it is in fact a convex optimization problem that can be solved conveniently using linear programming to determine the best filter parameters. With the P_{IN} filter determined from Eq. (5.14) proposed ARC design, $A = A_{OUT} + A_{IN}$ is implemented from Eqs. (5.11) and (5.12) as shown in Figure 23.b.

5.4. Experimental Validation

The experimental turning system setup used in validating proposed active chatter avoidance strategy is shown in Figure 26. Orthogonal tube cutting experiments are conducted on a Al6061 workpiece with a carbide insert, yielding roughly K_F=~1338 [N/mm^2]. A Dytran 3035B1G accelerometer with 10 [mV/g] sensitivity is used to measure the tooling dynamics G, and Figure 26.b shows measured and fitted FRFs. Notice that due to slender tool shank, the system suffers from a dominant mode at ~2.57 [kHz].

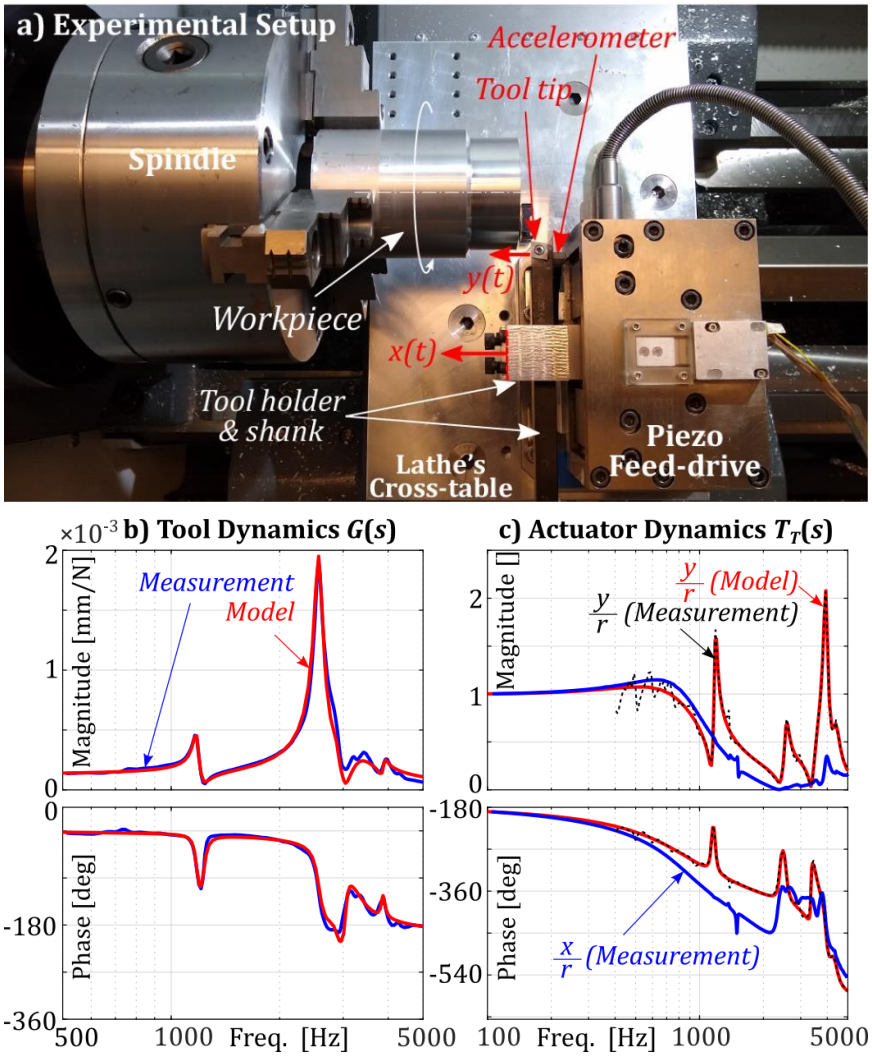

Figure 26. Experimental setup and its dynamic characterization.

As shown, the tool (shank) is fed to the workpiece by a piezo actuated feed drive system in this setup. Details of the drive system can be found in [81]. The actuator assembly contains an internal displacement sensor, which allows tuning a dedicated collocated PID controller with a maximum tracking bandwidth of 1[kHz] shown in Figure 26.c (see blue line, x/r). The sampling frequency of the real-time control system is set to 50 [kHz]. Tool tip tracking transfer function (T_T=y/r) is measured by integrating the tool tip acceleration measurements and shown in Figure 26.c.

Proposed active control algorithm ARC is first designed to suppress chatter due to the dominant mode at ~2.57 [kHz] (See Figure 26.b) by selecting the target frequency band as $\omega \in$ [2500, 2800] [Hz]. The objective is to open up a stable pocket at around n=1800 [rpm]. FIR filter orders of A_{IN} and A_{OUT} are set as N=20, K=5. Note that in realization of ARC, tool tip vibrations (y) are estimated from integrating accelerometer measurements and high-pass filtering with 250[Hz] cut-off.

Figure 27 shows the original and shaped process dynamics by ARC. As shown in Figure 27.a, A_{OUT} eliminates ripples due to the regeneration effect, and A_{IN} further minimizes the negative real part of process loop transmission. This improves the gain margin of the process significantly. It is also evident from Figure 27.b that process loop transmission is squeezed and pushed to the right-hand side of complex plane and the -1 point by the help of ARC.

Next, SLDs are plotted in Figure 28.a. As shown, due to high frequency resonance (~2.57[kHz]), the original stability lobes are very tight, and asymptotic stability limit is below ~0.5[mm]. However, when ARC is used, stability is drastically improved around the desired 1800[rpm]. Widths of cut up to ~2[mm] can be cut stably providing 4× improvement in productivity. Tube cutting experiments (plunge turning) at a feedrate of 4[μm/rev] are conducted. As shown, workpieces with 0.5-1.75[mm] wall thicknesses are machined free of chatter with a smooth surface finish by the help of the proposed ARC design.

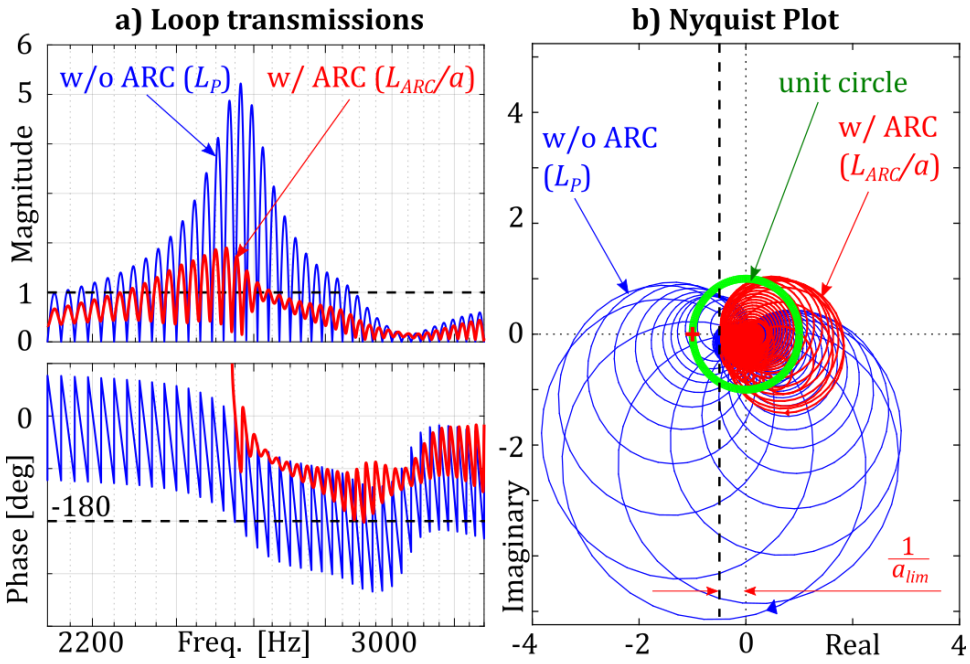

Figure 27. Process loop transmissions with and without ARC.

Figure 27.b shows the effect of ARC when it is switched on during machining at 1.75mm width. When ARC is turned on at ~2.5[sec], chatter vibrations at 2.66[kHz] are quickly dampened, and the process is stabilized. More importantly, ARC suppresses chatter vibrations originating from a mode beyond feed drive positioning bandwidth (~1[kHz]). This provides great flexibility since drive's servo controller can be designed separately and safely for positioning, and ARC is activated to suppress chatter when needed. Note that to take advantage of ARC for high frequency chatter avoidance, drives must be able to respond to at least small (micron level) position commands at that high frequency.

Lastly, ARC is implemented to create lobes at different spindle speeds such as at 1000 and 1400[rpm] to showcase its flexibility and robustness to increase MRR on demand in Figure 29. As shown, ARC can be tuned to create large stability lobes at various speeds. In comparison, delayed feedback control [79] can only provide minor improvement and requires tedious manual gain tuning.

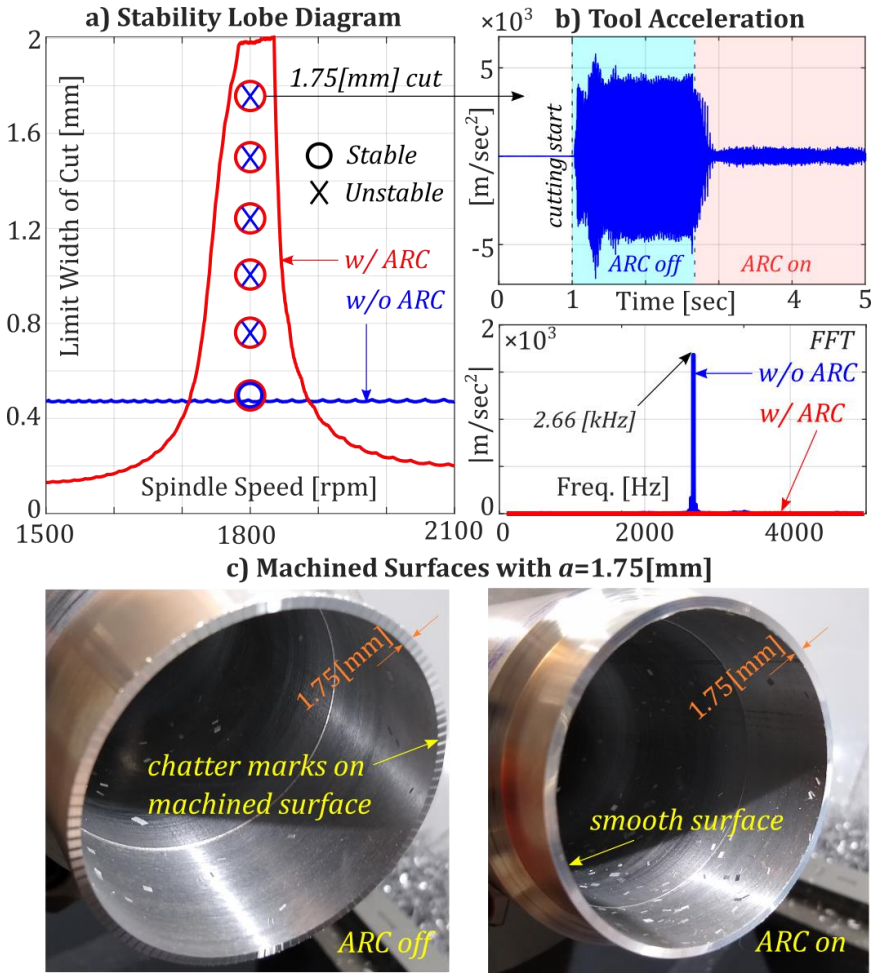

Figure 28. Experimental cutting results.

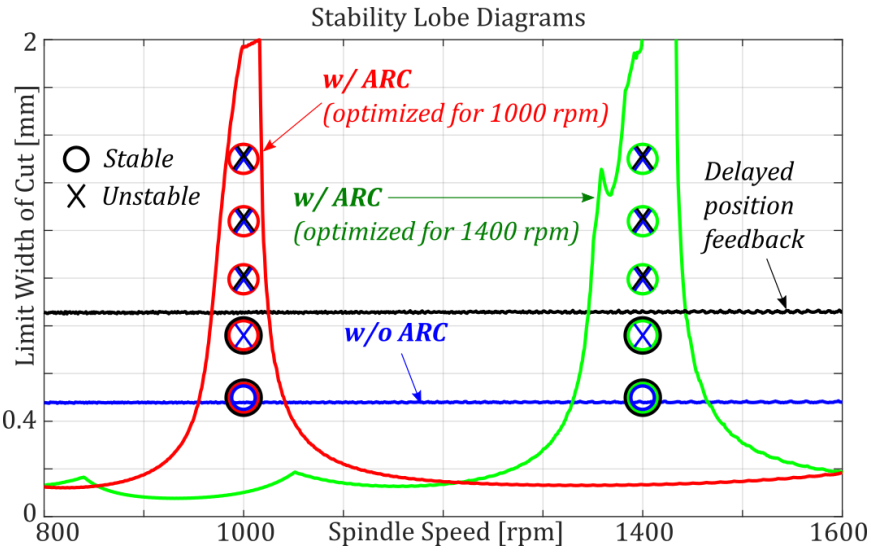

Figure 29. Chatter stability lobe (SLD) shaping by proposed technique.

5.5. Conclusions

The objective of this paper was to design a controller to exceed bandwidth limitation of conventional feed drive systems in actively controlling high frequency chatter vibrations. Regenerative chatter vibrations occurring at 2.66[kHz] are attenuated by a feed drive system that has <1[kHz] closed-loop bandwidth (2.5× lower). Stability lobes are shaped to realize 4× higher MRR in a desired cutting speed range. Proposed compensator can be used jointly with an existing servo control to utilize machine tool feed drives for active high frequency chatter control. Or, it can be implemented stand-alone on an active damper system such as in inertial actuators [80], [74], [23], [75], [76], [77], which broadens its impact for various machine tools and use scenarios. Implementation in other chatter-experiencing machining processes remains to be a future research topic.

5.6. Acknowledgement

Authors gratefully thank University of British Columbia (UBC)’s Manufacturing Automation Laboratories (MAL) for assisting with the experimental setup, and NSF (Award No: 1661926) for partially funding this research.

ACTIVE CHATTER MITIGATION BY OPTIMAL CONTROL OF REGENERATIVE MACHINING PROCESS DYNAMICS

Alper Dumanli and Burak Sencer

IEEE/ASME Transactions on Mechatronics
Submitted in March 2021, Under Review

6. Active Chatter Mitigation by Optimal Control of Regenerative Machining Process Dynamics

Chatter vibrations are a type of self-exited vibrations observed in many subtractive manufacturing processes. They limit achievable material remove rate (MRR), reduce tool life, result in poor surface finish, and even damage the manufacturing equipment. This paper proposes a novel control system design for machine tool feed drives, which modulates cutting tool motion based on the in-process vibration measurements to mitigate chatter vibrations. Proposed approach has two key contributions. Firstly, as opposed to introducing modal damping to the structure, proposed approach stabilizes machining process dynamics by controlling its governing delay differential equation (DDE). H∞ control framework is used to design the controller and ensure robust process stability. The controller design problem is postulated as a convex optimization problem with linear matrix inequalities (LMIs), which is solved to global optimality. Secondly, proposed controller is implemented as an add-on compensator that works jointly with an existing servo motion control system to realize both positioning and chatter vibration control. Experimental validations are conducted on a lathe equipped with a fast tool servo (FTS) actuator. It is shown that regenerative chatter vibrations in orthogonal turning process can be suppressed robustly and up to 5× increase in MRR (productivity) can be achieved.

6.1. Introduction

Attaining greater material removal rates (MRRs) is utmost important for subtractive manufacturing processes [71]. Higher MRR leads to greater productivity and throughput. Nevertheless, productivity of subtractive manufacturing processes is affected by various forms of unwanted vibrations. For example, trajectory-induced residual vibrations occur during high-speed machining when feed drives of the manufacturing equipment undergo rapid acceleration. Such residual vibrations are widely observed in high-speed machinery, 3D printer systems and industrial robots [82]. Forced vibrations occur due to disturbance process (cutting) forces acting on the flexible machine structure and may destroy the surface finish or violate part tolerances.

Finally, self-excited chatter vibrations occur due to forced vibrations and the regeneration effect that is induced by the rotating kinematics of the machining process. Once chatter vibrations are triggered, machining processes become unstable, leading to excessive oscillations of the machine tool/workpiece structure that causes rapid tool breakage and feed drive system failure. The overreaching goal in most machining processes is to eliminate such destructive "chatter vibrations" through process planning [83] or more recently mechatronic hardware or control techniques [75], [77], [74]. This paper presents a novel control system design, which allows machine's own feed drives (positioning) systems to actively control and stabilize chatter vibrations towards attaining higher MRR and productivity.

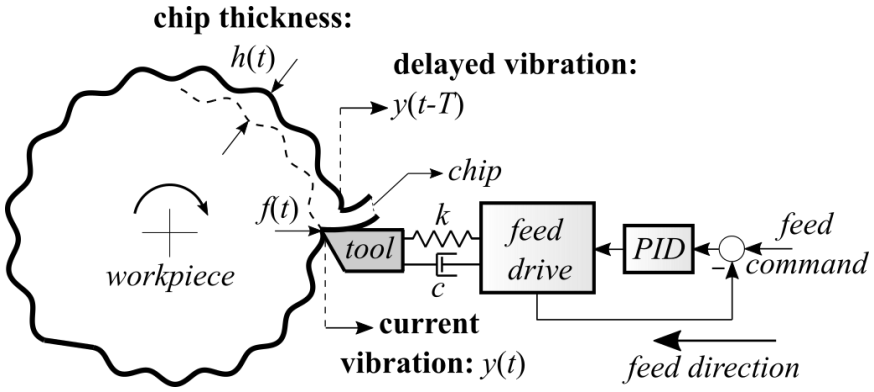

Figure 30. Illustration of chatter vibrations in orthogonal turning process.

Before discussing relevant state-of-the-art mechatronics-driven chatter vibration mitigation approaches, dynamics of orthogonal cutting and regenerative chatter vibrations are briefly introduced. Figure 30 illustrates dynamics of an orthogonal machining process, e.g. turning. A flexible tooling system is fed to a rotating workpiece to remove material from its surface. In such operation, feed (cutting) forces $f(t)$ are proportional to the thickness $h(t)$ and the width a of the material (chip) that is removed in each spindle (workpiece) revolution. Tool tip vibrates ($y(t)$) due to its structural dynamics $G(s)$ and the disturbance cutting forces. Dynamic cutting forces (f) and chip thickness (h) can be represented in Laplace (s) domain as:

$$f(s) = K_F a h(s), \text{ where: } h(s) = h_0 - \left[y(s) - e^{-sT} y(s) \right] \tag{6.1}$$

where K_F is the cutting force coefficient and h_0 is the indented or desired chip thickness.

Actual chip thickness $h(s)$ is varying due to difference between current tool vibration $y(s)$ and the one experienced in previous spindle revolution $y(s)e^{-sT}$, and thus the dynamically varying portion of the chip thickness becomes $y(s)(1-e^{-sT})$ with delay T being the spindle revolution period. Noting that cutting forces in (6.1) generate tool vibrations by $y(s)=G(s)f(s)$, and hence the well-known orthogonal machining process dynamics can be postulated as:

$$y(s) = K_F a G(s)\left[h_0 - \left(1 - e^{-sT} y(s)\right)\right] \tag{6.2}$$

Equation (6.2) is a delay differential equation (DDE), and its order is determined by the structural dynamics of the tooling $G(s)=y(s)/f(s)$, which is also the disturbance transfer function (TF) of the feed drive system (see Figure 30).

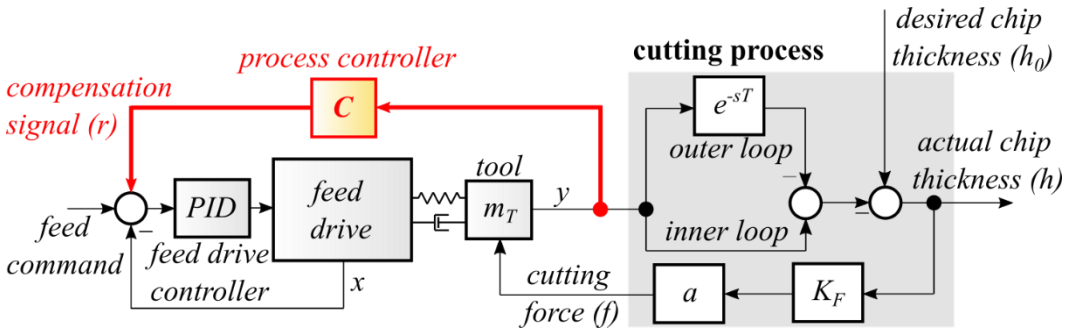

Figure 31. Block diagram of proposed chatter suppression strategy.

Tools such as Nyquist (frequency domain) [19] or semi-discrete time domain analysis [84] can be used to test machining process stability for any given $G(s)$, delay period T, and the width of cut, a. In manufacturing literature, the goal is to realize wider cuts at any cutting speed, and stability of (6.2) is analyzed for a range of spindle speeds (delay period) $n=60/T$ to determine the maximum attainable (limit) width of cut, a_{lim}. When a_{lim} is plotted against n, it is called the Stability Lobe Diagram (SLD), which shows the stability border of the machining process. Figure 32.a (see below) shows a typical SLD, which indicates that as long as the width of cut, a is selected below the borderline $a_{lim}(n)$, the process is stable.

Mechatronics and manufacturing communities have been focusing on improving stability of this regenerative process dynamics to attain higher MRRs [16], [75], [85], [22]. It is well-known that introducing damping into $G(s)$ improves stability [75]. Thus,

the most common approach has been to introduce damping through use of hardware systems. For instance, tuned-mass-dampers (TMDs) can effectively introduce modal damping [22]. Typical TMDs are passive solutions, and they fail if resonances in the structure shift, which very often happens on larger manufacturing equipment or when processing larger workpieces [86]. To increase their robustness, semi-active systems are designed [87]. Note that all such systems are "add-on" mechatronic components that are attached on the machine and may not fit onto smaller, more compact manufacturing equipment, or are simply too costly.

Another strategy is to use control schemes to either robustify TMDs or use a dedicated inertial actuator system to inject modal damping to the structure in a fully active manner. Such systems typically use accelerometer feedback [77] or make use of velocity signals [74] to realize modal damping. Examples of inertial actuators applied on various equipment can be found in the literature [16]. However, their practical performance is limited. The limitation originates mainly from the fact that the machine structure suffers from various structural modes, and when damping of one structural resonance is achieved by feedback control, other higher frequency modes may be destabilized. The fundamental limitation of Bode's Integral Theorem (waterbed effect) applies [88]. It should be noted that such modal damping approach can also be realized by the existing drives of the machine tool structure [85]. In this case, feed drives of the machine jointly undertake position control while at the same time try to dampen any observable and controllable resonant modes [5]. Such approach is cost effective since it eliminates the need for an additional actuator; however, it can only dampen low frequency modes due to its limited bandwidth and its tendency to destabilize higher frequencies.

As discussed, injecting damping into structural dynamics has been the dominant approach [75]. This is mainly due to the fact that stabilizing the original DDE in (6.2) with its inherent delays is a challenge for control design. Sophisticated state-space based methods are proposed, where transport delays are addressed with Padé approximation, and H∞ controllers are proposed [16,17]. However, these methods require significantly high-order controllers to accurately capture the delay effect. Control design suffers from numerical inaccuracy and these approaches fail to robustly

demonstrate greater improvement [78], [90].

This paper proposes a novel chatter mitigation strategy. The idea is to design an optimal process controller that utilizes existing feed drive axes of the machine to stabilize the process dynamics including its inherent delays. Proposed control architecture is illustrated in Figure 31. As shown, $C(s)$ is the process controller, which injects a compensation signal to stabilize the process dynamics. The novelty in the design of $C(s)$ comes from that fact that instead of approximating delays of (6.2), a delay-based Lyapunov function is utilized, which allows us to design a stable controller directly without any approximation. The controller design problem is postulated as a convex optimization problem with Linear Matrix Inequalities (LMIs). As a result, a lower order controller is designed, which works with existing positioning controller of the feed drive system to realize both low frequency positioning and high frequency process control. The design procedure is delay-independent, which means that once the controller is designed, it can be implemented for any spindle speed (n). The paper is organized as follows. Section II introduces the modeling strategy. Section III proposes the controller design methodology. Finally, Section IV presents implementation and experimental validation.

6.2. Modeling of Machining Process Dynamics

6.2.1. Open Loop Dynamics

The DDE of the machining process in (6.1) can be put in a transfer function (TF) form as:

$$P(s)=\frac{y(s)}{h_0(s)}=\frac{K_F a G(s)}{1+aK_F G(s)\left(1-e^{-sT}\right)}=\frac{K_F a G(s)}{1+aL_P(s)} \tag{6.3}$$

where $G(s)$ can be identified in the form of

$$G(s)=g_S\prod_{i=1}^{L}\left(\frac{s^2+2\zeta_{Z,i}\omega_{Z,i}s+\omega_{Z,i}^2}{s^2+2\zeta_{N,i}\omega_{N,i}s+\omega_{N,i}^2}\right)\left(\frac{\omega_{N,i}^2}{\omega_{Z,i}^2}\right) \tag{6.4}$$

where L is the number of flexible modes. $\omega_{N,i}$, $\zeta_{N,i}$, $\omega_{Z,i}$ and $\zeta_{Z,i}$ are the natural frequencies and damping ratios of the i^{th} resonance and anti-resonance, respectively. g_S

is the static gain of G.

The $L_P(s)=K_F G(s)(1-e^{-sT})$ term in the denominator of (6.3) is denoted as the *process loop transmission* dynamics with "a" (width of cut) being the process gain. Figure 32.b shows the frequency response of $L_P(s)$ for a delay period T. As shown, it follows the trend of $K_F G(s)$, but the delay term $(1-e^{-sT})$ adds severe magnitude and phase ripples, which decreases gain margin of the process. The minimum gain margin determines the limit width of cut a_{lim} allowed for a stable process. Figure 32.a simply plots this minimum gain margin in the form of an SLD and depicts stability border of the DDE in (6.2). Workpieces with a width of cut smaller than a_{lim}, i.e. $a<a_{lim}$, can be machined in a stable manner without chatter, but widths of cut larger than $a>a_{lim}$ will cause instability.

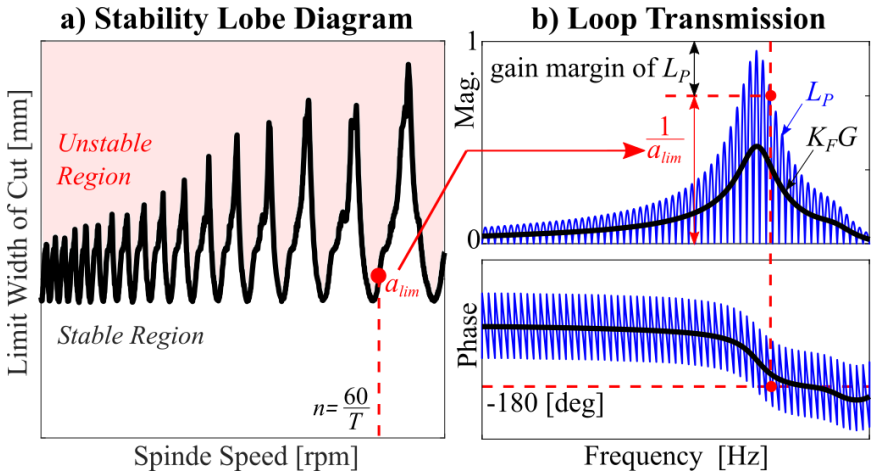

Figure 32. (a) Example Stability Lobes Diagram (SLD), and (b) loop transmission frequency response function of turning process.

6.2.2. Closed Loop Dynamics

The objective is to improve stability margins of the process dynamics by shaping the process loop transmission, L_P in (6.3). This is achieved by injecting an additional reference (compensation) signal $r(s)$ to the feed-drive controller actively during the machining process, based on vibration measurements taken from the tool tip (see Figure 31). Considering $r(s)$, governing dynamics of the process is rewritten from (6.3) as:

$$y = Gf + T_T \underset{r}{Cy} \rightarrow y = K_F aG\left[h_0 - y\left(1 - e^{-sT}\right)\right] + T_T Cy \tag{6.5}$$

where T_T=y/r is the tool tip position tracking dynamics (see Figure 31), which is controlled by a low-bandwidth PID controller [82]. C is the proposed controller TF, which receives tool displacement feedback (y) and generates compensation signal (r). The *controlled process loop dynamics* (P_C) is defined as:

$$P_C = \frac{y}{h_0} = \frac{K_F aG}{1 + K_F aG\left(1 - e^{-sT}\right) - CT_T} \tag{6.6}$$

Notice that in (6.6), the proposed controller C modifies the process loop transmission additively rather than multiplicatively. This makes the control design problem challenging. To retain controllability of P_C, characteristic equation of (6.6) is re-arranged as follows.

Characteristic equation of P_C is:

$$1 + K_F aG\left(1 - e^{-sT}\right) - CT_T = 0 \tag{6.7}$$

where roots of (6.7) determine stability of the controlled process, and therefore C should be designed such that all the roots of (6.7) are on the left half side of the complex plane (LHP). To realize that, (6.7) is algebraically modified without changing its roots as:

$$1 + C\underbrace{\left(\frac{-T_T}{1 + K_F aG\left(1 - e^{-sT}\right)}\right)}_{H} = 0 \tag{6.8}$$

Notice that in (6.8), C and H are multiplied, which enables us to utilize modern control design frameworks for designing C to stabilize H as outlined in the following section.

6.3. Optimal Process Controller Design

6.3.1. Design of the State Feedback Control Law

The objective of the proposed controller C is to ensure that roots of characteristic equation (6.8) are placed robustly on the LHP. Notice that H in (6.8) contains T_T=y/r, which denotes effect of slow feed-drive tracking dynamics. To help decouple the

process control design from feed-drive dynamics, inverse of the position tracking dynamics T_T^{-1} is included in C. T_T^{-1} can be estimated in a stable manner as:

$$T_T^{-1}(s) = \frac{T_{T,P}(s)}{T_{T,NZ}(0)T_{T,MZ}(s)} \tag{6.9}$$

where $T_{T,P}$ is the denominator of T_T, $T_{T,MZ}$ and $T_{T,NZ}$ are minimum and nonminimum-phase zeros of T_T respectively. $T_{T,NZ}(0)$ denotes the DC gain (~0 [Hz]) of the nonminimum-phase zeros.

Next, C is augmented by a state-feedback controller K as:

$$C = KT_T^{-1}, \quad G_V = \underbrace{\left(\frac{-T_T}{1+K_F aG\left(1-e^{-sT}\right)}\right)}_{H} T_T^{-1} \tag{6.10}$$

where G_V is called the "virtual open loop TF". Notice that, roots of $1+KG_V = 1+CH=0$ are identical to the poles of P_C, and thus stabilizing G_V with K ensures the stability of P_C. K is designed in state space form as described in the following.

The objective of K is to robustly stabilize roots of (6.8) by controlling the virtual open loop TF, G_V. Notice that G_V contains internal delay dynamics in its denominator (e^{-sT}), and thus it may have infinitely many roots [91]. For this reason, typical pole placement techniques [5] are not suitable for designing K. Frequency domain controller design techniques such as loop shaping are also challenging. This is because internal delays might make virtual open loop (G_V) unstable, and internal-delay-induced instability is difficult to test and control using frequency domain tools such as Nyquist-based design. To circumvent these limitations, K is designed utilizing H∞-norm minimization, where closed loop Lyapunov stability is guaranteed by taking internal delays into consideration.

Stable inversion of T_T is implemented as given by (6.9), and G_V is discretized as:

$$G_V = \frac{-T_T^{-1}T_T}{1+K_F aG\left(1-e^{-sT}\right)} \rightarrow G_V = \frac{-z^{-M}}{1+K_F aG_d\left(1-z^{-T/T_s}\right)} \tag{6.11}$$

where $\hat{T}_T^{-1}T_T$ in (6.11) is replaced by z^{-M} to represent the remaining delays induced by excluded non-minimum phase zeros and unmodeled dynamics. This helps reduce the

order of G_V and simplify controller design. In (6.11), T_s is the sampling time and G_d is the discrete-time equivalent of G:

$$G_d = \frac{\beta_1 z^{-1} + \cdots + \beta_{L-1} z^{-L+1}}{1 + \alpha_1 z^{-1} + \cdots + \alpha_L z^{-L}} \tag{6.12}$$

$\tilde{G}_V$ is then represented in discrete-time state space form as:

$$\begin{aligned}
&\mathbf{q}_{m+1} = \mathbf{A}\mathbf{q}_m + \mathbf{A}_D\mathbf{q}_{m-\tau} + \mathbf{B}r_m + \mathbf{B}w_m \\
&y_m = \mathbf{C}\mathbf{q}_m \\
&\text{where:} \\
&\mathbf{A} = \begin{bmatrix} \mathbf{0}_{(M-1)\times 1} & \mathbf{I}_{(M-1)\times(M-1)} & \mathbf{0}_{(M-1)\times L} \\ \mathbf{0}_{L\times 1} & \mathbf{0}_{L\times(M-1)} & \mathbf{I}_{L\times L} \\ 0 & \mathbf{0}_{1\times(M-1)} & \boldsymbol{\alpha}_{1\times L} \end{bmatrix} \\
&\boldsymbol{\alpha} = -\begin{bmatrix} \alpha_L & \left(\alpha_{L-1} + K_F a \beta_{L-1}\right) & \cdots & \left(\alpha_1 + K_F a \beta_1\right) \end{bmatrix} \\
&\mathbf{A}_D = \begin{bmatrix} \mathbf{0}_{M\times M} & \mathbf{0}_{M\times L} \\ \mathbf{0}_{L\times M} & \boldsymbol{\beta}_{L\times L} \end{bmatrix}, \quad \boldsymbol{\beta} = \begin{bmatrix} 0 & \cdots & \cdots & 0 \\ \vdots & \ddots & \ddots & \vdots \\ 0 & \cdots & \cdots & 0 \\ 0 & K_F a \beta_{L-1} & \cdots & K_F a \beta_1 \end{bmatrix} \\
&\mathbf{B} = \begin{bmatrix} \mathbf{0}_{1\times(M+L-1)} & 1 \end{bmatrix}^T, \quad \mathbf{C} = \begin{bmatrix} \alpha_L & \cdots & \alpha_1 & 1 & \mathbf{0}_{1\times(M-1)} \end{bmatrix}
\end{aligned} \tag{6.13}$$

with $\mathbf{q}_{(M+L)\times 1}$ being its internal states and m is the sample counter. w_m is the disturbance input, which represents unmodeled dynamics and modeling errors. r_m is the compensation signal shown in Figure 31, and y_m is the current tool displacement. Notice that the delayed internal state $\mathbf{q}_{m-\tau}$ appears in (6.13) with $\tau = T/T_s$. Therefore, $\tilde{G}_V$ in (6.11) is still a DDE.

If $\mathbf{q}$ is measured, $\tilde{G}_V$ can be stabilized by the following state feedback law:

$$r_m = \mathbf{K}\mathbf{q}_m \tag{6.14}$$

where $\mathbf{K}_{1\times(M+L)}$ is the state-feedback gain vector. $\mathbf{K}$ is designed by solving the following H∞-norm optimization problem to minimize sensitivity (S) of process dynamics:

$$\begin{aligned}
&\min_{\mathbf{K}} \|S\|_\infty, \text{ subject to: } S \text{ is stable} \\
&\text{with: } S = \frac{1}{1 + KG_V} = 1 + \mathbf{K}\left(z\mathbf{I} - \mathbf{A} - \mathbf{A}_D z^{-\tau} - \mathbf{B}\mathbf{K}\right)^{-1}\mathbf{B}
\end{aligned} \tag{6.15}$$

Notice that (6.15) is a typical H∞ controller design problem augmented by internal delays. It is first converted into a convex optimization problem with the use of Linear

Matrix Inequalities (LMI) [92] as described in the following, and then solved numerically using semidefinite programming tools [55].

Firstly, to stabilize the system, (6.15) is converted into an LMI by defining a Lyapunov function candidate [92] for S as:

$$V\left(\mathbf{q}_m\right)=V_m=\mathbf{q}_m^T\mathbf{P}\mathbf{q}_m+\sum_{i=m-\tau}^{m}\mathbf{q}_i^T\mathbf{R}_1\mathbf{q}_i+\sum_{i=m-\tau}^{m}\mathbf{q}_i^T\mathbf{K}^T R_2\mathbf{K}\mathbf{q}_i \tag{6.16}$$

The candidate in (6.16) consists of three terms. The first term, $\mathbf{q}_m{}^T\mathbf{P}\mathbf{q}_m$, is a typical energy-like quadratic function found in typical Lyapunov functions used for linear systems [93]. The second and third terms are introduced to penalize cumulative energy of the internal state $\mathbf{q}_m$ and the compensation signal $r_m=\mathbf{K}\mathbf{q}_m$ within one delay period τ. If V is positive ($V>0$) and monotonically decreasing ($\Delta V<0$) for all values of $\mathbf{q}_m$, then the closed loop system is ensured to be stable. These stability conditions can be summarized as follows:

$$\Delta V_m=V_{m+1}-V_m<0,\ \ \mathbf{P}\succ\mathbf{0},\ \ \mathbf{R}_1\succ\mathbf{0}\ \text{ and }\ R_2>0 \tag{6.17}$$

where "$\succ\mathbf{0}$" indicates *positive definiteness*, and Δ is the *difference* operator. $\Delta V_m<0$ condition in (6.17) can be expanded as:

$$\Delta V_m=\begin{bmatrix}\mathbf{q}_m\\ \mathbf{q}_{m-\tau}\\ \mathbf{K}\mathbf{q}_{m-\tau}\end{bmatrix}^T\underbrace{\begin{bmatrix}\mathbf{\Phi}_{11} & \mathbf{\Phi}_{12} & \mathbf{0}\\ * & \mathbf{\Phi}_{22} & \mathbf{0}\\ * & * & -R_2\end{bmatrix}}_{\mathbf{\Phi}}\begin{bmatrix}\mathbf{q}_m\\ \mathbf{q}_{m-\tau}\\ \mathbf{K}\mathbf{q}_{m-\tau}\end{bmatrix}<0$$

where:

$$\begin{aligned}\mathbf{\Phi}_{11}&=\left(\mathbf{A}+\mathbf{B}\mathbf{K}\right)^T\mathbf{P}\left(\mathbf{A}+\mathbf{B}\mathbf{K}\right)-\mathbf{P}+\mathbf{R}_1+\mathbf{K}R_2\mathbf{K}^T\\ \mathbf{\Phi}_{12}&=\left(\mathbf{A}+\mathbf{B}\mathbf{K}\right)^T\mathbf{P}\mathbf{A}_D\\ \mathbf{\Phi}_{22}&=-\mathbf{R}_1+\mathbf{A}_D^T\mathbf{P}\mathbf{A}_D\end{aligned} \tag{6.18}$$

Notice that (6.18) is satisfied if and only if the symmetric matrix $\mathbf{\Phi}$ is negative definite, i.e. $\mathbf{\Phi}\prec\mathbf{0}$. With the help of $\mathbf{\Phi}$, the Lyapunov stability conditions in (6.17) are revised as:

$$\mathbf{\Phi}\prec\mathbf{0},\ \ \mathbf{P}\succ\mathbf{0},\ \ \mathbf{R}_1\succ\mathbf{0}\ \text{ and }\ R_2>0 \tag{6.19}$$

Next, utilizing the stability conditions given in (6.19), the optimization problem given in (6.15) is converted into a convex optimization problem with LMIs as:

$$\min_{(\mathbf{M},\ \mathbf{Q},\ \mathbf{S}_1,\ S_2)} \|\gamma\|_2^2$$

subject to:

$\mathbf{H} \prec \mathbf{0},\ \mathbf{Q} \succ \mathbf{0},\ \mathbf{S}_1 \succ \mathbf{0},\ S_2 > 0$ and $\gamma > 0$

with:

$$\mathbf{H} = \begin{bmatrix} \left(-\mathbf{Q} + \mathbf{A}_D \mathbf{S}_1 \mathbf{A}_D^T\right) & \left(\mathbf{AQ} + \mathbf{BM}\right) & \mathbf{B} & \mathbf{0} & \mathbf{0} & \mathbf{0} \\ * & -\mathbf{Q} & \mathbf{0} & \mathbf{M}^T & \mathbf{M}^T & \mathbf{Q} \\ * & * & -\gamma & \mathbf{I} & \mathbf{0} & \mathbf{0} \\ * & * & * & \mathbf{I} & \mathbf{0} & \mathbf{0} \\ * & * & * & * & -S_2 & \mathbf{0} \\ * & * & * & * & * & -\mathbf{S}_1 \end{bmatrix}$$

$$\mathbf{K} = \mathbf{M}\mathbf{Q}^{-1},\ \mathbf{Q} = \mathbf{P}^{-1},\ \mathbf{S}_1 = \mathbf{R}_1^{-1} \text{ and } S_2 = 1/R_2 \tag{6.20}$$

where $\sqrt{\gamma}$ is the upper bound of the H∞-norm of S ($\|S\|_\infty$), and $\mathbf{H}$ is symmetric. The proof of equivalence of (6.15) and (6.20) is provided in appendix. Equation (6.20) can be solved conveniently using available semidefinite programming tools [55], [48] to obtain the feedback gain vector $\mathbf{K}$.

In order to implement the state feedback control law given in (6.14), internal states $\mathbf{q}$ need to be accessed. In practice, only tool kinematics, e.g. acceleration/displacement, can be measured on a physical system, and thus $\mathbf{q}$ needs to be observed. The following describes the design of an observer to achieve this.

6.3.2. Design of the Delayed State Observer

In this section, a state observer algorithm is presented to estimate the internal states of (6.13), $\mathbf{q}$. A Luenberger observer structure [94] is utilized, which includes the internal delay in $\mathbf{q}$:

$$\begin{aligned} \mathbf{q}_{m+1}^{(e)} &= \hat{\mathbf{A}}\mathbf{q}_m^{(e)} + \hat{\mathbf{A}}_D\mathbf{q}_{m-\tau}^{(e)} + \hat{\mathbf{B}}r_m + \boldsymbol{\lambda}\hat{\mathbf{C}}\mathbf{q}_m^{(e)} - \boldsymbol{\lambda}y_m \\ y_m^{(e)} &= \hat{\mathbf{C}}\mathbf{q}_m^{(e)} \end{aligned} \tag{6.21}$$

and the overall closed loop process dynamics can be written in state space form from (6.13) as:

$$\begin{aligned}\begin{bmatrix}\mathbf{q}_{m+1}\\ \mathbf{q}_{m+1}^{(e)}\end{bmatrix}&=\begin{bmatrix}\mathbf{A} & \mathbf{BK}\\ -\mathbf{C}\boldsymbol{\lambda} & \left(\hat{\mathbf{A}}+\hat{\mathbf{B}}\mathbf{K}+\boldsymbol{\lambda}\hat{\mathbf{C}}\right)\end{bmatrix}\begin{bmatrix}\mathbf{q}_m\\ \mathbf{q}_m^{(e)}\end{bmatrix}\\&\quad+\begin{bmatrix}\mathbf{A}_D & \mathbf{0}\\ \mathbf{0} & \hat{\mathbf{A}}_D\end{bmatrix}\begin{bmatrix}\mathbf{q}_{m-\tau}\\ \mathbf{q}_{m-\tau}^{(e)}\end{bmatrix}+\begin{bmatrix}\mathbf{B}\\ \mathbf{0}\end{bmatrix}w_m\\ \begin{bmatrix}y_m\\ y_m^{(e)}\end{bmatrix}&=\begin{bmatrix}\mathbf{C} & \mathbf{0}\\ \mathbf{0} & \hat{\mathbf{C}}\end{bmatrix}\begin{bmatrix}\mathbf{q}_m\\ \mathbf{q}_m^{(e)}\end{bmatrix}\end{aligned}\tag{6.22}$$

where $\mathbf{q}_m^{(e)}$ is the estimated internal state, and $y_m^{(e)}$ is the estimated tool displacement. $\hat{\mathbf{A}}$, $\hat{\mathbf{B}}$ and $\hat{\mathbf{C}}$ are the modeled (identified) state space matrices of the process ($\tilde{G}_V$), and $\boldsymbol{\lambda}$ is the $(M+L)\times 1$ observer gain vector. Assuming $\hat{\mathbf{A}}\cong\mathbf{A}$, $\hat{\mathbf{B}}\cong\mathbf{B}$ and $\hat{\mathbf{C}}\cong\mathbf{C}$, state estimation error ($\tilde{\mathbf{q}}_m$) dynamics can be written as:

$$\begin{aligned}\tilde{\mathbf{q}}_{m+1}&=\mathbf{A}\tilde{\mathbf{q}}_m+\mathbf{A}_D\tilde{\mathbf{q}}_{m-\tau}+\boldsymbol{\lambda}\mathbf{C}\tilde{\mathbf{q}}_m+\mathbf{B}w_m\\ \tilde{\mathbf{q}}_m&=\mathbf{q}_m-\mathbf{q}_m^{(e)}\\ \tilde{y}_m&=\mathbf{C}\tilde{\mathbf{q}}_m\end{aligned}\tag{6.23}$$

where $\tilde{y}_m$ is the output estimation error, i.e. $\tilde{y}_m=y_m-y_m^{(e)}$. Observer gain $\boldsymbol{\lambda}$ needs to be designed to guarantee robust and stable estimation of the internal state so that the state feedback controller $\mathbf{K}$ can be implemented (see (6.14)). To achieve this, $\boldsymbol{\lambda}$ is designed by minimizing the disturbance response (D) of estimation error dynamics given by (6.23) from w_m to $\tilde{y}_m$ as:

$$\begin{aligned}&\min_{\boldsymbol{\lambda}}\left\|D\right\|_\infty,\ \text{subject to: } D \text{ is stable}\\ &\text{with: } D=\frac{\tilde{y}(z)}{w(z)}=\mathbf{C}\left(z\mathbf{I}-\mathbf{A}-\mathbf{A}_Dz^{-\tau}-\boldsymbol{\lambda}\mathbf{C}\right)^{-1}\mathbf{B}\end{aligned}\tag{6.24}$$

Similar to (6.15), (6.24) is an H∞-norm minimization problem. By making use of the following identity

$$\begin{aligned}D&=\mathbf{C}\left(z\mathbf{I}-\mathbf{A}-\mathbf{A}_Dz^{-\tau}-\boldsymbol{\lambda}\mathbf{C}\right)^{-1}\mathbf{B}\\&=\mathbf{B}^T\left(z\mathbf{I}-\mathbf{A}^T-\mathbf{A}_D^Tz^{-\tau}-\mathbf{C}^T\boldsymbol{\lambda}^T\right)^{-1}\mathbf{C}^T\end{aligned}\tag{6.25}$$

(6.24) can be converted into a convex optimization problem as:

$$\min_{(\boldsymbol{\mu},\,\boldsymbol{\Theta},\,\boldsymbol{\Sigma}_1,\,\Sigma_2)} \|\eta\|_2^2$$

subject to:

$$\boldsymbol{\Gamma} \prec \mathbf{0},\ \boldsymbol{\Theta} \succ \mathbf{0},\ \boldsymbol{\Sigma}_1 \succ \mathbf{0},\ \Sigma_2 > 0 \text{ and } \eta > 0$$

with:

$$\boldsymbol{\Gamma} = \begin{bmatrix} \left(-\boldsymbol{\Theta} + \mathbf{A}_D^T \boldsymbol{\Sigma}_1 \mathbf{A}_D\right) & \left(\mathbf{A}^T\boldsymbol{\Theta} + \mathbf{C}^T\boldsymbol{\mu}\right) & \mathbf{C}^T & \mathbf{0} & \mathbf{0} & \mathbf{0} \\ * & -\boldsymbol{\Theta} & \mathbf{0} & \boldsymbol{\Theta}\mathbf{B} & \boldsymbol{\mu}^T & \boldsymbol{\Theta} \\ * & * & -\eta & \mathbf{0} & \mathbf{0} & \mathbf{0} \\ * & * & * & \mathbf{I} & \mathbf{0} & \mathbf{0} \\ * & * & * & * & -\Sigma_2 & \mathbf{0} \\ * & * & * & * & * & -\boldsymbol{\Sigma}_1 \end{bmatrix}$$

$$\boldsymbol{\lambda} = \boldsymbol{\mu}\boldsymbol{\Theta}^{-1} \tag{6.26}$$

where $\sqrt{\eta}$ is the upper bound of the H∞-norm of D ($\|D\|_\infty$), and $\boldsymbol{\Gamma}$ is symmetric. Equivalence of (6.24) and (6.26) can be proven by following the same steps used for converting (6.15) to (6.20), as shown in the appendix.

Similar to (6.20), (6.26) can be solved using semidefinite programming tools [55], [48] to obtain the observer gain, $\boldsymbol{\lambda}$. The controller dynamics (K) from the tool displacement measurement input (y) to the compensation signal output (r) including state feedback and observer dynamics then becomes:

$$\begin{aligned} \mathbf{q}_{m+1}^{(e)} &= \hat{\mathbf{A}}\mathbf{q}_m^{(e)} + \hat{\mathbf{A}}_D\mathbf{q}_{m-\tau}^{(e)} + \hat{\mathbf{B}}\mathbf{K}\mathbf{q}_m^{(e)} + \boldsymbol{\lambda}\hat{\mathbf{C}}\mathbf{q}_m^{(e)} - \boldsymbol{\lambda} y_m \\ r_m &= \mathbf{K}\mathbf{q}_m^{(e)} \end{aligned} \tag{6.27}$$

and presented in TF form in z-domain as:

$$K = -\mathbf{K}\left(z\mathbf{I} - \hat{\mathbf{A}} - \hat{\mathbf{A}}_D z^{-\tau} - \hat{\mathbf{B}}\mathbf{K} - \boldsymbol{\lambda}\hat{\mathbf{C}}\right)^{-1}\boldsymbol{\lambda} \tag{6.28}$$

Once K is constructed as shown in (6.28), overall process controller can be implemented as $C=K\hat{T}_T^{-1}$ (see (6.10)).

6.4. Experimental Setup and Implementation

Proposed chatter suppression strategy is validated on an industrial turning center (lathe) equipped with a piezo actuated FTS shown in Figure 33.a. Cylindrical Al6061 workpieces are machined with a carbide insert, resulting in a cutting coefficient of

K_F=1336 [N/mm^2]. Tool accelerations are measured using a Dytran 3035B1G accelerometer with a 10 [mV/g] sensitivity.

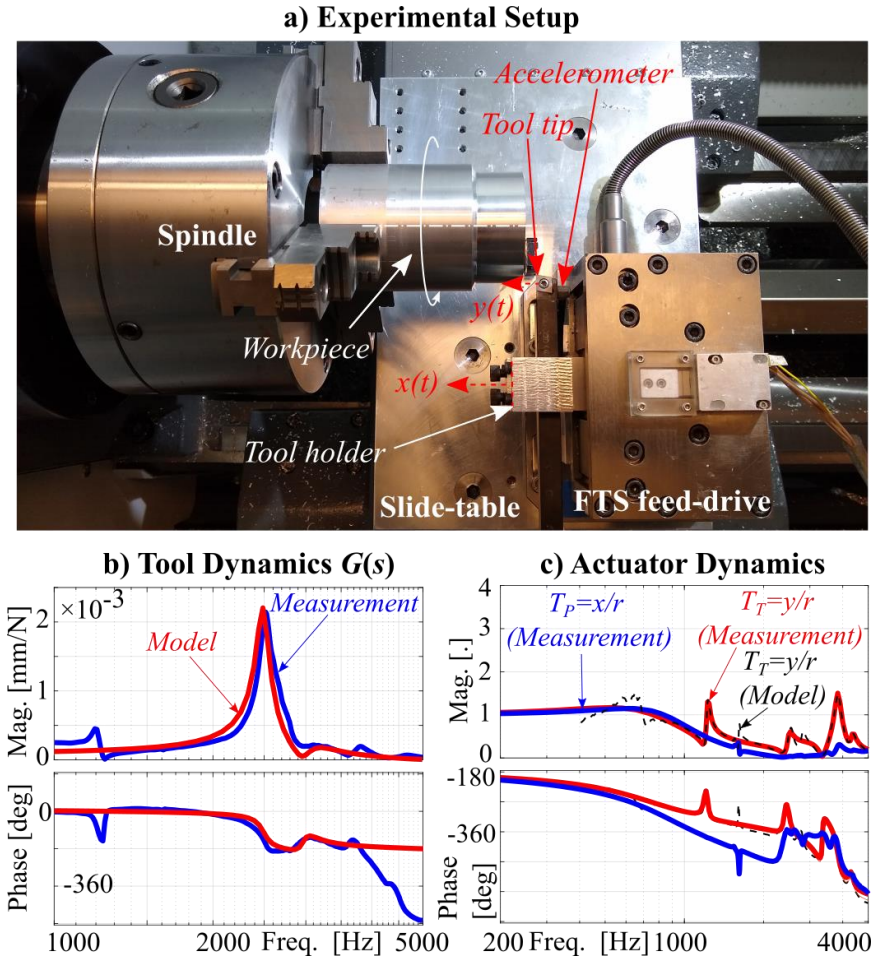

Figure 33. Experimental setup and its frequency response.

Dynamics of the tool assembly ($G=y/f$) is measured by impact testing, and $\hat{G}$ is fitted according to (6.4) with an order of L=5. Figure 33.b depicts the identification accuracy. Note that dominant resonant modes of G (~2.5[kHz] and ~3.2[kHz]) are captured by the model. These two modes are critical in destabilizing the machining process and cause chatter vibrations. The mode at ~1.2[kHz] is omitted in $\hat{G}$ to avoid increasing the degree of the system. This can be justified since that mode has a relatively larger dynamic stiffness and should not be the primary cause of instability.

As shown in Figure 33.a, cutting tool is fed to the workpiece by a piezo-actuated FTS system. Details of the FTS is given in [95]. Its position tracking dynamics $T_P=x/r$ is shown in Figure 33.c. Actuator position x is controlled by a PID controller with a

tracking bandwidth (f_{BW}) of ~1[kHz] (see Figure 33.c). Tool tip tracking transfer function T_T, from r to the tool-tip displacement y follows the response of T_P for $f<f_{BW}$ and exhibits magnitude peaks in the vicinity of the structural modes of G at 1.2[kHz], 2.5[kHz] and 3.2[kHz]. Thus, T_T is modeled by a 12th order TF as shown in Figure 33.c.

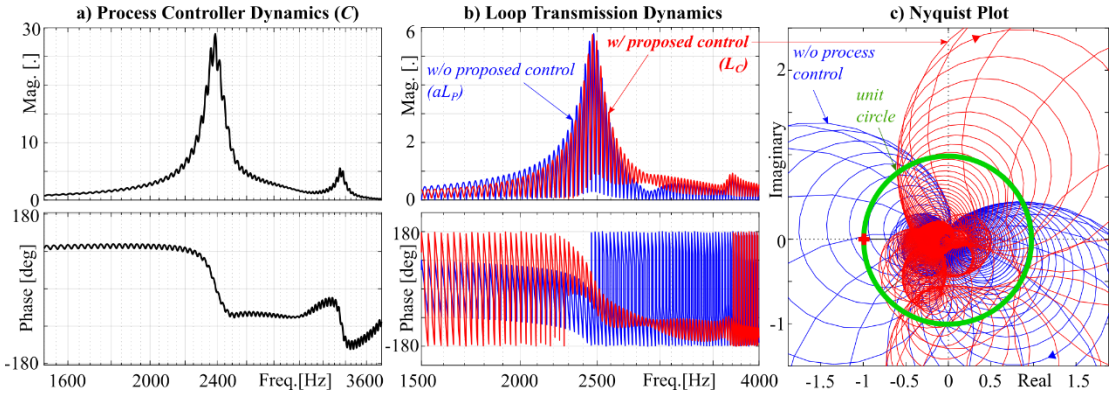

Figure 34. Controller and process loop transmission dynamics.

In order to implement the controller given by (6.27), tool displacement y is acquired by integrating and high pass filtering the acceleration signal:

$$\hat{y} = \left(\frac{T_s}{z-1} \right)^2 G_{HP}^3 y_{acc} \tag{6.29}$$

where y_{acc} is the acceleration signal on the tool-tip (see Figure 33.a), and G_{HP} is the high-pass filter with a high-pass frequency of 325 [Hz]. Signal conditioning and real-time implementation of the controller are both realized on a dedicated DSP board at a sampling frequency of 50 [kHz].

The controller is tuned by solving the optimization problems given in (6.20) and (6.26) with M=5 and L=5, and the state feedback control gain vectors **K** and **λ** are obtained. Note that both **K** and **λ** are optimized in a delay-independent manner, and hence they can be used for any spindle speed (n). The feedback controller ($K=r/y$ with the order of $M+L$) is implemented in discrete time for n=1800[rpm] using (6.27), which corresponds to a delay of T=0.033[sec]. K is combined with the estimate of inverse tool-tip tracking dynamics ($\hat{T}_T^{-1}$), and the overall process controller (C) is implemented in the form of $C=K\hat{T}_T^{-1}$.

Figure 34 summarizes controller and loop transmission dynamics. Figure 34.a shows the frequency response of C. As shown, controller dynamics is similar to G, but

frequencies of the open loop modes of G are shifted by state and observer feedback terms ($\mathbf{K}$ and $\boldsymbol{\lambda}$). Also, phase and magnitude ripples are introduced due to the $\hat{\mathbf{A}}_D\mathbf{q}_{m\text{-}\tau}^{(e)}$ term in the observer (see (6.22) and (6.27)). This dynamic behavior of C helps improve the stability margins of loop transmission as shown in Figure 34.b and c. Figure 34.b shows process open (aL_P) and closed loop (L_C) transmission dynamics for a=1[mm]. As shown, severe phase ripples of aL_P induced by the phase delay (see (6.3) and Figure 32.b) are significantly suppressed though the use of proposed controller in the vicinity of the most critical mode of G at ~2.5[kHz]. This ensures that phase of L_C remains above -180[deg] for a wide range of frequencies, which improves the minimum gain margin significantly, and shown in Figure 34.c.

The improvement in gain margin is also evident by the SLD diagrams shown in Figure 35.a. Notice that open loop process (without process control) has a limit width of cut (stability border) of a_{lim}=0.245[mm], which is impractically small. This is improved ~5× times by the proposed strategy, and a limit width of cut of 1.5[mm] is achieved (see Figure 35.a). As a benchmark, a recently published chatter mitigation method, delayed-feedback control [79] (DFC) is also implemented, and shown in Figure 35.a. As seen, DFC provides some improvement in the limit width of cut as well, but its improvement is limited in comparison to the proposed strategy.

To showcase robustness of the proposed strategy across different spindle speeds, machining tests are conducted at 1400, 1600 and 1800 [rpm]. Cylindrical workpieces (see Figure 33.a) with a=0.5, 0.75, 1, 1.25 and 1.5 [mm] widths of cut (wall thicknesses) are machined, and process stability is tested. Figure 35.a validates performance of the proposed controller.

Tool-tip acceleration measurements for machining tests with a=1.5[mm] are shown in Figure 35.b, c and d, respectively. In all experiments, severe chatter vibrations occur *without* the proposed controller. As noted from frequency spectrum of tool acceleration, chatter frequencies are slightly higher than the most dominant mode of G (2.5[kHz]), which is expected since delay ripples cause loop transmission to cross the real axis (-180[deg]) right after the resonance frequency (see Figure 32.b). Once the proposed controller is turned on, chatter vibrations are *eliminated*, and tool accelerations are attenuated drastically. Comparisons of machined surfaces for n=1800[rpm] is also

shown in Figure 35.e. As shown, chatter marks can clearly be seen on the surface machined without any compensation (Workpiece 2), and the proposed strategy results in a smoother surface that is free of chatter marks (see Workpiece 1). Thus, proposed controller can robustly attenuate chatter vibrations along a wide range of operating conditions.

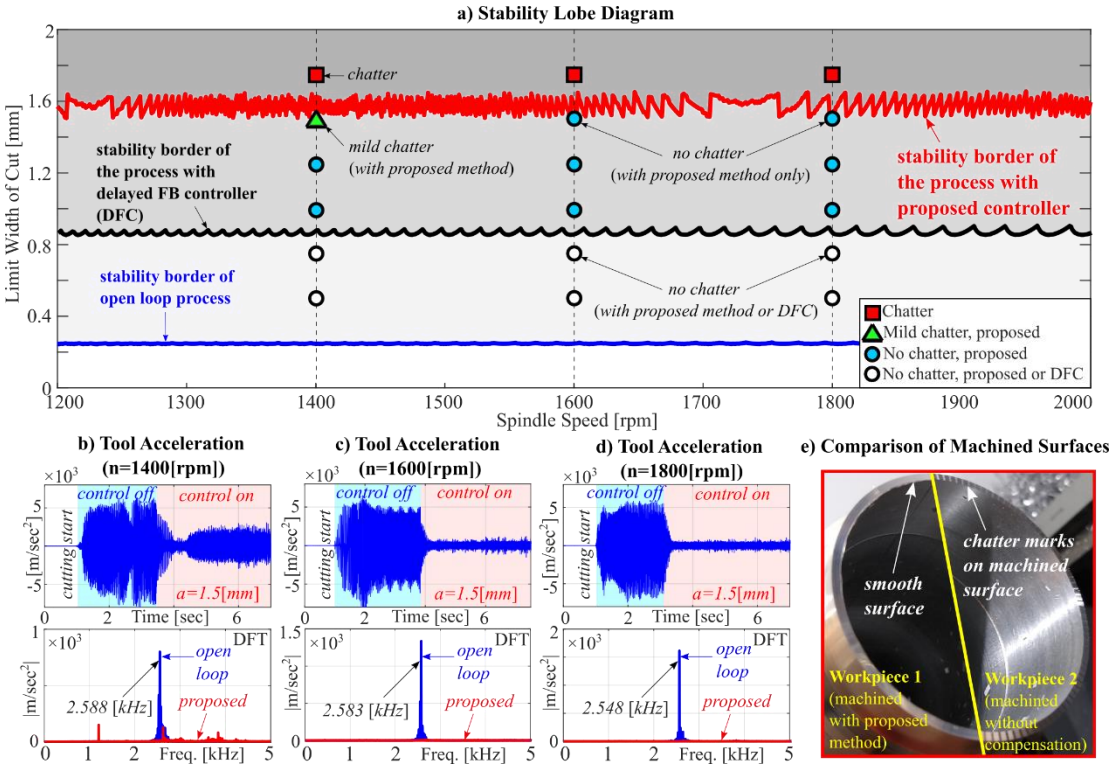

Figure 35. Comparison of Stability Lobe Diagrams (SLDs) and experimental machining results.

Robustness of the proposed method against variations in the G is also analyzed and an achievable a_{lim} is shown in Fig. 7. Proposed controller provides good robustness against shifts in the dominant resonance frequency (2.45~2.625[kHz]) from its nominal value of 2.5[kHz]. Variation in damping ratio (mode's quality factor) shows some adverse effect if it is largely overestimated. This is an expected behavior also observed in other techniques [16].

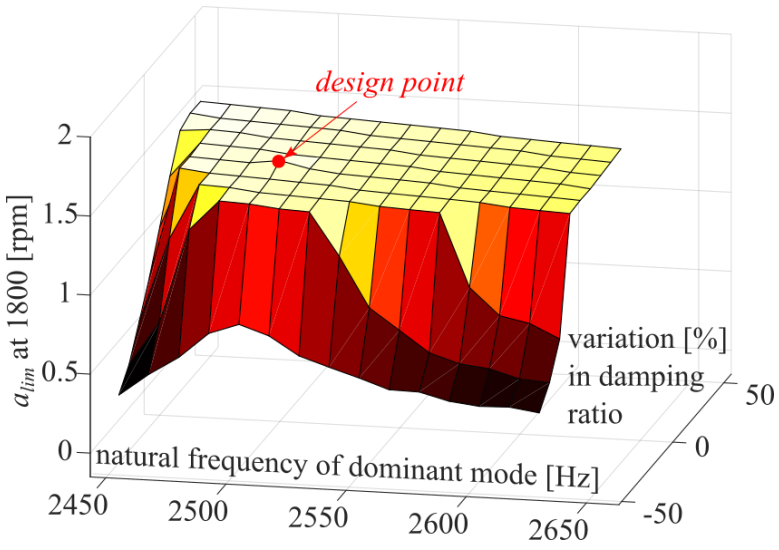

Figure 36. Controller performance with modeling errors.

6.5. Conclusions

This paper presented a novel chatter suppression strategy for turning processes. The proposed strategy is to control the tool position during machining operation to stabilize the process dynamics. Controller design is achieved by minimizing H∞-norm of process sensitivity dynamics. System states are accessed by means of an observer, designed by optimizing disturbance rejection of state-estimation dynamics. A Lyapunov function considering delay dynamics is utilized to postulate controller/observer design problems as convex optimization problems with LMIs, allowing numerical stability and efficiency. Controller design is independent of process delays, and so it can easily be implemented for different cutting(spindle) speeds. The controller is implemented on an industrial lathe equipped with a fast tool servo drive. Structural modes that are higher than feed-drive position tracking bandwidth are suppressed by inverting the tool position tracking TF. The proposed method is validated through machining experiments with a range of spindle speeds (1400, 1600 and 1800 [rpm]). It can increase stability of the system greatly, and workpieces with thicknesses of 1.5[mm] can be cut. This is an increase of 5× from the non-controlled case (0.245[mm]) providing significant gain in productivity.

7. General Conclusion

This dissertation presented passive and active control strategies that improve dynamic positioning accuracy of precision motion generation mechanisms. First, a novel trajectory optimization strategy is presented which aims to eliminate trajectory-induced excitation of lightly damped structural vibrations in CNC machine tools and 3D-Printers. Multi-axis motion trajectories are optimized in time and frequency domains to attenuate the magnitude of reference accelerations within a target frequency band. The target frequency band is selected to contain the resonance frequencies that are aimed to be avoided. Trajectory generation problem is posed as a convex optimization problem with linear equality and inequality constraints, which is easily solved to global optimality. A new windowing method is also introduced as a part of this strategy, which makes it feasible for toolpaths with long cycle times by reducing its computational cost. The proposed method is validated on an industrial 3-Axis Cartesian machine tool, and up to 6 times attenuation of column vibrations is achieved.

Secondly, a data-driven trajectory shaping method is presented for precision feed drives that suffer from positioning errors induced by ball-screw vibrations, servo-controller dynamics, and pre-sliding friction forces. A novel multi-stage trajectory pre-filter is designed to target each of these error sources separately. Pre-filter parameters are optimized utilizing machine-in-the-loop iterations, leveraging the data collected as the machine follows reference trajectories. Parameter optimization problems for each pre-filter is posed as a convex optimization problem, which guarantees reliable convergence with small number of iterations. The effectiveness of the proposed strategy is validated on an industrial machine tool, and it is shown that dynamic positioning errors are decreased up to 5 times compared to standard methods typically used in practice.

Finally, active tool control algorithms are proposed to eliminate chatter vibrations in turning processes. Proposed strategies utilize feed-drives of an industrial lathe augmented by a piezo-actuated fast tool servo (FTS), which moves the cutting tool at high frequencies during machining, based on tool acceleration feedback. The goal is to improve stability margins of the cutting process by this additional motion. Two tool

motion is control strategies are developed. Firstly, process loop transmission dynamics is shaped in frequency domain by an additional compensator, which in return creates a stable pocket in the Stability Lobe Diagram (SLD) for a target spindle speed. Secondly, process dynamics is modeled in state-space form, and a tool control algorithm is designed utilizing H-∞ control framework with internal delays. This approach lifts the SLD as opposed to creating a pocket. Both methods are implemented on the experimental setup, where chatter vibrations occur due to the most flexible mode of the tool-assembly. It is shown that proposed strategies can improve productivity by allowing stable machining of up to 5 times larger widths of cut.

Bibliography

[1] K. Erkorkmaz and Y. Hosseinkhani, “Control of ball screw drives based on disturbance response optimization,” *CIRP Ann. - Manuf. Technol.*, vol. 62, no. 1, pp. 387–390, 2013.

[2] D. S. Ertay, A. Yuen, and Y. Altintas, “Synchronized material deposition rate control with path velocity on fused filament fabrication machines,” *Addit. Manuf.*, vol. 19, pp. 205–213, Jan. 2018.

[3] T. Solatges, S. Rubrecht, M. Rognant, and P. Bidaud, “Adaptive input shaper design for flexible robot manipulators,” in *IEEE International Conference on Intelligent Robots and Systems*, 2017, pp. 444–449.

[4] L. Blanken, F. Boeren, D. Bruijnen, and T. Oomen, “Batch-To-Batch Rational Feedforward Control: From Iterative Learning to Identification Approaches, with Application to a Wafer Stage,” *IEEE/ASME Trans. Mechatronics*, vol. 22, no. 2, pp. 826–837, Apr. 2017.

[5] D. J. Gordon and K. Erkorkmaz, “Accurate control of ball screw drives using pole-placement vibration damping and a novel trajectory prefilter,” *Precis. Eng.*, vol. 37, no. 2, pp. 308–322, 2013.

[6] A. Dumanli and B. Sencer, “Optimal high-bandwidth control of ball-screw drives with acceleration and jerk feedback,” *Precis. Eng.*, vol. 54, pp. 254–268, 2018.

[7] Z. Jamaludin, H. Van Brussel, and J. Swevers, “Friction compensation of an XY feed table using friction-model-based feedforward and an inverse-model-based disturbance observer,” *IEEE Trans. Ind. Electron.*, vol. 56, no. 10, pp. 3848–3853, 2009.

[8] S. H. van der Meulen, R. L. Tousain, and O. H. Bosgra, “Fixed Structure Feedforward Controller Design Exploiting Iterative Trials: Application to a Wafer Stage and a Desktop Printer,” *J. Dyn. Syst. Meas. Control*, 2008.

[9] A. Amthor, C. Ament, and P. Li, “Friction identification and compensation on nanometer scale,” in *IFAC Proceedings Volumes (IFAC-PapersOnline)*, 2008.

[10] B. Sencer, A. Dumanli, and Y. Yamada, “Spline interpolation with optimal

frequency spectrum for vibration avoidance," *CIRP Ann.*, vol. 67, no. 1, pp. 377–380, 2018.

[11] M. Duan, D. Yoon, and C. E. Okwudire, "A limited-preview filtered B-spline approach to tracking control – With application to vibration-induced error compensation of a 3D printer," *Mechatronics*, vol. 56, pp. 287–296, 2017.

[12] Y. Altintas, A. Verl, C. Brecher, L. Uriarte, and G. Pritschow, "Machine tool feed drives," *CIRP Ann. - Manuf. Technol.*, vol. 60, no. 2, pp. 779–796, 2011.

[13] C. Okwudire and Y. Altintas, "Minimum Tracking Error Control of Flexible Ball Screw Drives Using a Discrete-Time Sliding Mode Controller," *J. Dyn. Syst. Meas. Control*, vol. 131, no. 5, p. 051006, Sep. 2009.

[14] A. Dumanli and B. Sencer, "Pre-compensation of servo tracking errors through data-based reference trajectory modification," *CIRP Ann.*, vol. 68, no. 1, pp. 397–400, 2019.

[15] K. K. Varanasi and S. A. Nayfeh, "The Dynamics of Lead-Screw Drives: Low-Order Modeling and Experiments," *J. Dyn. Syst. Meas. Control*, vol. 126, pp. 388–395, 2004.

[16] J. Munoa *et al.*, "Chatter suppression techniques in metal cutting," *CIRP Ann. - Manuf. Technol.*, vol. 65, no. 2, pp. 785–808, 2016.

[17] J. Y. Yoon and D. L. Trumper, "Friction microdynamics in the time and frequency domains: Tutorial on frictional hysteresis and resonance in precision motion systems," *Precis. Eng.*, vol. 55, pp. 101–109, Jan. 2019.

[18] K. Erkorkmaz and Y. Altintas, "High speed CNC system design. Part II: Modeling and Identification of Feed Drives," *Int. J. Mach. Tools Manuf.*, vol. 41, no. 10, pp. 1487–1509, Aug. 2001.

[19] Y. Altintas, *Manufacturing automation: metal cutting mechanics, machine tool vibrations, and CNC design*. Cambridge University Press, 2012.

[20] W. Singhose, L. Porter, M. Kenison, and E. Kriikku, "Effects of hoisting on the input shaping control of gantry cranes," *Control Eng. Pract.*, vol. 8, no. 10, pp. 1159–1165, 2000.

[21] M. F. Heertjes and H. Nijmeijer, "Self-tuning of a switching controller for scanning motion systems," *Mechatronics*, vol. 22, no. 3, pp. 310–319, 2012.

[22] C. Brecher, S. Schmidt, and M. Fey, “Analytic tuning of robust multi-mass dampers,” *CIRP Ann. - Manuf. Technol.*, vol. 65, no. 1, pp. 365–368, 2016.

[23] M. F. Zaeh, R. Kleinwort, P. Fagerer, and Y. Altintas, “Automatic tuning of active vibration control systems using inertial actuators,” *CIRP Ann. - Manuf. Technol.*, vol. 66, no. 1, pp. 365–368, 2017.

[24] X. Beudaert, K. Erkorkmaz, and J. Munoa, “Portable damping system for chatter suppression on flexible workpieces,” *CIRP Ann.*, vol. 68, no. 1, pp. 423–426, 2019.

[25] O. Zirn, “Machine tool analysis: modelling, simulation and control of machine tool manipulators,” ETH Zurich, Institute of Machine Tools and Manufacturing, 2008.

[26] M. Hanifzadegan and R. Nagamune, “Tracking and structural vibration control of flexible ball-screw drives with dynamic variations,” *IEEE/ASME Trans. Mechatronics*, vol. 20, no. 1, pp. 133–142, 2015.

[27] K. Tammi, “Active control of rotor vibrations by two feedforward control algorithms,” *J. Dyn. Syst. Meas. Control. Trans. ASME*, vol. 131, no. 5, pp. 1–10, Sep. 2009.

[28] R. Sato, G. Tashiro, and K. Shirase, “Analysis of the Coupled Vibration Between Feed Drive Systems and Machine Tool Structure,” *Int. J. Autom. Technol.*, vol. 9, no. 6, pp. 689–697, Nov. 2015.

[29] K. Erkorkmaz and A. Kamalzadeh, “High bandwidth control of ball screw drives,” *CIRP Ann. - Manuf. Technol.*, vol. 55, no. 1, pp. 393–398, 2006.

[30] N. C. Singer and W. P. Seering, “Preshaping Command Inputs to Reduce System Vibration,” *J. Dyn. Syst. Meas. Control*, vol. 112, no. 1, pp. 76–82, 1990.

[31] M. R. Khoshdarregi, S. Tappe, and Y. Altintas, “Integrated five-axis trajectory shaping and contour error compensation for high-speed CNC machine tools,” *IEEE/ASME Trans. Mechatronics*, vol. 19, no. 6, pp. 1859–1871, 2014.

[32] Y. Altintas and M. R. Khoshdarregi, “Contour error control of CNC machine tools with vibration avoidance,” *CIRP Ann. - Manuf. Technol.*, vol. 62, no. 1, pp. 335–338, 2012.

[33] W. E. Singhose, W. P. Searing, and N. C. Singer, “Improving repeatability of coordinate measuring machines with shaped command signals,” *Precis. Eng.*, vol. 18, no. 2–3, pp. 138–146, 1996.

[34] T. Flash and N. Hogan, “The coordination of arm movements: an experimentally confirmed mathematical model,” *J. Neurosci.*, vol. 5, no. 7, pp. 1688–1703, 1985.

[35] U. Pattacini, F. Nori, L. Natale, G. Metta, and G. Sandini, “An experimental evaluation of a novel minimum-jerk Cartesian controller for humanoid robots,” in *IEEE/RSJ International Conference on Intelligent Robots and Systems*, 2010, pp. 1668–1674.

[36] K. Erkorkmaz and Y. Altintas, “High speed CNC system design. Part I: Jerk limited trajectory generation and quintic spline interpolation,” *Int. J. Mach. Tools Manuf.*, vol. 41, no. 9, pp. 1323–1345, 2001.

[37] K. Erkorkmaz, A. Alzaydi, A. Elfizy, and S. Engin, “Time-optimal trajectory generation for 5-axis on-the-fly laser drilling,” *CIRP Ann. - Manuf. Technol.*, vol. 60, no. 1, pp. 411–414, 2011.

[38] B. Sencer and S. Tajima, “Frequency Optimal Feed Motion Planning in Computer Numerical Controlled Machine Tools for Vibration Avoidance,” *J. Manuf. Sci. Eng.*, vol. 139, p. 011006(13), 2016.

[39] Y. Altintas and K. Erkorkmaz, “Feedrate Optimization for Spline Interpolation In High Speed Machine Tools,” *CIRP Ann.*, vol. 52, no. 1, pp. 297–302, 2003.

[40] N. M. Patrikalakis and T. Maekawa, *Shape interrogation for computer aided design and manufacturing*. Berlin: Springer, 2010.

[41] H. Zhao, L. M. Zhu, and H. Ding, “A real-time look-ahead interpolation methodology with curvature-continuous B-spline transition scheme for CNC machining of short line segments,” *Int. J. Mach. Tools Manuf.*, vol. 65, pp. 88–98, 2013.

[42] K. Erkorkmaz, “Efficient Fitting of the Feed Correction Polynomial for Real-Time Spline Interpolation,” *J. Manuf. Sci. Eng.*, vol. 137, no. 4, p. 044501(8), 2015.

[43] L. Piegl and W. Tiller, *The NURBS Book*. Springer Berlin Heidelberg, 1997.

[44] K. Erkorkmaz and Y. Altintas, “Quintic Spline Interpolation With Minimal Feed Fluctuation,” *J. Manuf. Sci. Eng.*, vol. 127, pp. 339–349, 2005.

[45] D. Q. Mayne, “Model predictive control: Recent developments and future promise,” *Automatica*, vol. 50, no. 12, pp. 2967–2986, 2014.

[46] K. Erkorkmaz, Q. G. Chen (Christina), M. Y. Zhao, X. Beudaert, and X. S. Gao, “Linear programming and windowing based feedrate optimization for spline toolpaths,” *CIRP Ann. - Manuf. Technol.*, vol. 66, no. 1, pp. 393–396, 2017.

[47] P. Bloomfield, *Fourier analysis of time series : an introduction*. Wiley, 2000.

[48] Michael Grant and Stephen Boyd, “CVX: Matlab software for disciplined convex programming, version 2.0 beta.,” 2013. [Online]. Available: http://cvxr.com/cvx.

[49] K. Erkorkmaz, C. H. Yeung, and Y. Altintas, “Virtual CNC system. Part II. High speed contouring application,” *Int. J. Mach. Tools Manuf.*, vol. 46, no. 10, pp. 1124–1138, Aug. 2006.

[50] D. Kono, A. Matsubara, I. Yamaji, and T. Fujita, “High-precision machining by measurement and compensation of motion error,” *Int. J. Mach. Tools Manuf.*, vol. 48, no. 10, pp. 1103–1110, Aug. 2008.

[51] Z. Jamaludin, H. Van Brussel, G. Pipeleers, and J. Swevers, “Accurate motion control of xy high-speed linear drives using friction model feedforward and cutting forces estimation,” *CIRP Ann.*, vol. 57, no. 1, pp. 403–406, Jan. 2008.

[52] H. Van Brussel and P. Van Den Braembussche, “Robust control of feed drives with linear motors,” *CIRP Ann. - Manuf. Technol.*, vol. 47, no. 1, pp. 325–328, Jan. 1998.

[53] A. Matsubara, K. Nagaoka, and T. Fujita, “Model-reference feedforward controller design for high-accuracy contouring control of machine tool axes,” *CIRP Ann. - Manuf. Technol.*, vol. 60, no. 1, pp. 415–418, Jan. 2011.

[54] “Siemens Sinumerik 840D/810D/FM-NC OEM package MMC User’s Manual,” 1997.

[55] S. Boyd and L. Vandenberghe, *Convex optimization*. Los Angeles: Cambridge University Press, 2014.

[56] J. Y. Yoon and D. L. Trumper, “Friction modeling, identification, and compensation based on friction hysteresis and Dahl resonance,” *Mechatronics*, vol. 24, no. 6, pp. 734–741, Sep. 2014.

[57] Amthor A, Zschaeck S, and Ament C, “High Precision Position Control Using an Adaptive Friction Compensation Approach,” *IEEE Trans. Autom. Control*, vol. 55, no. 1, pp. 274–278, 2010.

[58] D. J. Gordon and K. Erkorkmaz, “Precision control of a T-type gantry using sensor/actuator averaging and active vibration damping,” *Precis. Eng.*, vol. 36, no. 2, pp. 299–314, Apr. 2012.

[59] X. Dong, X. Liu, D. Yoon, and C. E. Okwudire, “Simple and robust feedforward compensation of quadrant glitches using a compliant joint,” *CIRP Ann.*, vol. 66, no. 1, pp. 353–356, Jan. 2017.

[60] T. Piatkowski, “Dahl and LuGre dynamic friction models - The analysis of selected properties,” *Mech. Mach. Theory*, 2014.

[61] F. Al-Bender, V. Lampaert, and J. Swevers, “The generalized Maxwell-slip model: A novel model for friction simulation and compensation,” *IEEE Trans. Automat. Contr.*, vol. 50, no. 11, pp. 1883–1887, 2005.

[62] S. Tajima, B. Sencer, and E. Shamoto, “Accurate interpolation of machining tool-paths based on FIR filtering,” *Precis. Eng.*, 2018.

[63] W. Singhose and J. Vaughan, “Reducing vibration by digital filtering and input shaping,” *IEEE Trans. Control Syst. Technol.*, vol. 19, no. 6, pp. 1410–1420, Nov. 2011.

[64] M. Tomizuka, “Zero Phase Error Tracking Algorithm for Digital Control,” *J. Dyn. Syst. Meas. Control*, 1987.

[65] F. Boeren, A. Bareja, T. Kok, and T. Oomen, “Frequency-Domain ILC Approach for Repeating and Varying Tasks: With Application to Semiconductor Bonding Equipment,” *IEEE/ASME Trans. Mechatronics*, vol. 21, no. 6, pp. 2716–2727, 2016.

[66] L. Blanken, G. Isil, S. Koekebakker, and T. Oomen, “Data-Driven Feedforward Learning using Non-Causal Rational Basis Functions: Application to an Industrial Flatbed Printer,” in *Proceedings of the American*

Control Conference, 2018.

[67] P. Van Overschee and B. De Moor, “A unifying theorem for three subspace system identification algorithms,” *Automatica*, vol. 31, no. 12, pp. 1853–1864, 1995.

[68] D. N. Miller and R. A. De Callafon, “Subspace identification with eigenvalue constraints,” *Automatica*, vol. 49, no. 8, pp. 2468–2473, Aug. 2013.

[69] M. Ruderman and M. Iwasaki, “Observer of nonlinear friction dynamics for motion control,” *IEEE Trans. Ind. Electron.*, vol. 62, no. 9, pp. 5941–5949, 2015.

[70] J. Nocedal and S. J. Wright, *Numerical Optimization*. New York: Springer, 2006.

[71] Y. Altintas and M. Weck, “Chatter stability of metal cutting and grinding,” *CIRP Ann. - Manuf. Technol.*, vol. 53, no. 2, pp. 619–642, Jan. 2004.

[72] E. Budak and L. T. Tunc, “Identification and modeling of process damping in turning and milling using a new approach,” *CIRP Ann. - Manuf. Technol.*, vol. 59, no. 1, pp. 403–408, Jan. 2010.

[73] E. Shamoto, S. Fujimaki, B. Sencer, N. Suzuki, T. Kato, and R. Hino, “A novel tool path/posture optimization concept to avoid chatter vibration in machining - Proposed concept and its verification in turning,” *CIRP Ann. - Manuf. Technol.*, vol. 61, no. 1, pp. 331–334, Jan. 2012.

[74] X. Lu, F. Chen, and Y. Altintas, “Magnetic actuator for active damping of boring bars,” *CIRP Ann. - Manuf. Technol.*, vol. 63, no. 1, 2014.

[75] F. Chen, M. Hanifzadegan, Y. Altintas, and X. Lu, “Active damping of boring bar vibration with a magnetic actuator,” *IEEE/ASME Trans. Mechatronics*, vol. 20, no. 6, 2015.

[76] E. Abele, Y. Altintas, and C. Brecher, “Machine tool spindle units,” *CIRP Ann. - Manuf. Technol.*, vol. 59, no. 2, pp. 781–802, Jan. 2010.

[77] J. Munoa, X. Beudaert, K. Erkorkmaz, A. Iglesias, A. Barrios, and M. Zatarain, “Active suppression of structural chatter vibrations using machine drives and accelerometers,” *CIRP Ann. - Manuf. Technol.*, 2015.

[78] N. J. M. Van Dijk, N. Van De Wouw, E. J. J. Doppenberg, H. A. J. Oosterling,

and H. Nijmeijer, “Robust active chatter control in the high-speed milling process,” *IEEE Trans. Control Syst. Technol.*, vol. 20, no. 4, pp. 901–917, 2012.

[79] I. Mancisidor, A. Pena-Sevillano, Z. Dombovari, R. Barcena, and J. Munoa, “Delayed feedback control for chatter suppression in turning machines,” *Mechatronics*, vol. 63, p. 102276, Nov. 2019.

[80] J. Munoa, I. Mancisidor, N. Loix, L. G. Uriarte, R. Barcena, and M. Zatarain, “Chatter suppression in ram type travelling column milling machines using a biaxial inertial actuator,” *CIRP Ann. - Manuf. Technol.*, vol. 62, no. 1, 2013.

[81] Y. Altintas and A. Woronko, “A piezo tool actuator for precision turning of hardened shafts,” *CIRP Ann. - Manuf. Technol.*, 2002.

[82] A. Dumanli and B. Sencer, “Data-Driven Iterative Trajectory Shaping for Precision Control of Flexible Feed Drives,” *IEEE/ASME Trans. Mechatronics*, 2020.

[83] G. Stepan, A. K. Kiss, B. Ghalamchi, J. Sopanen, and D. Bachrathy, “Chatter avoidance in cutting highly flexible workpieces,” *CIRP Ann. - Manuf. Technol.*, vol. 66, no. 1, pp. 377–380, Jan. 2017.

[84] Y. Altintas, G. Stepan, D. Merdol, and Z. Dombovari, “Chatter stability of milling in frequency and discrete time domain,” *CIRP J. Manuf. Sci. Technol.*, vol. 1, no. 1, 2008.

[85] X. Beudaert, O. Franco, K. Erkorkmaz, and M. Zatarain, “Feed drive control tuning considering machine dynamics and chatter stability,” *CIRP Ann.*, vol. 69, no. 1, pp. 345–348, Jan. 2020.

[86] V. Thevenot, L. Arnaud, G. Dessein, and G. Cazenave-Larroche, “Integration of dynamic behaviour variations in the stability lobes method: 3D lobes construction and application to thin-walled structure milling,” *Int. J. Adv. Manuf. Technol.*, vol. 27, no. 7–8, 2006.

[87] Y. Yang, J. Muñoa, and Y. Altintas, “Optimization of multiple tuned mass dampers to suppress machine tool chatter,” *Int. J. Mach. Tools Manuf.*, vol. 50, no. 9, 2010.

[88] Xu Chen and M. Tomizuka, “Control methodologies for precision positioning

systems," in *2013 American Control Conference*, 2013.

[89] J. Monnin, F. Kuster, and K. Wegener, "Optimal control for chatter mitigation in milling-Part 1: Modeling and control design," *Control Eng. Pract.*, vol. 24, no. 1, pp. 156–166, Mar. 2014.

[90] J. Monnin, F. Kuster, and K. Wegener, "Optimal control for chatter mitigation in milling-Part 2: Experimental validation," *Control Eng. Pract.*, vol. 24, no. 1, pp. 167–175, Mar. 2014.

[91] W. Michiels, K. Engelborghs, P. Vansevenant, and D. Roose, "Continuous pole placement for delay equations," *Automatica*, vol. 38, no. 5, pp. 747–761, May 2002.

[92] J. H. Kim and H. B. Park, "H∞ state feedback control for generalized continuous/discrete time-delay system," *Automatica*, vol. 35, no. 8, pp. 1443–1451, Aug. 1999.

[93] S. Boyd, L. El Ghaoui, E. Feron, and V. Balakrishnan, *Linear Matrix Inequalities in System and Control Theory*. Society for Industrial and Applied Mathematics, 1994.

[94] D. Aslan and Y. Altintas, "On-line chatter detection in milling using drive motor current commands extracted from CNC," *Int. J. Mach. Tools Manuf.*, 2018.

[95] A. Woronko, J. Huang, and Y. Altintas, "Piezoelectric tool actuator for precision machining on conventional CNC turning centers," *Precis. Eng.*, vol. 27, no. 4, 2003.

Appendix

Equivalence between (6.15) and (6.20) is proven in this appendix. As reported in [92], $\mathbf{H}\prec\mathbf{0}$ in (6.20) is equivalent to $\mathbf{F}\prec\mathbf{0}$ which is a symmetric matrix defined as:

$$\mathbf{F}=\begin{bmatrix} \boldsymbol{\Xi} & \left(\mathbf{A}+\mathbf{BK}\right)^T\mathbf{PA}_D & \mathbf{0} & \left(\mathbf{A}+\mathbf{BK}\right)^T\mathbf{PB}+\mathbf{K}^T \\ * & -\mathbf{R}_1+\mathbf{A}_D^T\mathbf{PA}_D & \mathbf{0} & \mathbf{A}_D^T\mathbf{PB} \\ * & * & -R_2 & \mathbf{0} \\ * & * & * & -\gamma+\mathbf{B}^T\mathbf{PB} \end{bmatrix} \tag{6.30}$$

with:

$$\boldsymbol{\Xi}=\left(\mathbf{A}+\mathbf{BK}\right)^T\mathbf{P}\left(\mathbf{A}+\mathbf{BK}\right)-\mathbf{P}+\mathbf{R}_1+\mathbf{K}^TR_2\mathbf{K}+\mathbf{K}^T\mathbf{K} \tag{6.31}$$

If $\mathbf{F}\prec 0$, then the following must hold:

$$\begin{bmatrix}\mathbf{q}_m & \mathbf{q}_{m-\tau} & \mathbf{Kq}_{m-\tau} & w_m\end{bmatrix}\mathbf{F}\begin{bmatrix}\mathbf{q}_m & \mathbf{q}_{m-\tau} & \mathbf{Kq}_{m-\tau} & w_m\end{bmatrix}^T<0 \tag{6.32}$$

Left hand side of (6.32) is written as a scalar expression by making use of the definition of $\mathbf{q}_{m+1}$ in (6.13) and S in (6.15):

$$\begin{aligned}\mathbf{q}_{m+1}^T\mathbf{P}\mathbf{q}_{m+1}-\mathbf{q}_m^T\left(\mathbf{P}-\mathbf{R}_1-\mathbf{K}^TR_2\mathbf{K}\right)\mathbf{q}_m-\mathbf{q}_{m-\tau}^T\mathbf{R}_1\mathbf{q}_{m-\tau}\cdots \\ \cdots-\mathbf{q}_{m-\tau}^T\mathbf{K}^TR_2\mathbf{K}\mathbf{q}_{m-\tau}+e_m^2-\gamma w_m^2<0\end{aligned} \tag{6.33}$$

where $e=Sw$; w is defined in (6.13), and S is defined in (6.15). By making use of the Lyapunov function candidate (V) defined in (6.16), (6.33) can be rewritten as:

$$\Delta V_m+e_m^2-\gamma w_m^2<0 \tag{6.34}$$

Since the (6.34) holds for the m^{th} sample time, summation over samples does not change the inequality, and therefore:

$$\sum_{i=1}^{\infty}\Delta V_i+\sum_{i=1}^{\infty}e_i^2-\gamma\sum_{i=1}^{\infty}w_i^2<0 \tag{6.35}$$

Notice that the second and third terms of (6.35) define 2-norms of e_m and w_m, respectively. The first term of (6.35) is simplified, and the inequality is rewritten as:

$$\lim_{m\to\infty}\left\{V_m\right\}-V_1+\left\|e_m\right\|_2^2-\gamma\left\|w_m\right\|_2^2<0 \tag{6.36}$$

Assuming zero initial conditions, i.e. $\mathbf{q}_1=\mathbf{0}$, $V_1=0$ holds. Additionally, (6.15) requires S to be stable, which dictates that V_m converges to "0" as m approaches to ∞. Thus, (6.36) is further simplified as:

$$\frac{\|e_m\|_2}{\|w_m\|_2} = \|S\|_\infty < \sqrt{\gamma} \tag{6.37}$$

(6.37) implies that $\sqrt{\gamma}$ is the upper bound of $||S||_\infty$, assuming that γ>0. Since (6.15) minimizes $||S||_\infty$, and (6.20) minimizes $\sqrt{\gamma}$, it is proven that solving (6.20) minimizes $||S||_\infty$.